

**Probing the Redox Environment of Single Human Cancer Cells
using Scanning Electrochemical Microscopy**

by

Sabine Kuss, M.Sc.

Chemistry Department, McGill University, Montreal, Canada

Submitted May 2015

Dissertation

A thesis submitted to

McGill University

in partial fulfillment

of the requirements

of the degree of

Doctor of Philosophy

© Sabine Kuss, 2015

DEDICATION

This dissertation is dedicated to
my grandmother Eva Rosemarie Hantschel.

“Life begins at the end of your comfort zone.”

Neale Donald Walsch

TABLE OF CONTENTS

DEDICATION.....	1
TABLE OF CONTENTS.....	2
LIST OF FIGURES	7
LIST OF TABLES	14
LIST OF ABBREVIATIONS AND ACRONYMS	15
LIST OF SYMBOLS	17
ABSTRACT.....	19
RÉSUMÉ	21
ACKNOWLEDGEMENTS.....	23
CONTRIBUTION OF AUTHORS.....	25
CHAPTER I.....	29
1.1 Scope of the Dissertation.....	29
1.1.1 The Redox State of Glutathione and the Overall Redox Environment of the Cell	29
1.2 The Challenge.....	33
1.3 Scanning Electrochemical Microscopy (SECM).....	34
1.3.1 Principles	34
1.3.2 The Stationary Electrode	39
1.3.3 Approaching a Surface	41

1.3.3.1 SECM Operation Modes	42
1.3.4 The Scanning Electrode.....	45
1.3.4.1 SECM Line Scans and Imaging	45
1.3.4.2 Understanding the Current Behaviour.....	48
1.3.4.3 Modes of Imaging.....	50
1.3.5 Numerical Modeling for SECM.....	51
1.3.6 Introducing Convection	52
1.4 Biology meets Electrochemistry.....	54
1.4.1 Cellular Transmembrane Export of Molecules	54
1.4.2 Model Cell Types and Cell Culture Conditions	55
1.4.3 Multidrug Resistance.....	57
1.4.4 Redox Mediators for Biological SECM Studies	58
1.4.5 Homogeneous and Heterogeneous Reactions	60
1.6 Dissertation Outline.....	63
CHAPTER II.....	65
2.1 Abstract.....	67
2.2 Introduction	67
2.3 Material and Methods.....	69
2.3.1 Formation of Cell Culture Patterns.....	69
2.3.2 Electrochemical Measurements.....	70

2.4 Results and Discussion	71
2.4.1 Patterning of Cell Islands	71
2.4.2 SECM Imaging.....	74
2.4.3 Formation of Cell Coculture Pattern	77
2.4.4 SECM Imaging of Cocultures and Data Analysis	78
2.5 Conclusions	83
2.6 Acknowledgments	84
CHAPTER III	85
3.1 Abstract.....	87
3.2 Introduction	87
3.3 Material and Methods.....	89
3.3.1 Materials and Reagents.....	89
3.3.2 Microelectrode Fabrication	90
3.3.3 Cell Culture and Sample Preparation	91
3.3.4 SECM Measurements.....	91
3.4 Theory and Simulations.....	93
3.5 Results and Discussion	95
3.6 Conclusions	105
3.7 Acknowledgements	106
CHAPTER IV	107

4.1 Abstract.....	109
4.2 Introduction	109
4.3 Materials and Methods	112
4.3.1 Microelectrode Fabrication.	112
4.3.2 SECM Measurements.....	113
4.4 Theory and Simulations.....	114
4.5 Results and Discussion	115
4.6 Conclusion.....	122
4.7 Acknowledgements	122
CHAPTER V	123
5.1 Abstract.....	125
5.2 Introduction	125
5.3 Materials and Methods	127
5.3.1 Microelectrode Fabrication.	127
5.3.2 Cell Culture and Sample Preparation.	128
5.3.3 Cell Viability Measurements.....	128
5.3.4 SECM Measurements.....	128
5.3.5 Fluorescent Microscopy.	129
5.4 Results and Discussion	130
5.5 Conclusion.....	136

5.6 Acknowledgements	136
CHAPTER VI	137
6.1 Summary of Objective Achievements.....	137
6.2 Comparison of the Presented Methodologies for Cell Kinetic Determination.....	139
6.3 SECM Studies on Biological Samples	141
6.3.1 Quantitative SECM Studies in Literature.....	142
6.4 Potential Future Studies.....	144
6.4.1 Effect of GTC on Other Cell Lines	145
6.4.2 Further Development of the SECM Convection Method.....	145
6.4.3 MRP1 Distribution in HeLa and HeLa-R.....	147
APPENDIX A	151
A.1 Cell Management.....	151
A.2 Preparation of Plastic Substrates	152
A.3 Fabrication of Membranes and Cover Slabs.....	152
A.4 Imaging.....	153
A.5 Data Analysis.....	153
APPENDIX B	155
APPENDIX C	157
APPENDIX D.....	160
REFERENCES	162

LIST OF FIGURES

Figure 1.1. Schematic representation of intracellular action of glutathione (GSH) and glutathione disulfide (GSSG). GSH is synthesized from three amino acids. L-glutamic acid reacts with L-cysteine to form γ -glutamyl-L-cysteine, catalyzed by the enzyme γ -glutamylcysteine synthetase. γ -glutamyl-L-cysteine reacts further with L-glycine to GSH in the presence of the γ -glutathione synthase. GSH can be oxidized to GSSG when reaction with peroxides and be regenerated by the glutathione reductase, whereby NADPH functions as electron donor. 32

Figure 1.2. Schematic representation of the instrumental design of an SECM. (A) Instrumental set up including Z axis positioner (A), constant distance controller (B), light source (C), electrochemical cell (D) as well as working electrode (WE), counter electrode (CE) and reference electrode (RE). (B) Simplified representation of the low current potentiostat connected to the platinum WE, CE, RE and a computer during imaging of biological samples. 38

Figure 1.3. Microelectrode used for SECM measurements. (A) Full length of a standard 25 μm Pt microelectrode, (B) size comparison of a microelectrode tip and a Canadian 1 cent coin, (C) top view of the same electrode shown in (A) and (B). 39

Figure 1.4. Example of a Cyclic Voltammogram for a 25 μm Pt electrode in 1 mM FcCH₂OH in cell medium without serum. The electrochemical potential is linearly swept over a range of 600 mV, whereas a steady state behaviour is shown from 0.3 to 0.5 V vs. Ag/AgCl reference electrode. Therefore a potential of 0.4 V vs. Ag/AgCl reference electrode is chosen for the oxidation of FcCH₂OH. 41

Figure 1.5. Representation of different operation modes during SECM. (A) Collection/Generation modes as well as (B) feedback modes are presented. 43

Figure 1.6. Options of imaging in SECM (A) Representation of a line scan profile, taken from (B) a 3D image of a 300 μm by 300 μm scan area. The dotted line indicates the extracted line scan.

..... 46

Figure 1.7. Reactivity and topographical contributions to the measured electrochemical current.

(A) Diffusion of a redox species from an active site of the substrate. (B) Change in topography, allowing an increase in diffusion of the redox species towards the electrode. (C) An active flux of redox species towards the microelectrode through a permeable surface. 49

Figure 1.8. Schematic representation of the imaging modes during SECM. (A) Constant height mode, whereas the electrode always keeps the same height above the substrate. (B) Constant distance mode. The electrode keeps the same tip-to-substrate distance at all times..... 51

Figure 1.9. Optical micrographs of cell cultures. (A) HeLa and (B) HeLa-R. 57

Figure 1.10. Schematic representation of multidrug resistance in cancer cells. Exposure to chemotherapeutic drugs usually leads to cell death in cancer. In drug resistant cells, however, a drug can be transported from the cell directly or in conjugation with GSH through active MRP1 pumps..... 58

Figure 1.11. Schematic representation of the FcCH₂OH and glutathione relationship. FcCH₂OH reacts with intracellular GSSG to generate GSH, which is expelled from the cell and regenerates FcCH₂OH..... 60

Figure 1.12. Schematic representation of homogeneous and heterogeneous reactions occurring during live cell SECM analysis..... 62

Figure 2.1 Layout of the elastomeric stencil and resulting cell patterns. (A) Photograph of an open through-hole membrane as used within this study. (Inset) Scanning electron micrograph of a corner

section. (Scale bar: 500 μm .) (B) Close-up view of the central part of the membrane. The array contains 100 openings of 50 μm in diameter arranged in a 10×10 configuration. (Scale bar: 500 μm .) (Inset) Scanning electron micrograph depicts a cross-sectional view of the array after the membrane had been cut in half using a blade. (Scale bar: 100 μm .) (C–H) Optical micrographs of cell islands formed from HeLa (C–E) and HeLa-R cells (F–H). OPS were generated using circular through-holes of 400 and 200 μm indiameter as well as rectangular features of 50 μm in width and 73

length, respectively. (Scale bar: 100 μm .) 73

Figure 2.2 Cell imaging using SECM. (A) Schematic illustration of constant-height feedback mode SECM imaging with a living cell in the presence of FcCH_2OH as a redox mediator. FcCH_2OH is oxidized to $[\text{FcCH}_2\text{OH}]^+$ at the Pt microelectrode, and regenerated in proximity to the cell as a result of GSH efflux. (B) Normalized SECM current recorded at a distance of 12 μm above the substrate when HeLa cells were exposed to FcCH_2OH (1 mM) for 75 min. (Inset) Close-up 3D view of the signal obtained from an individual cell island. (Scale bar: 50 μm .) ... 75

Figure 2.3 Formation of cell coculture patterns in a side-by-side configuration. Patterning scheme involves a template partly covered by a PDMS slab to promote selective adhesion and growth of a first cell line (HeLa-R) on the substrate. The optical microscope image depicts an OPS occupied by three HeLa-R cells whereas the adjacent one remains covered by the PDMS slab. Once the slab is removed, the sample is exposed to a second cell line during which cells adhere on OPS that were inaccessible during the first incubation step. The fluorescence micrograph shows stained HeLa cells (red) and HeLa-R cells (green) in the form of a side-by-side coculture pattern. (Scale bar: 100 μm .) 80

Figure 2.4 SECM imaging and decoupling of feedback response for a HeLa and HeLa-R cell coculture substrate. (A) Optical micrograph of a coculture pattern containing seven HeLa-R cells (Left) and six HeLa cells (Right). (B) Fluorescence micrograph of the sample shown in A, with HeLa-R cells stained green and HeLa cells stained red. (C and D) Normalized SECM currents recorded with the same sample at 12 μm above the substrate in 1 mM $[\text{Ru}(\text{NH}_3)_6]^{3+}$ (C) and 1 mM FcCH_2OH (D). (E) Extracted normalized tip-to-substrate distance profile. (F) Profile of the extracted apparent heterogeneous rate constant ($\text{cm}\cdot\text{s}^{-1}$) for the sample shown in A. (Scale bar: 50 μm .)..... 82

Figure 3.1. Line scans across (a) a flat Pt conductor of 25 μm diameter and (b) a mercury hemisphere of 25 μm diameter in a non-conducting surface. (c) Experimental data and linear fit of the dependence of the normalized peak current on scanning velocity for scans across the two model substrates..... 97

Figure 3.2. (a) Line scans over HeLa cancer cells. (b) Experimental data and linear fit of the dependence of the normalized peak current on scanning velocity for scans over human HeLa cancer cells..... 98

Figure 3.3. (a) Simulation result of the tip current profile of line scans across a flat conductor of 25 μm diameter, the tip-to-substrate distance $d = 8 \mu\text{m}$. (b) Velocity magnitude (m/s) and velocity field of the fluid at $y = 0$ when the tip is scanned over a flat conductive substrate with velocity $v = 25 \mu\text{m/s}$ 100

Figure 3.4. (a) Simulation result of the tip current profile at $y = 0$ over a conductive domed substrate (Hg drop) with different scanning velocity $v = 2\text{--}50 \mu\text{m/s}$, the tip-to-substrate distance $d = 15 \mu\text{m}$; (b) velocity magnitude (m/s) and velocity field of the fluid when the tip is scanned over a conductive substrate with velocity $v = 25 \mu\text{m/s}$ 101

Figure 3.5. Simulation result of (a) the tip current profile and (b) normalized tip current profile over an insulating domed substrate (same shape as in Fig. 3.3b) with different scanning velocity $v = 2\text{--}50 \mu\text{m/s}$, the tip-to-substrate distance $d = 15 \mu\text{m}$, the tip current is normalized at the position far from the substrate ($x = 60 \mu\text{m}$) for each scanning velocity..... 103

Figure 3.6. Normalized tip current as a function of scanning velocity for pure negative feedback (simulation), pure positive feedback (simulation) and HeLa cell (experiments)..... 105

Figure 4.1: Experimental results (left panel) and simulation results (right panel) of the moving tip over a flat insulator (A), a flat conductor embedded into an insulator (B), and a mercury hemisphere deposited on the $25 \mu\text{m}$ Pt conductor (C) used in (B) at several velocities from 2 to $50 \mu\text{m/s}$ 117

Figure 4.2: (A) Normalized current as a function of Ps in log scale: simulation results (line) for several kinetics varied from 10^{-8} to 10^1 m/s, experimental results over the insulating substrate (circle) and experimental results (square) over the conductive substrate. (B) The slope α of the normalized current taken at high $Ps > 1$ as a function of kinetic k_0 120

Figure 4.3: (A) Line scan across a single HeLa cell in FcCH_2OH during SECM imaging at different velocities ranging from 2 to $50 \mu\text{m/s}$. (B) SECM imaging of a comparable HeLa cell exposed to $[\text{Ru}(\text{NH}_3)_6]^{3+}$. (C) Normalized current as a function of Ps in log scale: simulation results (line) for several kinetics varied from 10^{-8} to 10^1 m/s, experimental results over a HeLa cell (square) and a HeLa-R cell (circle) as well as over a mercury drop (\times) in FcCH_2OH 121

Figure 5.1: (A) SECM line scan profile at $12 \mu\text{m}$ above a single living HeLa cell at $50 \mu\text{m/s}$ scan rate before and after treatment with EGCg. (B) Linear dependency of normalized peak current on scan velocity before and after treatment with EGCg. 132

Figure 5.2: Results summary of the three experimental sample groups: control (before treatment), placebo (treated with DMEM-), and EGCg treated sample. The dashed lines represent the simulated normalized peak currents for several substrate kinetics ranging from 10^{-8} to 10^1 m/s. The probe is positioned at $12\mu\text{m}$ above the samples..... 133

Figure 5.3: (A) Time dependent CMFDA response depending on intracellular GSH content. (B) Proposed time dependent reaction scheme for EGCg effect leading to alterations of intracellular GSH content and, eventually, cell death. 136

Figure 6.1: Schematic representation of cell height determination by means of the SECM convection method. (A) Extrapolation of the current value without contribution of convection. (B) Calculation of cell height (d_{cs}) from tip-to-substrate distance (d) after obtaining the tip-to-cell distance (d_{TC}) by numerical simulations. 147

Figure 6.2: Schematic representation of MRP1 pump recognition using functionalized Au-NP. MRP1 can be recognized by a specific antibody (red), binding to a specific sequence (red dotted line). Its biotinylation (B) allows linkage to neutravidin (NTN), which is tied to a biotinylated 10 nm Au-NP. 149

Figure A.1. Oxidation of FcCH_2OH to $[\text{FcCH}_2\text{OH}]^+$ 154

Figure A.2. Formation of glutathione disulfide through intermolecular coupling of glutathione. 154

Figure B.1. The hydrogen evolution potential increases upon mercury deposition on the platinum electrode. 155

Figure B.2. Geometrical domain used in the numerical simulation: the UME is scanned from left to right with the scanning velocity $v = 02\text{-}50$ ($\mu\text{m/s}$), the tip-to-substrate distance $d = 15$ (μm), the

radius of the tip $a_{tip} = 12.5 \mu\text{m}$ with $RG = 5$, the radius of the cell $a_{sub} = 25 \mu\text{m}$, height of the cell $h_{sub} = 10 \mu\text{m}$, the potential applied on the tip $E_{tip} = 0.5 \text{ VSCE}$ 156

Figure C.1. Schematic representation of experimental setup and parameters for numerical simulations..... 157

Figure C.2. SECM imaging of a single living HeLa cell. (A) Schematic representation of experimental procedure. The microelectrode is positioned $12 \mu\text{m}$ above the substrate and about $100 \mu\text{m}$ to the left of a target cell. The biased tip scans across the center of the cell at velocities ranging from 2 to $50 \mu\text{m/s}$ 158

Figure C.3. Scan direction and fluid movement during SECM scan. The microelectrode (white) is scanned from left to right at (A) $0 \mu\text{m/s}$, (B) $2 \mu\text{m/s}$, (C) $10 \mu\text{m/s}$ and (D) $20 \mu\text{m/s}$, which causes a fluid flow from right to left. 159

Figure C.4. Numerical simulations of an SECM scan across a domed substrate at velocities ranging from 2 to $10 \mu\text{m/s}$. Simulation parameters: initial tip-to-substrate distance is $12 \mu\text{m}$, mediator is 1mM ferrocyanide, $25 \mu\text{m}$ Pt microelectrode with $RG=5$ 159

Figure D.1. (A) Cyclic Voltammogram of 1 mM EGCg in PBS. An irreversible two electron transfer reaction is obvious during the oxidation of EGCg. Due to electrode blockage by the oxidation product of EGCg, the electrochemical signal diminishes after one initial sweep. Insets showing optical micrographs of the electrode before (A) and after (B) 21 sweeps in 1 mM EGCg solution..... 160

Figure D.2. (A) Cell viability depending on EGCg concentration over a period of 4 hours. (B) Optical micrographs of HeLa cells incubated in DMEM- (left panel) or $25 \mu\text{M}$ EGCg in DMEM- for 24 hours. 161

LIST OF TABLES

Table 1.1: Compartmentation of glutathione. Table reproduced from reference ¹. 32

Table 4.1: I_0 , A and r_0 as a function of k_0 for the flat substrate and domed cell. 121

LIST OF ABBREVIATIONS AND ACRONYMS

ABC	ATP-Binding Cassette
ABCC	ATP-Binding Cassette, Sub-Family C (CFTR/MRP)
AC-SECM	Alternating Current Scanning Electrochemical Microscopy
AFM	Atomic Force Microscopy
Au-NP	Gold Nanoparticle
ADP	Adenosine 5'-diphosphate
ATP	Adenosine 5'-triphosphate
BQ	Benzoquinone
CE	Counter Electrode
CMFDA	5-Chloromethylfluorescein Diacetate
EGCg	Epigallocatechine Gallate
FcCH ₂ OH	Ferrocenemethanol
[FcCH ₂ OH] ⁺	Ferroceniummethanol
GSH	Reduced Glutathione
GTC	Green Tea Catechins
HA	Hemagglutinin
HeLa	Adenocarcinoma Cervical Cancer Cells
HeLa-R	Adenocarcinoma Cervical Cancer Cells Overexpressing MRP1
HIV/AIDS	Human Immunodeficiency Virus/Acquired Immunodeficiency Syndrome
HPV	Human Papilloma Virus
HT-29	Human Colon Adenocarcinoma Cells

H ₂ Q	Hydroquinone
MDR1	Multidrug Resistance Gene, Encoding for P-gp
MRP1	Multidrug Resistance Associated Protein
NADP ⁺ /NADPH	Nicotinamide Adenine Dinucleotide Phosphate
NSOM	Near Field Scanning Optical Microscopy
NTN	Neutravidin
Ox	Oxidized Species
PAP	P-aminophenol
P-gp	P-glycoprotein
PO	Peroxidase
RE	Reference Electrode
Red	Reduced Species
RG	Dimensionless Radius of Glass
Ru(NH ₃) ₆ ³⁺	Hexaamineruthinium (III) chloride
Ru(NH ₃) ₆ ²⁺	Hexaamineruthinium (II) chloride
SECM	Scanning Electrochemical Microscopy
SEM	Scanning Electron Microscopy
SG-TC	Substrate Generation-Tip Collection
TEM	Transmission Electron Microscopy
TG-SC	Tip Generation-Substrate Collection
WE	Working Electrode

LIST OF SYMBOLS

Symbol	Description	Units
A	Electrode Surface	m^2
a (<i>Substance</i>)	Activity of Substance	
α_a	Anodic Charge Transfer Coefficient	
α_c	Cathodic Charge Transfer Coefficient	
c	Concentration	mol/l
c^0	Initial Concentration	mol/l
c_{Fc}	Concentration of FcCH ₂ OH	mol/l
D	Diffusion coefficient	m^2/s
d	Tip-to-Substrate Distance	m
d_{CS}	Cell-to-Substrate Distance (Cell Height)	m
d_{TC}	Tip-to-Cell Distance	m
E	Electrode Potential	V
E_0	Electrode Potential at standard conditions	V
F	Faraday Constant (96485)	C/mol
G	Gibb's Free Energy	kJ/mol
i	Current Density	A/m^2
i_0	Exchange Current Density	A/m^2
I	Current	A
I_{norm}, Ni_T	Normalized Current (I_{tip}/I_{ss})	
$I_{ss}, i_{T\infty}$	Measured Microelectrode Current in Bulk	A
I_{tip}, i_T	Measured Microelectrode Current	A
J	Flux	$mol/(m^2 s)$
k_0	Apparent Heterogeneous Rate Constant	m/s
L	Dimensionless Distance (d/r)	
Ni_s	Kinetically Controlled Substrate Current	A
Ni_T^{cond}	Normalized Current over a Conductor	
Ni_T^{ins}	Normalized Current over an Insulator	

Ni_{Tot}	Total Normalized Microelectrode Current	
n	Number of Independent Experiments	
n_e	Number of Electrons Exchanged During Redox Reaction	
n_m	Amount of Reacted Substance	mol
σ	Stress imposed on Microelectrode Tip	Pa
P_s	Péclet Number	
p	Pressure	atm
ρ_{solid}	Density of the Tip Material	(kg/m ³)
r	Radius of Active Material	m
R	Universal Gas Constant (8.314472)	J/(K mol)
RG	Dimensionless Radius of Glass	
t	Time	s
T	Temperature	K
u	Fluid Velocity	m/s
x	Length	m
β	Geometry Factor Constant	
η	Dynamic Viscosity of the Solution	Pa s
η_o	Overpotential	V
$\nu_s (Substance)$	Stoichiometric Factor of Substance	
v_e	Scan Velocity of the Electrode	m/s

ABSTRACT

Complex biological processes, such as the transport of molecules across cell membranes, are often difficult to understand or even to monitor using purely biological methodologies. Investigating these transport processes remains challenging, because biological objects exhibit highly complex chemical composition, target substances exist in small concentrations and studies require the analysis of living samples. Scanning electrochemical microscopy (SECM) is an electrochemical analytical technique, offering the detection of single molecules released from a single cell non-invasively. It does so by detecting electron transfer reactions at a biased microelectrode positioned in close proximity to a target cell.

The presented dissertation investigates and quantifies the efflux of glutathione from human adenocarcinoma cervical cancer cells (HeLa) and a multidrug resistant variant (HeLa-R). Due to its ubiquitous antioxidant and regulatory redox properties, glutathione provides information about the overall cellular redox state. Herein, two methods are proposed to quantify the heterogeneous rate constant (kinetics) in HeLa and HeLa-R by means of SECM. First, the use of both, a cell permeable and a cell impermeable redox mediator during 3D live cell imaging and application of SECM theory leads to a direct comparison of HeLa and HeLa-R cell kinetics. Secondly, SECM line scan imaging at different scan velocities, supported by numerical simulations offers a rapid and convenient alternative solution for the quantitative determination of cellular glutathione efflux. Furthermore, issues related to a long experimental acquisition time during the mediator-based methodology could be resolved.

To apply the SECM scan velocity based glutathione efflux quantification method to a biological relevant model as a proof of concept, the influence of Epigallocatechine gallate (EGCg),

the most abundant catechin in tea, on HeLa cell kinetics is investigated. After exposure to EGCg the cells metabolic response is monitored electrochemically and biochemically over time. Finally, a direct comparison of the two proposed electroanalytical methods is conducted and discussed in the context of current literature. Suggestions are made for future studies and their impact in analytical and medical research is discussed.

RÉSUMÉ

Les processus biologiques complexes, tels que le transport de molécules à travers les membranes cellulaires, sont souvent difficiles à comprendre ou même à observer en utilisant des méthodologies purement biologiques. Enquêter sur ces processus de transport reste difficile, parce que les corps biologiques présentent une composition chimique très complexe, les substances cibles existent en petites concentrations et les études nécessitent l'analyse d'échantillons vivants. La microscopie électrochimique à balayage (SECM) est une technique d'analyse électrochimique permettant la détection de molécules individuelles sécrétées par une seule cellule de façon non-invasive. Cette technique se base sur la détection de réactions de transfert d'électrons à une microélectrode polarisée positionnée à proximité immédiate de la cellule cible.

La thèse présentée étudie et quantifie l'efflux de glutathion à partir de cellules humaines d'adénocarcinome du col de l'utérus (HeLa du cancer) et d'un variant présentant une résistance à de multiples médicaments (HeLa-R). En raison de ses propriétés antioxydantes omniprésentes et de propriétés régulatrices d'activités redox, le glutathion fournit des informations sur l'état redox général de la cellule. Ici, deux méthodes sont proposées pour quantifier la constante de vitesse hétérogène (cinétique) dans des cellules HeLa et HeLa-R au moyen de la SECM. Premièrement, l'imagerie 3D de cellules vivantes en utilisant deux médiateurs redox, un qui est perméable à la cellule et un qui ne l'est pas, et application de la théorie SECM conduit à une comparaison directe de la cinétique cellulaire d'HeLa et d'HeLa-R. Deuxièmement, l'imagerie SECM par balayage linéaire à différentes vitesses, soutenue par des simulations numériques, offre une solution de rechange rapide et pratique pour la détermination quantitative de l'efflux cellulaire du glutathion.

En outre, les problèmes liés à une longue période d'acquisition au cours d'expériences impliquant des médiateurs pourraient être résolus.

Pour prouver le concept, la méthode de quantification de l'efflux de glutathion par SECM a été appliquée à un système biologique modèle, soit les cellules HeLa. L'influence de l'épigallocatechine gallate (EGCg), la catéchine la plus abondante dans le thé, sur la cinétique des cellules est étudiée. Après exposition à l'EGCg, la réponse métabolique des cellules est évaluée par voies électrochimique et biochimique au fil du temps. Enfin, une comparaison directe des deux méthodes électroanalytiques proposées est menée et discutée dans le contexte de la littérature actuelle. La thèse se conclut sur une discussion approfondie concernant les travaux futurs envisagés ainsi que leurs impacts potentiels dans les domaines de la chimie analytique et la recherche médicale.

ACKNOWLEDGEMENTS

The completion of this dissertation is certainly one of the most elaborate, interesting and also frustrating tasks I accomplished so far. This work would not have been possible without the effort and support of many people, I would like to thank and mention here:

My supervisor, **Professor Dr. Janine Mauzeroll**, for accepting the challenge of hosting me as an international graduate student with only minor experience in chemistry seven years ago. Janine, your incredible patience and unbelievable support of my personal life has greatly moulded my professional and personal development. Thank you for understanding all the little mistakes in the lab, sending me on conferences and teaching me the beauty of electrochemistry.

Thanks is also due to **Professor Dr. Borhane Annabi** at Université du Québec à Montréal (UQAM), for introducing me to Janine in 2008 as well as **Professor Dr. Benoit Marsan**, for his understanding and openness for special circumstances that arise when students change the educational system during their studies and for accepting me into the graduate program of biochemistry at UQAM;

Dr. Matthias Geissler and **Dr. Dao Trinh**, for their helpful discussions and support during our collaborative work;

My review committee, **Professor Dr. Amy S. Blum** and **Professor Dr. Gonzalo Cosa**, for accompanying my research and providing helpful comments and ideas during review meetings. And once more Amy, for her interest in challenging side projects;

My colleagues, for many helpful discussions and their friendship. In particular **Isabelle Beaulieu**, for her assistance and translation skills, **Laurence Danis**, for developing and providing

the microelectrodes, **Carolyn Madwar**, for being my library buddy, **Dr. Michael Snowden, Dr. Karl Klinger and Dr. Tomer Noyhouzer**, for making the journey so much more enjoyable.

Our undergraduate student assistants **Charles St. Pierre, Ivon Vassileva**, for their assistance;

Mrs. Chantal Marotte, for her dedicated help as Graduate Program Administrator;

And last, but certainly not least, my husband **Dr. Christian Kuss**, for being such an incredible husband and father to our kids. Thank you, Christian, for your patience, love and also for your brilliant cooking skills. I also thank **my children Theodor and Klara**, for providing the perfect balance between my worlds of accurate and logic science and our crazy reality.

CONTRIBUTION OF AUTHORS

As the presented work represents multidisciplinary collaborative research, details will be given in the following for each publication to outline individual contributions of all collaborators.

Chapter II: Assessment of multidrug resistance on cell coculture patterns using scanning electrochemical microscopy

Published in 2013 in the journal Proceedings of the National Academy of Science of the United States of America, Volume 110, Issue 23, Pages 9249 to 9254 (www.pnas.org/cgi/doi/10.1073/pnas.1214809110).

The design of experiments as well as the acquisition of all experimental data, which includes cell culturing, the development of the cell patterning method (figure 2.1), co-culturing of HeLa and HeLa-R (figure 2.3), validation of the patterns during SECM studies (figure 2.2) and imaging of co-cultures (figure 2.4A and B) in ferrocenemethanol and hexaammineruthinium(III)chloride (figure 2.4C and D), was performed solely by Sabine Kuss (SK). Dr. Daniel Brassard (DB) developed the protocol for the synthesis of the elastomeric through-hole membrane, which was fabricated and oxygen plasma treated according to our needs by Dr. Matthias Geissler (MG) at the facilities of the National Research Council Canada in Boucherville. To extract the heterogeneous rate constant of live cells using a numerical software, such as Matlab. Data treatment in Matlab for the SECM images in FcCH₂OH and [Ru(NH₃)₆]³⁺ was carried out by David Polcari (DP) and a numerical value for cell kinetics was extracted by DP. Furthermore, DP contributed specifically to the modification of figure 2.2A and generated figure 2.4E and F. DP also contributed to the

preparation of manuscript chapter 2.4.4. All co-authors revised, provided comments and agreed to the final version submitted to PNAS.

Chapter III: Forced convection during scanning electrochemical microscopy imaging over living cells: Effect of topographies and kinetics on the microelectrode current

Published in 2013 in the journal Electrochimica Acta, Volume 110, Pages 42 to 48 (<http://dx.doi.org/10.1016/j.electacta.2013.03.149>)

The design and performance of all experiments except the mercury hemisphere (figure 3.1B), data analysis and treatment was performed by SK. Experiments include cell culture, SECM line scans at different velocities across living cells (figure 3.2) as well as a Pt bottom microelectrode embedded into Epoxy (figure 3.1A and C). Dr. Christian Kuss (CK) agreed to perform SECM line scans across a mercury hemisphere deposited onto the Pt bottom electrode following the experimental design and guidance of SK (figure 3.1B). Thereby Prof. Steen Schougaard (SS) kindly provided his lab space and instrumentation. Numerical modelling was performed by Prof. Dr. Dao Trinh (DT), providing figures 3.3 to 3.6 as well as manuscript section 3.4. Manuscript preparation was organized as stated above, with SK as first author and hence providing a complete initial draft and addressing co-authors comments. The authors CK, DT, SS and JM (supervisor and corresponding author) reviewed and edited the draft and all authors agreed to the submission of the manuscript.

Chapter IV: Scanning Electrochemical Microscopy Forced Convection Method for Substrate Kinetics Determination: Method and Theory

Accepted manuscript in the journal of Analytical Chemistry (Manuscript ID: ac-2015-012685), 2015. (DOI: 10.1021/acs.analchem.5b01268).

As the first author of this manuscript, SK designed and performed all experiments (figure 4.1 left panel and insets, figure 4.3A and B, figure C.1 and figure C.2). Data analysis and treatment was also carried out by SK, providing the basis for the numerical modeling. Microelectrodes were fabricated by LD. Numerical modeling on the experimental data in COMSOL was performed by DT, providing figures 4.1 right panel (without insets), 4.2, table 4.1, figure 4.3C, and supporting figures C.3 and C.4, and wrote text section 4.4 as well as parts of the results and discussion section. As the main investigator, SK organized and handled all collaborations, conference calls and provided a complete draft of the manuscript, which received minor corrections from the co-authors DT (corresponding author), LD and JM (supervisor, corresponding author).

Chapter V: Scanning Electrochemical Microscopy Forced Convection Method for Substrate Kinetics Determination: Application to Live Cell Imaging of Human Cancer

Accepted manuscript in the journal of Analytical Chemistry (Manuscript ID: ac-2015-012697), 2015. (DOI: 10.1021/acs.analchem.5b01269).

Design and setup of the experiments as well as their full execution was conducted by SK. Experiments included electrochemical studies on GTC (figure D.1), cell culture, viability studies on cancer cells in the presence of GTC (figure D.2), fluorescent imaging (figure 5.3), and electrochemical studies on the cellular response to stress (figure 5.1). Data analysis and treatment was also performed by SK. Final data was provided to DT for the application of the numerical method established in chapter IV to include a numerical value to the manuscript, shown in figure

5.3. The manuscript was written by SK, including design and generation of figures. Minor corrections were requested by the co-authors DT and JM (supervisor and corresponding author), which were addressed by SK.

CHAPTER I

INTRODUCTION

The following introduction will discuss the principles of electrochemistry as a basis for the analytical electrochemical methods employed in the presented work. The intersection of electrochemistry and biology is introduced by reviewing literature as well as pointing out advantages and limitations of the electrochemical methods in the recognition of biological molecules of interest.

1.1 Scope of the Dissertation

1.1.1 The Redox State of Glutathione and the Overall Redox Environment of the Cell

A mammalian cell, regardless of its tissue origin, displays a highly complex system. Different cell organelles that are maintained by complex signalling pathways and protein-protein-interaction cascades make a mammalian cell a highly involved complex. Thereby, some important cell functions, *e.g.* responsible for cellular defense mechanisms against harmful molecules, or cellular dysfunctions that may cause the development of malignant cancer tissue, still remain not fully understood. The energy needed for building and maintaining cellular structures is mainly provided and balanced by redox processes in the cell and the transport of molecules across cell membranes, both determining the redox environment of a living cell.¹

The term redox environment reflects the sum of the states of a linked set of intracellular redox couples. The term redox state on the other hand, describes the half-cell reduction potential of a specific couple, such as glutathione (GSH) and glutathione disulfide (GSSG). However, in the

case of the glutathione redox couple, its redox state might very well represent the overall cellular redox environment, as its intracellular concentration is much greater compared to the concentration of all other redox couples in a cell.¹

Glutathione is a tripeptide, consisting of three amino acids, namely glutamic acid, cysteine and glycine, which are connected through a peptide bond and a γ -peptide linkage between glutamic acid and cysteine (Figure 1.1).² It is the most abundant and major thiol-disulfide redox buffer of the cell.³ Its intracellular concentration is estimated to 1-11 mM in the cytosol⁴ and varies within different cellular compartments as summarized in table 1.1. The ratio of GSH / GSSG is often used as an estimate of the redox state, whereby a value > 10 is obtained under normal conditions.⁵

As shown in figure 1.1, GSH is synthesized from its three precursor amino acids glutamic acid, cysteine and glycine in the cytosol and requires two ATP-requiring steps. First, L-glutamate and L-cysteine react to γ -glutamyl-L-cysteine in the presence of γ -glutamylcysteine synthetase. In a second step, catalysed by the glutathione synthetase, γ -glutamyl-L-cysteine reacts with L-glycine to GSH.⁶

Because of its cysteine residue, GSH can be oxidized non-enzymatically to its disulfide dimer GSSG by reacting with electrophilic substances, such as free radicals or reactive oxygen species.⁷ Furthermore, glutathione keeps sulfhydryl groups of proteins in their reduced form and hence maintains the thiol redox potential in cells.⁸ Its importance in cell proliferation, its detailed function and metabolism, as well as its oxygen-reduction-pathways have been described previously in literature.^{7,9-13}

A decrease in cellular GSH concentration was shown in response to malnutrition, oxidative stress and pathological conditions.^{5,14} As an example, when GSH reacts with a peroxide, such as hydrogen peroxide, it undergoes a radical redox reaction, which results in the products GSSG and

water. This reaction is catalyzed by the glutathione peroxidase, an enzyme protecting organisms from oxidative damage. During this oxidation process two GSH molecules donate a hydrogen atom each to scavenge hydroxyl radicals resulting from hydrogen peroxide. GSSG can be reduced to GSH by the glutathione reductase and NADPH as electron source or newly synthesized as described above.

Location	GSH [mM]	Reference
Extracellular	0.010	4
	0.800	15
	0.002	16
Cytosol	1 to 11	3,17,18
Mitochondria	5 to 11	19,20
Nucleus	\geq Cytosol	4,21,22

Table 1.1: Compartmentation of glutathione. Table reproduced from reference ¹.

Because of its antioxidant properties and its importance for the cellular redox state, glutathione and its transmembrane transport is the main focus of this dissertation. With the use of electrochemical techniques, specifically Scanning Electrochemical Microscopy (SECM), it is possible to measure the efflux of glutathione from cells. The presented dissertation aims to reach the following major goal:

The establishment of an electroanalytical measure of the glutathione efflux from single human cancer cells and its reliable determination using standard Scanning Electrochemical Microscopy equipment.

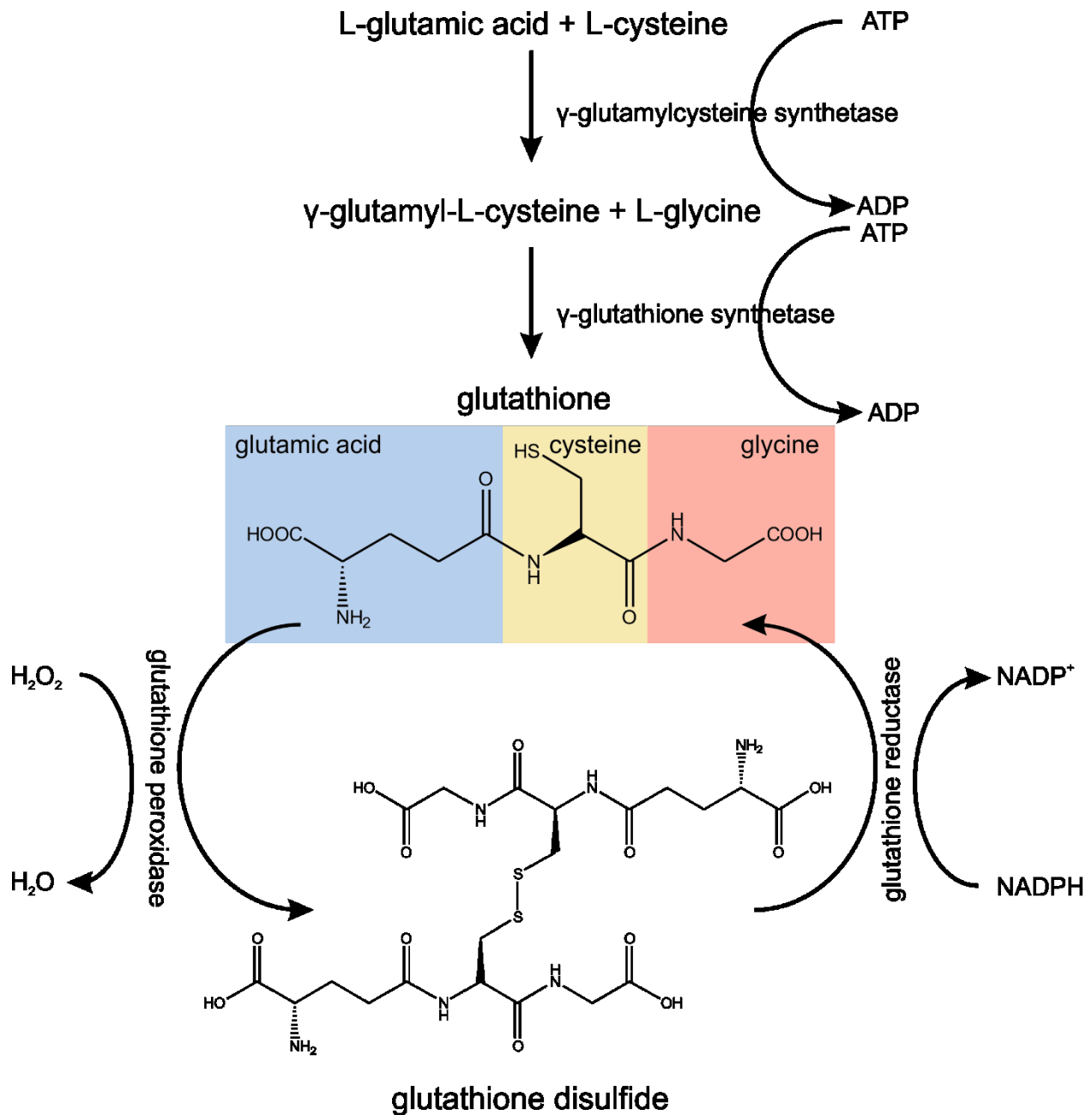


Figure 1.1. Schematic representation of intracellular action of glutathione (GSH) and glutathione disulfide (GSSG). GSH is synthesized from three amino acids. L-glutamic acid reacts with L-cysteine to form γ -glutamyl-L-cysteine, catalyzed by the enzyme γ -glutamylcysteine synthetase. γ -glutamyl-L-cysteine reacts further with L-glycine to GSH in the presence of the γ -glutathione synthetase. GSH can be oxidized to GSSG when reaction with peroxides and be regenerated by the glutathione reductase, whereby NADPH functions as electron donor.

1.2 The Challenge

The analysis of biological systems by electrochemistry is most challenging, since biological objects usually present a highly complex chemical composition. This composition can vary quantitatively and qualitatively by external effects, such as temperature or extracellular solution composition, making analyses in-vitro complicated, as samples are no longer in their natural environment. Furthermore, as often essential substances inside a biological system, such as a cell, are present in very small concentrations. Especially for the analysis of single biological cells, microsensors or microelectrodes have been developed to achieve an appropriate resolution and to interfere with the cell environment as little as possible.²³ Commonly, platinum (Pt) wires or carbon fibers are used for micro- or even nanoelectrode fabrication. Due to the small size of these probes, the current measured remains also relatively low (micro- or picoamper), which requires a delicate and sensitive instrumentation.²⁴

Although only visible on the micrometer scale, living cells are constantly active and changing their position. The mobility of the sample can disturb sensitive current measurements and may considerably complicate data analysis, as the origin of a result may become unclear. Cell immobilization often times leads to cell death or alterations in cell metabolism due to the introduction of toxic substances to the cell environment.^{25,26} The cell's metabolism, defined as the sum of all enzyme catalysed reactions involving organic molecules in living cells²⁷, strongly depends on the environmental conditions. Even, if the cells are not undergoing apoptosis or necrosis, observations of morphological changes can be used as an indicator for metabolic changes.^{28,29} Therefore it is very important during SECM measurements on living cells to closely monitor the target cell's appearance, to simulate its natural environment as best as possible, and to keep the analysis time short.

Another challenge during the analysis of small samples, such as biological cells, with electrochemical techniques is that it is very difficult to understand exactly which feature of the substrate it is that causes the obtained electrochemical current. An active site, a change in topography, or active transport processes through a substrate may result in a similar current behavior, as discussed in detail in section 1.3.4.2. Hence, it is often times necessary to combine SECM with other microscopy techniques or numerical modeling to decouple differences in reactivity and/or topography.

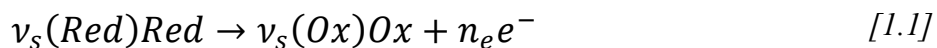
1.3 Scanning Electrochemical Microscopy (SECM)

1.3.1 Principles

Scanning Electrochemical Microscopy (SECM) is the main electrochemical technique employed in the presented dissertation. The instrument principles of an SECM for biological systems are displayed in figure 1.2A. A standard SECM employs micro- or even nano-scale electrodes that are scanned over an electrochemical cell in close proximity to the surface. Such microelectrodes, as shown in figure 1.3, consist of a metal wire that is sealed into a quartz capillary and is connected to a potentiostat by an attached gold pin.³⁰ The microelectrode is mounted onto a motor station, moving in z -direction. An electrochemical cell, which is also fixed to motors, can thereby be controlled in x - and y -direction. The absolute position of the electrode above a sample is insured by close-loop piezo controllers that minimize motor hysteresis.³¹ An incorporated microscope equipped with a camera allows monitoring of samples during measurements, which is useful for the electrode positioning prior to the data acquisition. Sample observation becomes especially important while working with biological samples, such as living cells, as the target's morphology can be observed during the experiment. The whole apparatus is placed on top of a

vibration isolation table and inside a Faraday cage to avoid interference from external electric noise.

SECM is a technique that allows measuring oxidation and reduction (redox) processes at the microscopic scale:



where $\nu_s(\text{species})$ is the stoichiometric factor of the redox species, *Red* is the redox species in its reduced form, *Ox* is the redox species in its oxidized form, n_e is the number of electrons exchanged during redox reaction and e^- is the transferred electrons.

With the use of microelectrodes, these redox processes can be separated in space, whereas the reduction takes place at the cathode, the oxidation at the anode. By applying a potential (or voltage) difference between anode and cathode, the direction and rate of these reactions can be controlled. Consequently, a faradaic (electrochemical) current, consisting of an electronic current, transporting electrons through an external circuit, and an ionic current, transporting ions through the electrolyte, is induced. The electronic current can be measured and correlates to the amount of species transformed per time unit by Faraday's law (1.1):

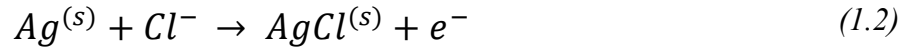
$$\frac{n_m}{t} = n_e \cdot F \cdot I \quad (1.1)$$

Where n_m is the amount of reacted substance (mol), t is the time (s), n_e is the number of electrons transferred per molecule, F is the Faraday constant (96485 C/mol) and I is the current (A).

In the presented studies, a three electrode set up is used (Figure 1.2B). The working electrode (WE), counter electrode (CE) as well as reference electrode (RE) is connected to a low current potentiostat, where the electronic current is measured, commonly in the fA to μ A range.

The presented work was carried out in amperometric mode, in which a potential between WE and RE is controlled, giving rise to an electrochemical current between WE and CE. Inside the potentiostat, an electrometer measures the voltage difference between the RE and WE, while a current-to-voltage-converter compares this potential difference to the chosen potential difference given by the computer. The potentiostat then regulates the power source between WE and CE. A platinum wire can be used as a CE to transfer the collected electrons from the WE into the solution.

A RE is an electrode with a highly stable electrode potential and serves as reference point during SECM measurements. It is important that small current fluxes in the electrochemical cell do not influence the potential of the RE. Silver/silverchloride (Ag/AgCl) REs are ideal references, because of the presence of AgCl, which exhibits low solubility on the surface. Consequently, the Ag^+ concentration remains constant. In our case, at a stable chloride ion (Cl^-) concentration, an Ag/AgCl wire functions as a RE, according to the following half-cell reaction (1.2):



By using a RE, a well-defined potential can be applied to the WE. The electrode potential (E) at 0 current flux defines the thermodynamic driving force for a reaction and can be calculated by the Nernst Equation (1.3):

$$E = E_0 - \left(\frac{RT}{n_e F} \right) \ln \left(\frac{[red]}{[ox]} \right) \quad (1.3)$$

whereas E_0 is the potential of a redox couple under standard conditions ($T= 25\text{ }^\circ\text{C}$, $p= 1\text{ bar}$, $[ox]=[red]= 1\text{ mol/l}$, given in V), R is the universal gas constant ($J/(K\text{ mol})$), T is the temperature (K), n_e is the number of exchanged electrodes, F is the Faraday constant (96485 C/mol) and $[red]$

and $[ox]$ describe the concentrations of the reduced and oxidized species in solution (mol/l). Reactions, that thermodynamically would not take place spontaneously, can be driven electrochemically by applying a potential greater than the respective Nernst potential. The applied potential over or under the Nernst potential is thereby called overpotential η_o .

The increasing magnitude of the overpotential increases the reaction rate according to the Butler-Volmer equation (1.4). The current usually depends on the type, size and geometry of the electrode, the overpotential and the reaction that takes place on the electrode. Furthermore, if the heterogeneous reaction rate at the electrode exceeds the diffusive flux, it depends also on the diffusivity of the species in the electrolyte and the geometry of the surroundings of the electrode. The Butler-Volmer equation (1.4) describes the potential dependence of the current near the equilibrium potential, *i.e.* assuming no diffusion limitation:

$$\frac{i}{i_0} = e^{\frac{\alpha_a n_e F \eta_o}{RT}} - e^{-\frac{\alpha_c n_e F \eta_o}{RT}} \quad (1.4)$$

with the current density i , the exchange current density i_0 , the cathodic and anodic charge transfer coefficients α_c and α_a , n_e is the number of exchanged electrons, F is the Faraday constant (96485 C/mol), R is the universal gas constant (J/(K mol)), T is the temperature (K) and the overpotential η_o .

If a redox reaction occurs spontaneously, the cathode potential is higher than the anode potential. The potential difference between oxidation and reduction reaction ΔE (V) is thus related to the reaction Gibbs' free energy ΔG (kJ/mol) (1.5), where the relationship is described by:

$$\Delta G = -n_e \cdot F \cdot \Delta E \quad (1.5)$$

Here, n_e is the number of exchanged electrons and F is the Faraday constant (96485 C/mol).

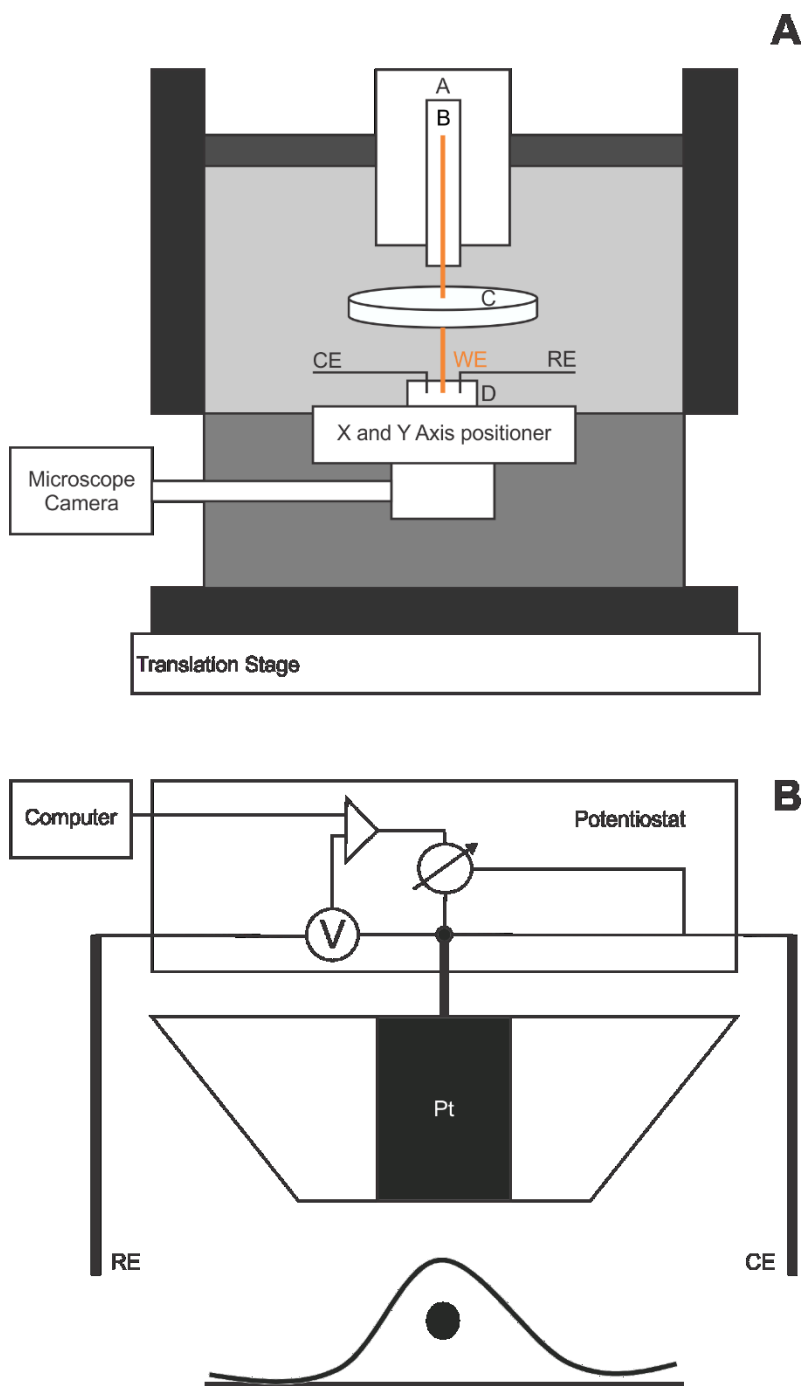


Figure 1.2. Schematic representation of the instrumental design of an SECM. (A) Instrumental set up including Z axis positioner (A), constant distance controller (B), light source (C), electrochemical cell (D) as well as working electrode (WE), counter electrode (CE) and reference electrode (RE). (B) Simplified representation of the low current potentiostat connected to the platinum WE, CE, RE and a computer during imaging of biological samples.

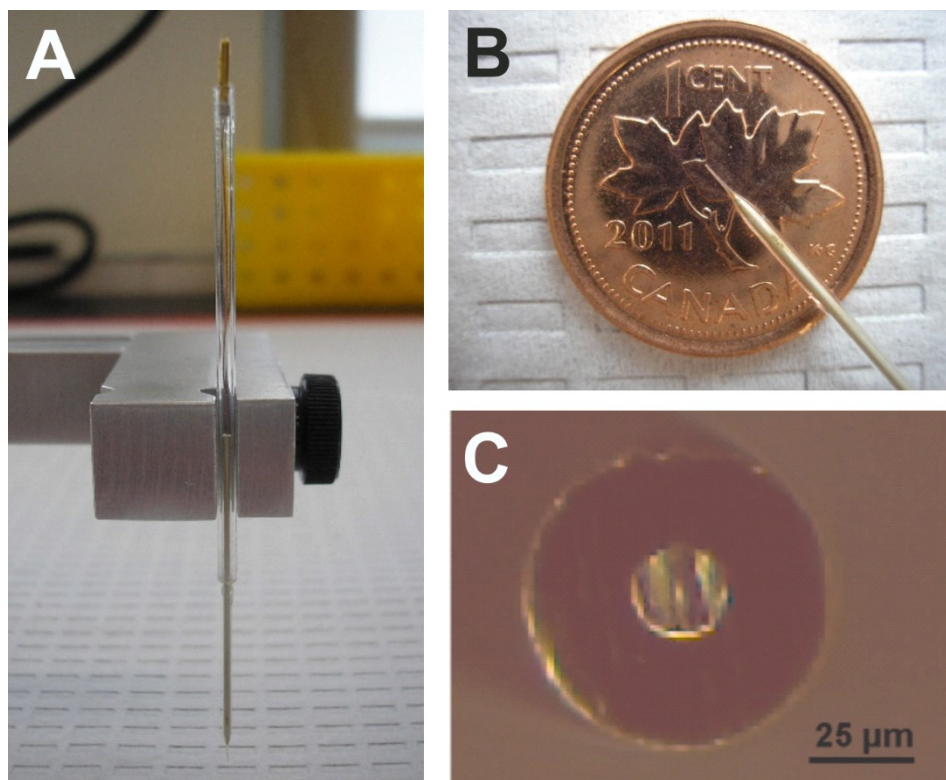


Figure 1.3. Microelectrode used for SECM measurements. (A) Full length of a standard 25 μm Pt microelectrode, (B) size comparison of a microelectrode tip and a Canadian 1 cent coin, (C) top view of the same electrode shown in (A) and (B).

1.3.2 The Stationary Electrode

Without displacement of the microelectrode in solution and far away from the substrate, at distances greater than 200 micrometer from the surface, the current measured is governed by hemispherical diffusion. By choosing a potential far exceeding the standard potential of the dissolved redox mediator, the oxidation or reduction of the redox species is solely dependent on the diffusion of the redox species towards the tip of the microelectrode as long as no significant adsorption or chemical side reactions occur. This scenario is described as diffusion limited condition.³²

Due to the depletion of the redox species at the microelectrode surface, a diffusion layer is established. This describes the concentration gradient of the dissolved redox species from the microelectrode, where the species is depleted, into the bulk solution. The thickness of the diffusion layer depends on the diffusion coefficient of the redox species and the size of the active part of the microelectrode and is usually less than a few hundred micrometers.³³

Due to the hemispherical diffusion, a steady species flux to the microelectrode is established. The steady state current for a microelectrode having a disk geometry (I_{ss}) measured far away from the surface is defined by equation (1.6).

$$I_{ss} = 4n_e F D c r \beta \quad (1.6)$$

In this equation n_e is the number of transferred electrons, F is the Faraday constant (96485 C/mol), D is the diffusion coefficient of the redox mediator (m^2/s), c is the concentration of the redox species in solution (mol/l), r is the radius of the active part of the electrode (m) and β is a tabulated correction factor, which accounts for diffusion of the redox species from above the plane (also called back diffusion) of the microelectrode, which is dependent on the geometry of the probe.³⁴

The steady state current equation (1.6) is derived from Fick's laws (1.7) and (1.8).

$$J = -D\nabla c \quad (1.7)$$

$$\frac{\partial c}{\partial t} = D\nabla^2 c \quad (1.8)$$

with J as the flux of substance ($\text{mol}/(\text{m}^2/\text{s})$), D as the diffusion coefficient (m^2/s), c as the concentration (mol/l) and t as the time (s). To reach the steady state current equation (1.6) Fick's law is solved for a spherical geometry, assuming a constant concentration of 0 of the redox active species at the electrode surface and an infinite volume of bulk solution of constant concentration c .

1.3.3 Approaching a Surface

The specific potential at which a microelectrode is biased to reduce or oxidize a redox species in solution is determined by cyclic voltammetry (CV). Thereby a potential is chosen that lies well in the diffusion limited (steady state) region of the CV (figure 1.4).

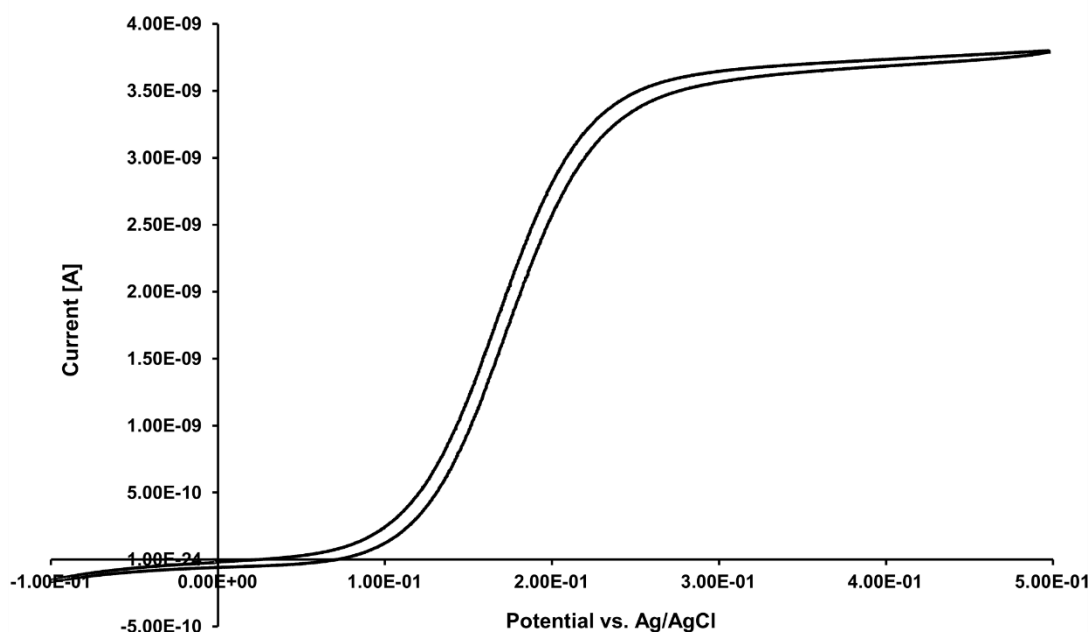


Figure 1.4. Example of a Cyclic Voltammogram for a 25 μm Pt electrode in 1 mM FcCH₂OH in cell medium without serum. The electrochemical potential is linearly swept over a range of 600 mV, whereas a steady state behaviour is shown from 0.3 to 0.5 V vs. Ag/AgCl reference electrode. Therefore a potential of 0.4 V vs. Ag/AgCl reference electrode is chosen for the oxidation of FcCH₂OH.

The dependence of the acquired electrochemical current on the tip-to-substrate distance is called an approach curve. Thereby the biased microelectrode is moved vertically towards the substrate until a desired tip-to-substrate distance is reached, while the electrochemical current is recorded. The presence of the substrate may lead to a reduction of diffusive flux from the bulk, and increase diffusive flux of species that originate from the substrate.

1.3.3.1 SECM Operation Modes

As shown in figure 1.5, SECM employs different operation modes: Tip generation-substrate collection (TG-SC), substrate generation-tip collection (SG-TC) as well as two feedback modes. In TG-SC mode (Figure 1.5A), an electroactive species is generated at the microelectrode tip and collected at the substrate. In this case the reactant diffuses to the substrate and undergoes a reaction at the surface. The recorded current can therefore be dependent on time or the decreasing tip-to-substrate distance.³⁵ In SG-TC mode (also figure 1.5A), a species, produced by the substrate, diffuses towards the electrode where it is collected by the biased tip. In this case the substrate is rather large, producing a thick diffusion layer. In this case, no steady state current can be achieved and sophisticated data analysis is required to extract quantitative results.³⁶

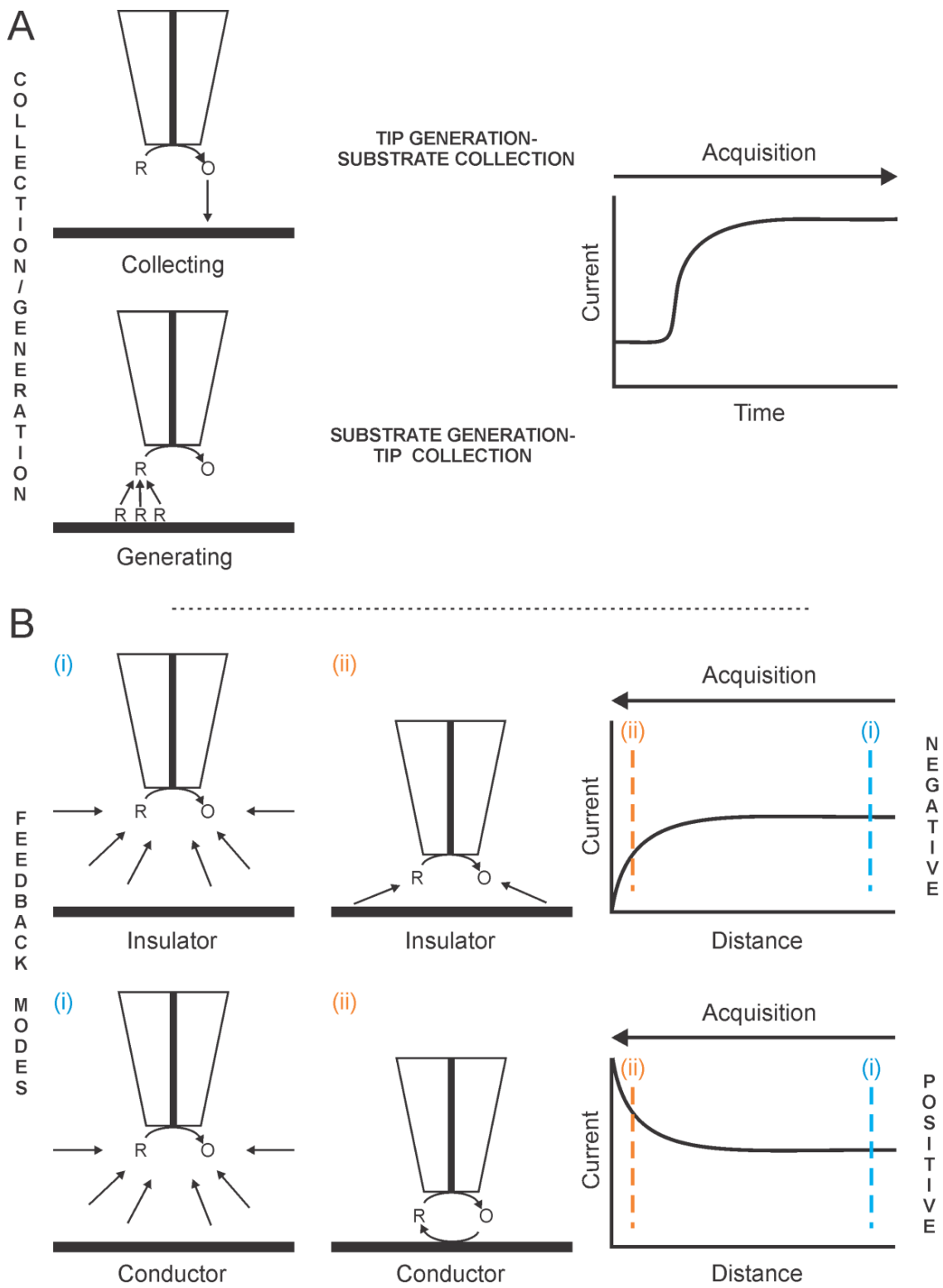


Figure 1.5. Representation of different operation modes during SECM. (A) Collection/Generation modes as well as (B) feedback modes are presented.

The TG-SC as well as the SG-TC mode is not subject of the presented work, but have been reviewed and the interested reader can refer to ³⁷⁻³⁹. Here, main focus will be put on the feedback mode.

In feedback mode (Figure 1.5B), far from the substrate (as explained in section 1.3.2), the electrochemical current magnitude is commonly defined by the diffusive flux of dissolved redox mediator to the tip (Figure 1.5B (i)). When approaching an electrical insulator, the diffusion of the redox species is hindered by the physical presence of the substrate (Figure 1.5B (ii)). As a result, the measured current decreases with decreasing tip to substrate distance. This behaviour is called negative feedback and is described as a numerical approximation in literature³⁴:

$$Ni_T^{ins} = \frac{\left(\frac{2.08}{RG^{0.358}}\right)\left(L - \frac{0.145}{RG}\right) + 1.585}{\left(\frac{2.08}{RG^{0.358}}\right)(L + 0.0023RG) + 1.57 + \frac{\ln(RG)}{L} + \left(\frac{2}{\pi RG}\right)\ln\left(1 + \frac{\pi RG}{2L}\right)} \quad (1.9)$$

where Ni_T^{ins} (A) is the normalized current at the microelectrode over an insulating substrate, RG is the dimensionless radius of the glass and L is the dimensionless distance (tip-to-substrate distance divided by the radius of the active area of the microelectrode).

In contrast, when approaching an electrically conducting substrate the measured current increases with decreasing tip to substrate distance due to the regeneration reaction of the redox mediator at the electrode's tip. This effect is called positive feedback. This behaviour is described as the analytical approximation:

$$Ni_T^{cond} \approx \alpha(RG) + \frac{1}{\beta(RG)} \frac{\pi}{4ArcTanL} + \left(1 - \alpha(RG) - \frac{1}{2\beta(RG)}\right) \frac{2}{\pi} ArcTanL \quad (1.10)$$

$$\alpha = \ln 2 + \ln 2 \left(1 - \frac{2}{\pi} \text{ArcCos} \frac{1}{RG} \right) - \ln 2 \left[1 - \left(\frac{2}{\pi} \text{ArcCos} \frac{1}{RG} \right)^2 \right] \quad (1.11)$$

where Ni_T^{cond} (A) is the normalized current acquired over a conductor, RG is the dimensionless radius of the glass and L is the dimensionless distance.

Furthermore, an analytical approximation for substrate kinetically limited behaviour (Ni_T) is given as:

$$Ni_T(L, RG, \kappa) \approx Ni_T^{cond} \left(L + \frac{1}{\kappa}, RG \right) + \frac{Ni_T^{ins}(L, RG) - 1}{(1 + 2.47RG^{0.31}L\kappa)(1 + L^{0.006RG+0.113}\kappa^{-0.0236RG+0.91})} \quad (1.12)$$

where RG is the dimensionless radius of the glass and L is the dimensionless distance and κ is the normalized rate constant.

These equations can be used to perform data treatment (fitting of experimental data) in software, such as Matlab, as applied in chapter II.

These feedback modes are commonly used to evaluate the tip-to-substrate distance or to monitor cellular function.⁴⁰ Using SECM feedback modes it is possible to monitor molecules, expelled or consumed by a biological cell, as it is subject in the presented work.

1.3.4 The Scanning Electrode

1.3.4.1 SECM Line Scans and Imaging

Before a sample, such as a cell, can be imaged the microelectrode needs to be positioned at a desired tip-to-substrate distance above the plastic surface. Therefore the biased microelectrode is brought manually to a tip-to-substrate distance of about 200 μm , by using the SECM integrated camera and motors. The SECM instrument then approaches vertically the plastic substrate at a

velocity of 1 $\mu\text{m/s}$ and is stopped manually when the current value reaches a minimum. In addition, the approaching microelectrode is constantly observed through the SECM camera and the moment of surface contact can also be very well recognized visually. To reach a desired tip-to-substrate distance (in most cases 12 μm) the microelectrode is pulled back by the SECM motors. Generally, the SECM image origin is roughly set 100 μm laterally to the left of a target cell.

The investigation of cell samples using SECM feedback modes can be carried out in line scan or 3D imaging. During SECM imaging, the microelectrode is rastered laterally across a surface at a chosen tip-to-substrate distance. Line scans can be performed by moving the tip in x-direction while biasing at a defined potential and recording the current (figure 1.6A). By recording an array of several line scans in y-direction one obtains a 3D image (figure 1.6B).

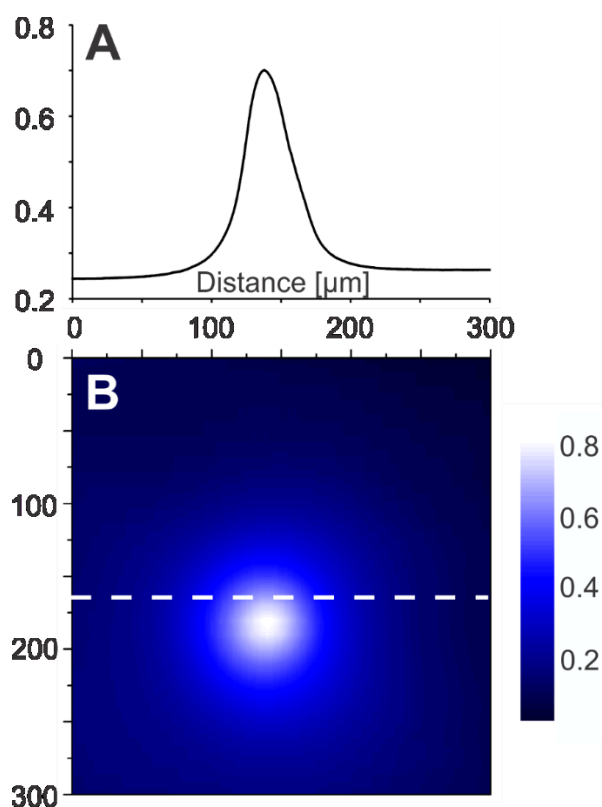


Figure 1.6. Options of imaging in SECM (A) Representation of a line scan profile, taken from (B) a 3D image of a 300 μm by 300 μm scan area. The dotted line indicates the extracted line scan.

As described before, at the diffusion limiting current, the measured electrochemical current at a microelectrode is governed by the flux of species in solution to the electrode tip. This flux can be composed of three modes: diffusion, migration and convection. Fick's diffusion describes the movement of a species under the influence of a gradient (∇) of the concentration. This mode occurs by a "random walk" process and leads to the homogenization of a solution. The governing Fick's equations have already been introduced and Fick's first law can also be found as component of the mass transport equation. Migration on the other hand is the movement of a charged species under the influence of an electric field, whereas convection describes stirring or hydrodynamic transport of a species.⁴¹ The flux J of a species j ($\text{mol s}^{-1} \text{cm}^{-2}$) is the sum of these three terms and is expressed by the mass transport equation (1.13):

$$J_j = \underbrace{-D_j \nabla c_j}_{\text{Diffusion}} - \underbrace{\frac{n_e j F}{RT} D_j c_j \nabla \phi}_{\text{Migration}} + \underbrace{c_j v}_{\text{Convection}} \quad (1.13)$$

where D is the diffusion coefficient of a redox species j in solution (m^2/s), c is the concentration of the redox species j (mol/l), n_e is the number of electrons transferred, F is the Faraday constant (96485 C/mol), R is the Universal Gas Constant $J/(\text{K mol})$, T is the temperature (K), $\nabla \phi$ is the gradient of an established electric field and v is the velocity of the liquid (m/s). During the presented studies the use of an inert supporting electrolyte, usually KCl diminishes any electric field as the latter leads to a charge separation among these ions. A supporting electrolyte is commonly added at a much higher concentration than the electroactive species. The K^+ and Cl^- do

not participate in the reactions, but they carry most of the migration current in solution; hence this term can be neglected and the general flux equation for species j (1.14) becomes:

$$J_j = -D_j \nabla c_j + c_j v \quad (1.14)$$

with J as the flux of a species j ($\text{mol s}^{-1} \text{cm}^{-2}$), D as the diffusion coefficient of a redox species j in solution (m^2/s), c as the concentration of the redox species j (mol/l) and v as the velocity of the liquid (m/s).

It is important to distinguish between natural convection that occurs due to temperature induced density gradients in solution, and forced convection that results from the movement of a solid, *e.g.* the microelectrode during data acquisition, through the solution. The movement of the liquid is influenced by gradients of the flow and pressure, which are induced by the moving solid. The resulting flow velocity fields can be calculated by numerical simulations.⁴² Its influence of convection on the microelectrode current signal and its usefulness in the determination of a sample's kinetic rate in chapters 3 and 4.

1.3.4.2 Understanding the Current Behaviour

When investigating samples, exhibiting complex topographical features or are of unknown reactive nature, it becomes difficult to understand what exactly causes the obtained electrochemical current. For example, just by looking at a current behavior, it is difficult to determine if an increase in current is due to an active site, a change in topography, or the permeability or transport through a substrate. As illustrated in figure 1.7, the active flux of a species generated at a substrate may overcompensate the hindered diffusion from the presence of the surface (Figure 1.7A). Furthermore, while in the negative feedback region close to the sample, a

change in topography might also be responsible for a less negative feedback current depending on the tip-to-substrate distance (Figure 1.7B). Also, an active or diffusive transport through a permeable surface, such as a cell membrane, can also cause an increase in measured current (Figure 1.7C).

In order to decouple current contributions resulting from topography and reactivity, it is often times necessary to combine SECM with other microscopy techniques, such as Atomic Force Microscopy.^{43,44} The development of a constant distance, also called shear force, mode for SECM displays an option to distinguish between reactivity and topography current contributions. Although such approaches are promising, they require expensive and complex experimental equipment. Numerical modeling displays an attractive alternative, which is explored in the presented dissertation.

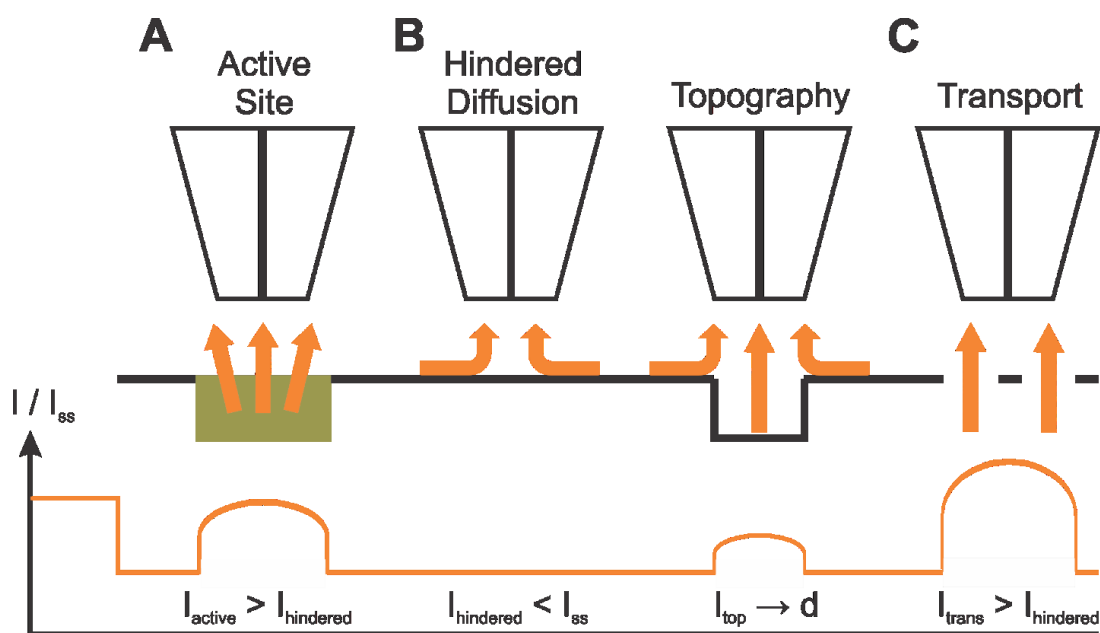


Figure 1.7. Reactivity and topographical contributions to the measured electrochemical current. (A) Diffusion of a redox species from an active site of the substrate. (B) Change in topography, allowing an increase in diffusion of the redox species towards the electrode. (C) An active flux of redox species towards the microelectrode through a permeable surface.

1.3.4.3 Modes of Imaging

As presented in figure 1.8, there are two imaging modes available during SECM analysis. In constant height imaging mode (Figure 1.8A), the electrode moves laterally in *x*- and *y*- direction across a sample, while keeping the initial height during data acquisition. In this case, the topography of the sample changes the tip-to-sample distance. Due to the relatively simple instrumental set up, SECM instruments measuring in constant height are broadly available and used since 1989.⁴⁵⁻⁴⁷ A major disadvantage of scanning in constant height mode is that a slope correction needs to be performed during measurements or data treatment, due to the fact that no adjustment in tip-to-substrate distance can be conducted during SECM imaging. In the past, there was no method available to successfully decouple information about topography and reactivity during constant height imaging. Scanning probe microscopy approaches to control the tip-to-sample distance in the past have been applied in near field scanning optical microscopy (NSOM)⁴⁸ and AC-SECM.⁴⁹⁻⁵² In constant distance mode (Figure 1.8B), the electrode's tip is stimulated by a dither piezo crystal to a vibration at its resonance frequency, whereas a receiver piezo crystal records the electrode's vibration. In close proximity to the surface (about 200 nm above the substrate) increasing shear forces can be observed between the medium and the electrode's tip. Such forces lead to an alteration of phase and amplitude of the recorded vibration at the receiver piezo. This effect is used as a feedback signal in order to keep the same tip-to-sample distance during the electrochemical measurement.⁵³ In order to realize this imaging mode, different approaches have been conducted. Schuhmann and co-workers first introduced a so called "shear force mode" to SECM by recording the amplitude damping of a vibrating tip.⁵⁴ Since then, constant distance imaging was carried out using a laser and split photodiode⁵⁵, tuning fork positioning systems^{48,56,57}, non-optical shear force modes⁵⁸⁻⁶⁰ or even using a phase-controlled feedback

mechanism⁶¹. Employing the constant distance imaging mode the issue of a slope in the target substrate can be overcome, however, this instrumental set up is difficult to realize and many additional parameters, such as the potential influence of the vibrating tip on a biological cell as well as the disturbance of the liquid by the electrode's vibration, have to be considered in order to achieve reproducible and reliable results.

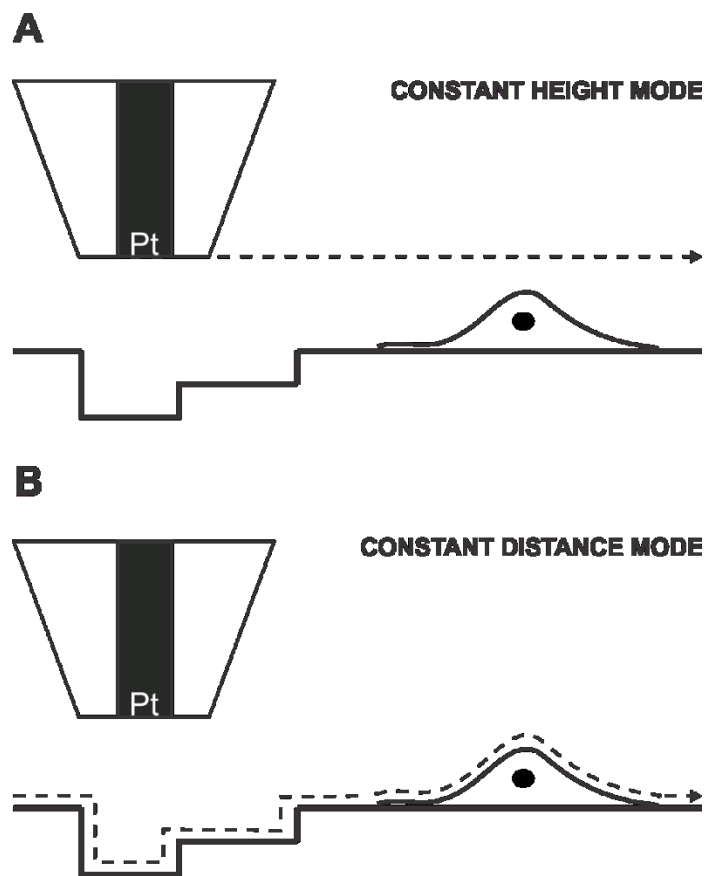


Figure 1.8. Schematic representation of the imaging modes during SECM. (A) Constant height mode, whereas the electrode always keeps the same height above the substrate. (B) Constant distance mode. The electrode keeps the same tip-to-substrate distance at all times.

1.3.5 Numerical Modeling for SECM

SECM signals can be predicted, and the origin of experimental features can be explained using finite element modelling. A commonly used software for this purpose is COMSOL. Here,

partial differential equations can be solved in a 5 step procedure. First, the geometry of the studied system is defined. This includes size parameters, such as electrode dimensions or tip-to-substrate distance, as well as the fluid region between the microelectrode and a surface, where the diffusion processes and reactions happen. Second, partial differential equations describe processes for diffusion, migration and convection, such as the mass transport equation (1.13), including Fick's laws (1.7 and 1.8), as a general equation for the flux. Third, boundary conditions are defined, such as gradients of a redox species in solution. Furthermore, kinetic values are set, to estimate the rate at which a redox species is converted at the microelectrode. Fourth, a mesh is designed, which expresses the numerical steps in space (and time, if the system is time dependent) at which partial differential equations will be solved. In a fifth and final step, algorithms are chosen that are used to solve the partial differential equations and the numerical modelling can be executed in COMSOL for different parameters or starting conditions.

1.3.6 Introducing Convection

In contrast to laminar flow, where the fluid flows in parallel layers, without disturbances between the layers, turbulent flow describes chaotically mixing fluid movements. Here, inertial forces are dominant that can introduce vortices in the fluid path. In general, the Reynolds numbers (Re), shown in equation (1.15) are used as a dimensionless quantitative measure to estimate flow patterns in different fluid situations. Low Re thereby represent laminar flow, whereas high Re describe turbulent flow occurrences.

$$Re = \frac{\textit{inertial forces}}{\textit{viscous forces}} = \frac{\rho v L}{\eta} \quad (1.15)$$

where ρ represents the density (g/cm^3), v is the velocity, L the travelled length of the fluid (m) and η represents the dynamic viscosity of the solution (m/s).

In turbulent liquids, it is important to distinguish between natural convection and forced convection. Natural convection is usually due to density differences arising from temperature gradients, which results in a disturbance of the fluid motion. Forced convection is generated by external sources, such as active stirring of the solution, or as in our case, the displacement of the microelectrode during SECM line scans. In general, it is assumed that the diffusion of molecules from a substrate to the tip (tip-to-substrate distance d (m)) happens on the order of milliseconds and occurs faster than the time it takes for the electrode to scan across a substrate, following equation (1.16):

$$d = \sqrt{Dt} \quad (1.16)$$

where D is the diffusion coefficient of a species in solution (m^2/s) and t represents the time (s).

The consequences associated with the displacement of the microelectrode was first examined by Kanoufi et al.⁴² They made use of hydrodynamic finite element modelling and concluded that at low scan velocities of an SECM tip, the induced mass transport to the electrode was negligible. However, the measured current was perturbed by convective flow at higher scan rates. The presented PhD work applies this knowledge to substrates having non-uniform topography and reactivity, specifically human cancer cells.

1.4 Biology meets Electrochemistry

1.4.1 Cellular Transmembrane Export of Molecules

The transport of molecules across cell membranes is one of the most fascinating and important features a living cell needs to display in order to thrive and prosper or even just to survive.⁶² In fact, in some organisms, such as *Escherichia coli*, 15% to 30% of all genes encode membrane proteins⁶³ and some cells of mammals use up to two thirds of their metabolic energy for membrane transport processes⁶². A hydrophobic cell membrane allows cells to maintain the concentration of solutes in the cytosol that differs from the concentration in the extracellular liquid and from concentrations in other compartments of the cell. In order to take up nutrition, expel metabolites or to regulate the intracellular concentration of different ions, cells need to be able to transport water soluble molecules through their cell membranes^{64,65}. In contrast to water and non-polar molecules, which diffuse easily across a cell membrane, polar molecules, such as ions, amino acids, nucleotides or cell metabolites, are transported by transport proteins of the cell membrane. A variety of different transporters exists in all biological membranes, whereas each protein transports a certain class of molecules or often just specific molecules⁶⁶. On one hand there are channel-proteins that function as pores that open and allow the transport of solutes with certain size and charge. On the other hand, carrier-proteins bind target molecules to specific binding sites and due to a change of conformation of the carrier, the target can be guided through a pump, while remaining unmodified⁶⁴. Carrier-proteins are often linked to an energy source to transport molecules⁶⁷. Hence, cells are using three main mechanisms to actively transport substances across membranes: Coupled Carrier (transport of a solute with opposing flux of another), Light-driven Pumps (transport linked to luminous energy) and Adenosine 5'-triphosphate (ATP) -driven Pumps

(transport linked to the hydrolysis of ATP)⁶². The latter, also called ABC-transporter family, is of specific interest for us, due to its clinical importance.

ABC transporters in Eukaryotes are known to be specialized on the export of substances from living cells. Mutations of genes associated with ABC transporters lead to severe consequences, such as the development of Cystic Fibrosis^{68,69}. If a transporter is able to expel pharmaceutical products from the cytosol, it can lead to a resistance against cytotoxic substances used to treat Malaria⁷⁰ or in chemotherapy for cancer treatment⁷¹⁻⁷³. In fact, studies have shown that the Multidrug Resistance Associated Protein 1 (MRP1), a member of the ABC sub-family C (ABCC), is an independent prognostic indicator and its expression is strongly predictive of the survival rate of cancer patients⁷⁴. In 2007, 70 % of ovarian cancer patients exhibited multidrug resistance in Canada and the United States, lowering their survival rate to 10-30 %.⁷⁵ Also, MRP1 plays an important role in childhood cancer relapse as shown in acute lymphoblastic leukemia⁷⁶.

1.4.2 Model Cell Types and Cell Culture Conditions

As membrane transport plays such an important role in cancer development, human adenocarcinoma cervical cancer cells (HeLa) are subject to the presented work. Taken from a cancer patient, Henrietta Lacks, who died in 1951 from the disease, it became one of the most studied and commonly used cancer cell lines in biomedical research.⁷⁷ Containing the human papilloma virus (HPV), they are ranked biosafety level 2. Unfortunately, HPV virus infections and incidence of adeno/adenosquamous cell carcinomas have been reported at an upward trend in North America and Canada⁷⁸ and much effort is done in the understanding of the disease and its treatment.^{79,80}

HeLa cells are adherent epithelial cells that present a triangular morphology when attached to a surface (Figure 1.9A). The cell's diameter is of 25-50 μm , whereas we estimate its height to be 7-10 μm . To simulate the physiological environment of the human body, these cells are grown in culture medium, such as Dulbecco's Modified Eagle Medium, supplemented with heat inactivated fetal bovine serum (the cells' nourishment) and antibiotics to reduce the risk of culture contamination. Similar to the human body's temperature, cells are incubated at 37 °C and 5 % CO_2 . Alterations of the genotype very often affect the cell's phenotype as well.

During electrochemical measurements bovine serum was removed, to allow maximum uptake of substances, such as green tea catechins, presented in chapter V. Furthermore, by removing serum from the electrolyte solution, blockage of the microelectrode due to oxidizable species in serum can be avoided.⁸¹

A multidrug resistant variant of HeLa cells (HeLa-R) has been chosen as a second model system in the presented work, due to the above mentioned clinical importance of these organisms. In case of HeLa-R, the insertion of small antigenic hemagglutinin (HA) epitopes into different transmembrane domains in the amino-terminal half and the carboxy-terminal half of the multidrug resistance associated protein 1 (MRP1) lead to drug resistance in these cells.^{82,83} The cells exhibit a more circular and dense shape and prefer to grow in colonies, in contrast to the HeLa wild type cells (Figure 1.9B).⁸⁴

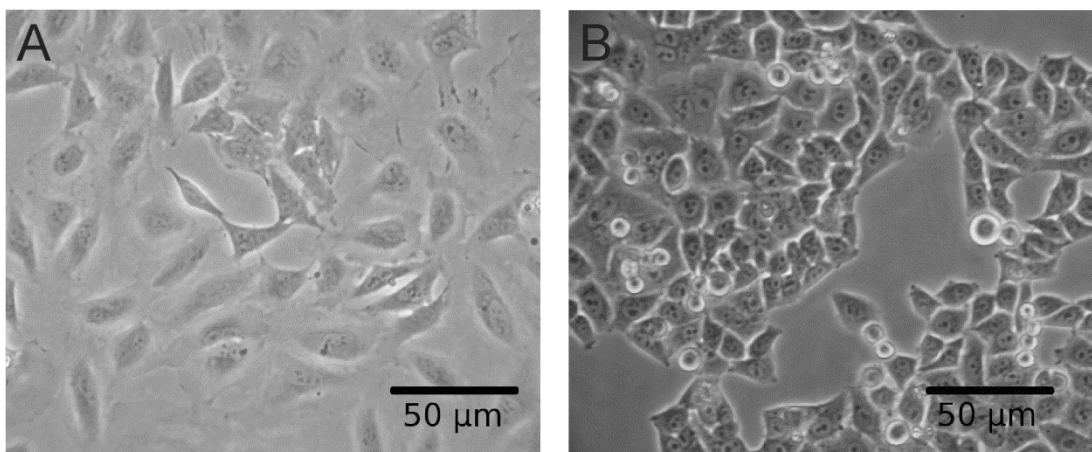


Figure 1.9. Optical micrographs of cell cultures. (A) HeLa and (B) HeLa-R.

1.4.3 Multidrug Resistance

The only difference between the above introduced cell lines is the overexpression of the MRP1 protein and hence, the exhibition of multidrug resistance, which makes therapy less efficient and the positive outcome of cancer treatment in general uncertain.⁷⁵ Such an obstacle is often related to multidrug resistance, which is reported to occur in a broad range of cancer types, such as kidney cancer, colon cancer or leukemia.⁷¹ As shown in figure 1.10, a multidrug resistant cancer cell is able to defend itself towards drugs by expelling harmful molecules rapidly from the cell, making chemotherapeutic treatment inefficient. Multidrug resistance is due to the over expression of certain molecules belonging to the ABC-transporters. P-glycoprotein (P-gp) as well as the multidrug resistance associated protein 1 (MRP1) are two proteins of this family. The over expression of the multidrug resistance gene (MDR1) results in the excessive production of P-gp and with that chemoresistance in cells. The mechanism that causes the expression of P-gp is roughly understood and reported in literature.⁸⁵ This mechanism involves the glucosaminoglycan hyaluronan, which is known to play an important role in wound repair as well as in cancer metastasis. However, the development of multidrug resistance caused by MRP1 remains unclear.

Hence, studies in the presented dissertation focus on human cancer cells that are not overexpressing P-gp, but MRP1. The overexpression of MRP1 also influences the intracellular content of glutathione, which importance is discussed in chapter 1.1.1.

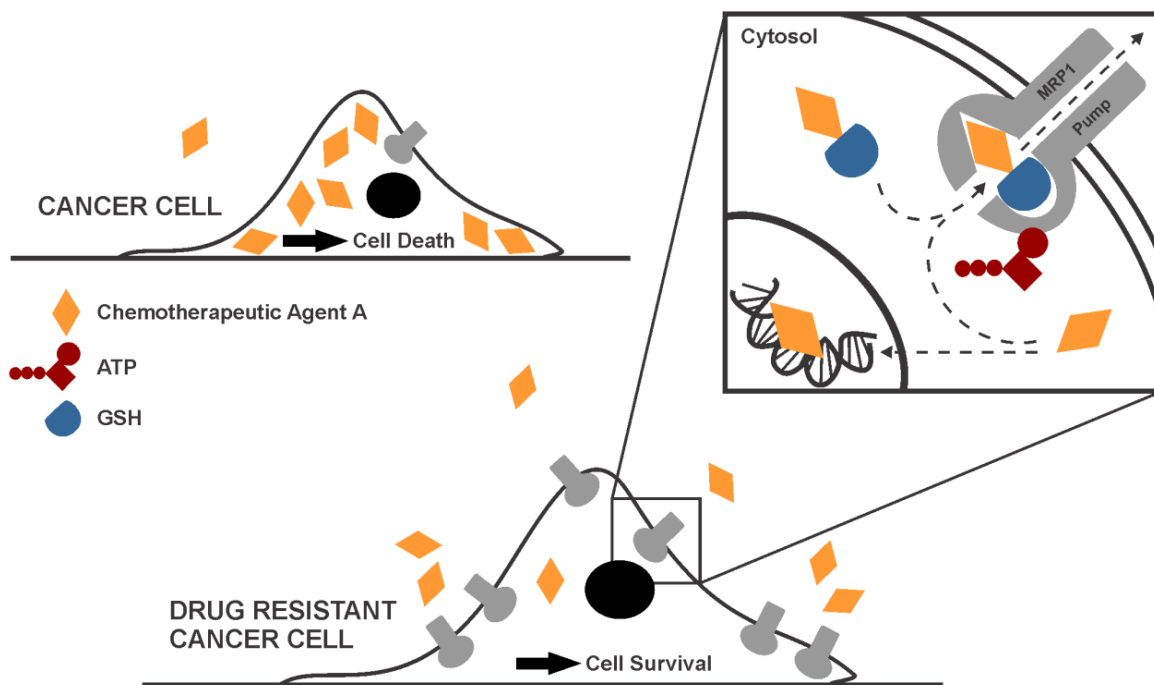


Figure 1.10. Schematic representation of multidrug resistance in cancer cells. Exposure to chemotherapeutic drugs usually leads to cell death in cancer. In drug resistant cells, however, a drug can be transported from the cell directly or in conjugation with GSH through active MRP1 pumps.

1.4.4 Redox Mediators for Biological SECM Studies

To study the above introduced biological cells using SECM, two commonly used redox mediators have been employed, namely Hexaammineruthenium(III)chloride ($[\text{Ru}(\text{NH}_3)_6]^{3+}$) and ferrocenemethanol (FcCH_2OH). Previous cell studies involving these two redox mediators have been performed and are published in literature.⁸⁶ Advantages related to the use of $[\text{Ru}(\text{NH}_3)_6]^{3+}$ and FcCH_2OH include solubility in water, commercial availability, a single electron process during

their oxidation and reduction and absence of material deposition on the biased microelectrode. Furthermore, the redox mediator cell toxicity has been evaluated by flow cytometry and no decline in cell viability was found over an incubation period of up to 4 hrs.⁸⁷ Due to its cell impermeable nature, $[\text{Ru}(\text{NH}_3)_6]^{3+}$ provides information about the topography of the sample during SECM imaging. A decrease in microelectrode current, due to the hindered diffusion of $[\text{Ru}(\text{NH}_3)_6]^{3+}$ towards the tip of the electrode, indicates thereby an elevated substrate feature. FcCH_2OH (Figure 1.11) on the other hand, is cell permeable.⁸⁷ Based on flow cytometry experiments, using 5-Chloromethylfluorescein Diacetate (CMFDA), an intracellular increase in GSH in the presence of FcCH_2OH was discovered.⁸⁷ CMFDA is a colorless, non-fluorescent molecule that passes freely through the cell membrane. Inside a cell it binds GSH and is converted to a green fluorescent dye by intracellular esterases, emitting light at a wave length of 512 nm. Similar flow cytometry experiments, performed with the oxidized form $[\text{FcCH}_2\text{OH}]^+$ did not alter intracellular GSH concentration. Considering as well a clear positive feedback using the FcCH_2OH mediator, compared to the cell impermeable RuHex during SECM experiments, a regeneration model was established. Figure 1.10 illustrates this mechanism reported previously⁸⁷, where FcCH_2OH is electrochemically oxidized at the biased microelectrode surface. It was shown that FcCH_2OH passively diffuses into the cell, where it promotes the intracellular generation of GSH, leading to an alteration of the GSH to GSSG ratio. As a result, GSH is expelled from the cell at an enhanced rate and reacts outside the cell with FcCH_2OH^+ , which is generated at the microelectrode surface. The reaction of GSH with FcCH_2OH^+ results in the oxidation of GSH to GSSG, regenerating FcCH_2OH which can again be oxidized at the microelectrode surface. These interactions provide the basis of the presented electrochemical detection of a cell's redox environment, as glutathione is a major antioxidant in mammalian cells.

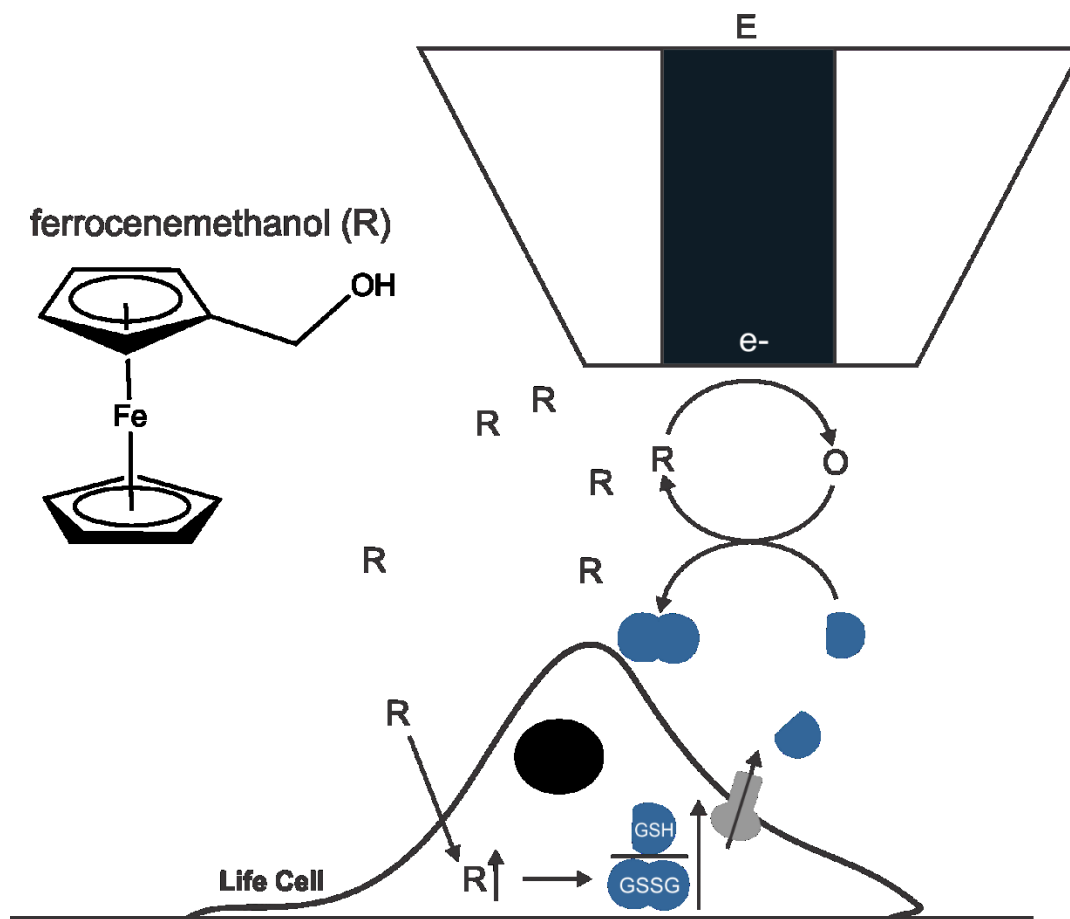


Figure 1.11. Schematic representation of the FcCH_2OH and glutathione relationship. FcCH_2OH reacts with intracellular GSSG to generate GSH, which is expelled from the cell and regenerates FcCH_2OH .

1.4.5 Homogeneous and Heterogeneous Reactions

All processes occurring during SECM live cell analysis can be classified in homogeneous and heterogeneous reactions. A homogeneous reaction takes place in one single phase (liquid, solid, gas), whereas heterogeneous reactions occur at an interphase of different phases. As shown in figure 1.12, the intracellular promotion of GSH generation, as well as the oxidation of GSH to GSSG by $[\text{FcCH}_2\text{OH}]^+$ outside of the cell, are considered homogeneous reactions as they take place in the liquid phase. The oxidation of FcCH_2OH to $[\text{FcCH}_2\text{OH}]^+$ at the microelectrode,

however, takes place at the interphase of the buffer solution and the microelectrode surface, and is therefore considered a heterogeneous reaction. The heterogeneous reaction at the microelectrode is depending on the diffusion of $[\text{FcCH}_2\text{OH}]^+$ to the surface of the cell and the back diffusion of FcCH_2OH to the microelectrode. Thereby the assumption is made that the reaction of GSH with $[\text{FcCH}_2\text{OH}]^+$ happens fast and without GSH diffusing far from the cell surface, effectively leading to a flux of FcCH_2OH from the cell surface towards the microelectrode. Accordingly, the origin of this experimentally measured flux can be approximated as heterogeneous kinetics by numerical simulations. The ability to regenerate the redox species is expected to vary among different cell types, as the intracellular GSH content may differ or the efflux rate might be altered due to the varying expression of membrane pumps and channels.^{82,83} Furthermore, as cell metabolism is strongly dependent on its environment, such as the availability of nutrients, temperature of the solution, etc, the heterogeneous kinetics are also expected to change upon changes of the environment or induction of stress, due to the exposure to harmful molecules.

Acquiring quantitative information about reaction rate kinetics based on the GSH efflux rate of cancer cells, could lead to a more effective drug screening and development that could ultimately impact the survival rate of a large number of cancer patients.

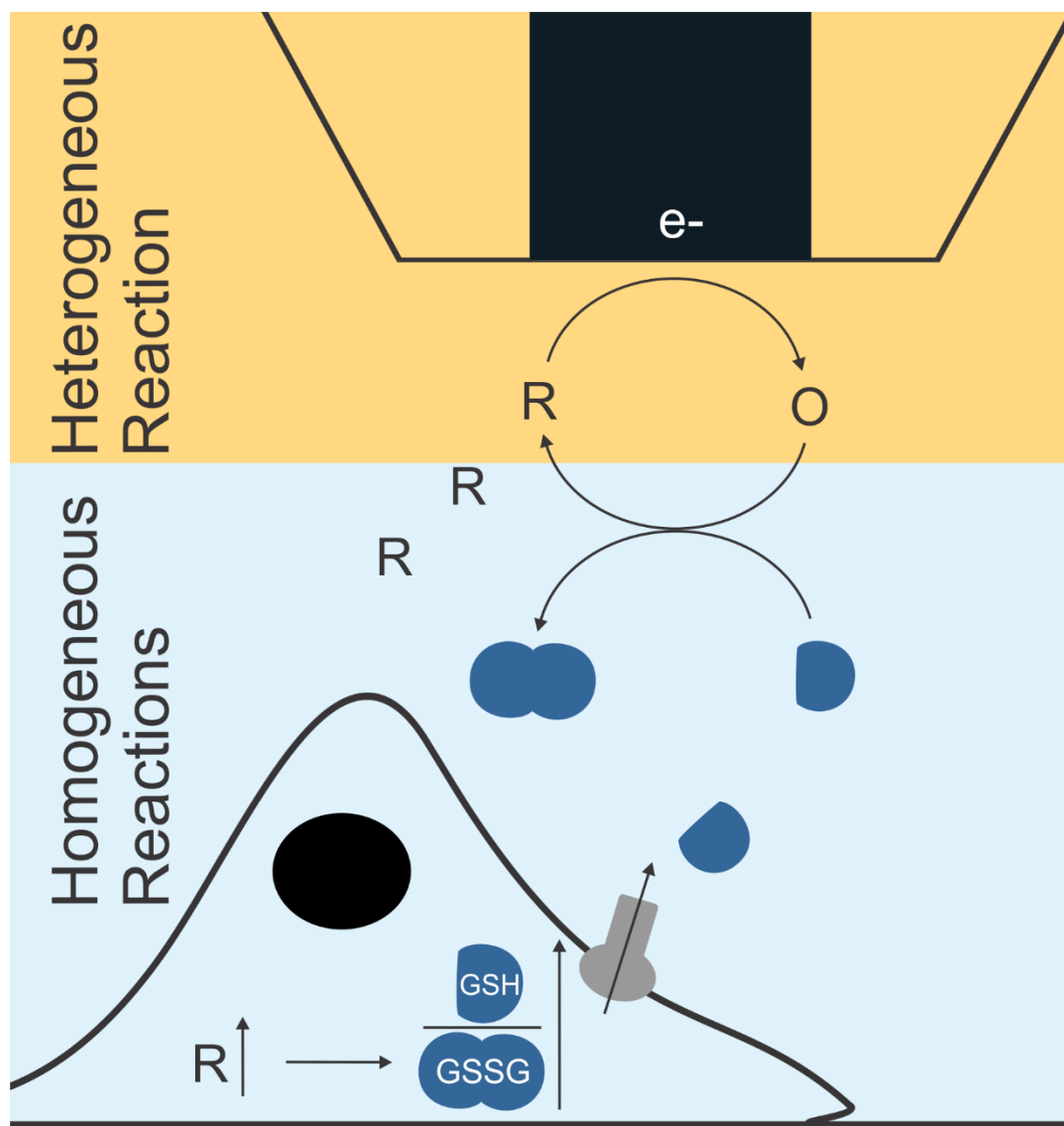


Figure 1.12. Schematic representation of homogeneous and heterogeneous reactions occurring during live cell SECM analysis.

1.6 Dissertation Outline

This dissertation focuses on the non-invasive *in-vitro* monitoring of the redox environment in living cells. Furthermore, attention is paid to the cell's instantaneous response to the exposure to stress inducing molecules, measured on the single cell level. For this purpose, human adenocarcinoma cervical cancer cells (HeLa) and a multidrug resistant variant (HeLa-R) were employed as model organisms and were imaged in constant height SECM feedback mode. The dissertation is structured into six chapters that are presented in the form of manuscripts.

Following this introduction, **Chapter II** presents the preliminary and first approach for the quantification of the GSH efflux from living cells by SECM based on the use of a cell impermeable and a cell permeable redox mediator, whereby the increased cell metabolism of HeLa-R compared to HeLa cells. Furthermore, the development of a cell patterning strategy for target cells was established. Cells of interest need to be patterned in an efficient and environmentally friendly way, facilitating their locating and imaging by SECM. Such a patterning strategy not only restricts the cell's ability to alter their position during measurements, but also allows us to study cells of different types in co-culture (HeLa and HeLa-R) at the same time and under the exact same conditions. The usefulness of the generated cell patterns is demonstrated as well as a method to decouple the electrochemical current into separate profiles for topography and electrochemical reactivity signal is proposed.

The knowledge obtained in chapter II offers an alternative to constant distance mode in SECM. In **Chapter III**, the appearance of a forced convection effect during SECM imaging is presented when scanning at high velocities. This effect is confirmed by numerical simulations and studied experimentally and theoretically over different features. A quasi-linear dependence of the normalized peak current on the scanning velocity during SECM imaging is revealed, suggesting

the extrapolation of the true feedback signal without contribution of convection even in constant height measurements.

Chapter IV presents the extraction of a living cell's extracellular FcCH₂OH regeneration kinetics from the peak current behaviour, shown in chapter III. The introduction of a forced convection effect can be used to determine the heterogeneous rate constant at slow and fast SECM scan velocities by numerical modeling. The extraction of a single cell's kinetic rate, independent from sample topography, is proposed. This approach is tested over three different model substrates and applied to the two cell lines HeLa and HeLa-R.

While the first chapters are concerned with the establishment of methodologies to determine a living cell's heterogeneous rate constant, **Chapter V** displays the application of the proposed method and theory to human cancer cells to monitor a cell's electrochemical response to stress by SECM. The effect of green tea catechins on HeLa cells is presented, where the catechins function as stress causing agent due to their known antioxidant properties. In fact, an alteration of cellular metabolic rate was found following exposure to green tea catechins.

Finally, **Chapter VI** summarizes and concludes all findings presented in this dissertation. A comparison is made between the presented methods to quantify the cellular GSH efflux and hence, the heterogeneous kinetics of the involved reactions. Furthermore, the impact of our findings is discussed in the context of literature about quantitative cell studies using the technique of SECM. Suggestions are made for future improvement strategies and possible studies.

CHAPTER II

ASSESSMENT OF MULTIDRUG RESISTANCE ON CELL COCULTURE PATTERNS USING SCANNING ELECTROCHEMICAL MICROSCOPY

To understand the behaviour of cancer cells and their response to external stimuli, it is important to optimize the analytical method of choice. During Scanning Electrochemical Microscopy imaging, especially with living samples, such as human cancer cells, experimental conditions must be controlled, evaluated and adjusted accordingly. In order to assure reproducible and representative data acquisition, target cells had to be positioned on the surface in a defined manner, allowing easy recognition and approach of a microelectrode towards the cell of interest. In order to compare the electrochemical signal of different model cell lines, cell co-cultures needed to be established, avoiding cross contamination. The present chapter demonstrates the initial approach to extract kinetic information from experimental SECM data by using redox mediators (cell permeable and cell non-permeable) in SECM imaging. Topographical information were successfully decoupled from an electrochemical signal related to cancer cell activity.

This dissertation chapter has been published in 2013 in the journal Proceedings of the National Academy of Science of the United States of America, Volume 110, Issue 23, Pages 9249 to 9254 (www.pnas.org/cgi/doi/10.1073/pnas.1214809110). Sabine Kuss, David Polcari, Matthias

Geissler, Daniel Brassard and Janine Mauzeroll are co-authors of this article. The Supporting Information for this publication can be found in Appendix A. As stated by the journal in its rights and permission policy, PNAS authors do not need to obtain permission to include their papers as part of their dissertations.

As explained in detail on pages 25-28, the contribution to this work by all co-authors involved:

- Sabine Kuss: Design of experiments, performing experiments, data analysis and treatment, discussion, preparation of figures and manuscript.
- David Polcari: Data analysis and treatment, preparation of figure 2.2A and 2.4 and manuscript
- Matthias Geissler: Preparation of membrane materials, preparation of manuscript
- Daniel Brassard: Preparation of membrane materials
- Janine Mauzeroll: Supervision, preparation of manuscript

2.1 Abstract

The emergence of resistance to multiple unrelated chemotherapeutic drugs impedes the treatment of several cancers. Although the involvement of ATP-binding cassette transporters has long been known, there is no in situ method capable of tracking this transporter-related resistance at the single-cell level without interfering with the cell's environment or metabolism. Here, we demonstrate that scanning electrochemical microscopy (SECM) can quantitatively and noninvasively track multidrug resistance-related protein 1-dependent multidrug resistance in patterned adenocarcinoma cervical cancer cells. Nonresistant human cancer cells and their multidrug resistant variants are arranged in a side-by-side format using a stencil-based patterning scheme, allowing for precise positioning of target cells underneath the SECM sensor. SECM measurements of the patterned cells, performed with ferrocenemethanol and $[\text{Ru}(\text{NH}_3)_6]^{3+}$ serving as electrochemical indicators, are used to establish a kinetic “map” of constant-height SECM scans, free of topography contributions. The concept underlying the work described herein may help evaluate the effectiveness of treatment administration strategies targeting reduced drug efflux.

2.2 Introduction

Cancer cells, such as lung cancer or leukemia, acquire resistance to multiple unrelated drugs in response to treatment with chemotherapeutic agents^{71,75}. Resistance impedes therapeutic effectiveness, which in turn, reduces the long-term survival rate of cancer patients⁷⁵. The emergence of multidrug resistance (MDR) involves the overexpression of transmembrane proteins P-glycoprotein (P-gp) and MDR-related protein 1 (MRP1), which both belong to the family of 5'-triphosphatebinding cassette transporters (known as ABC transporters). P-gp and MRP1 act as molecular “pumps,” actively removing therapeutic agents from the cancer cells, thereby preventing

the drug from inducing the desired effect on the cell nucleus or cytoplasm. MDR based on P-gp is relatively well understood and involves binding of hyaluronan to the cell surface glycoprotein CD44. The resulting up-regulation of the transcriptional cofactor p300 expression and therefore the NFkappaB-specific transcriptional up-regulation lead to the production of P-gp, and with that chemoresistance in cells ⁸⁵. However, the mechanism that causes MRP1-mediated MDR remains unclear. Currently, quantification of MDR relies on immunohistochemical analyses, such as real-time PCR, focusing mostly on P-gp or other members of ABC transporters ⁸⁸⁻⁹³. Fluorescent MRP1-specific studies were also conducted, revealing that resistant and nonresistant cancer cells have differential intracellular content of glutathione and GST, which affect their cell death mechanism during hyperthermia ⁹⁴. Microvoltammetry was also used to measure the efflux of chemotherapeutic drugs from normal and MDR cancer cells on the single-cell level, with detection limits in the nanomolar range ⁹⁵. Finally, flow cytometry has routinely been used to quantify and compare expression levels and activity of different ABC transporters that are linked to MDR ⁹⁶⁻⁹⁸. Although the transporter activity can be inferred from the drug retention in the cell, this method has been advanced by using the invariable drug retention on polymer beads as a standard in flow cytometry measurements ⁹⁹. Herein, we report the use of cell coculture patterns for quantitative analysis of MDR in adenocarcinoma cervical cancer cells on the single-cell level using scanning electrochemical microscopy (SECM). In contrast with flow cytometric quantification of MDR, SECM allows for in situ observation on the single-cell level without interfering with the cell's environment or metabolism. In SECM, a microelectrode is scanned across a surface while the electrochemical current is recorded with high spatial and temporal resolution ¹⁰⁰. Since the first studies on single human cells emerged in 1998 ¹⁰¹, SECM has gained increasing attention as an analytical tool for biological studies ¹⁰²⁻¹⁰⁵. After successfully confirming cell viability and

oxidative stress in living cells ^{106–108}, the focus of analytical studies shifted toward the investigation of MDR. For example, the MRP1-mediated efflux of the menadione S-glutathione conjugate (thiodione) was monitored in yeast and hepatoblastoma cells, making it possible to estimate the export rate of thiodione by SECM ^{108,109}. Most recently, Bard et al. monitored the formation of thiodione from menadione in adenocarcinoma cervical cancer cells (HeLa). In this study, the detection of thiodione by SECM not only allowed for the quantification of MRP1-mediated efflux of thiodione, but with the use of MK571 as an MRP1 blocker, the MRP1 efflux pump was identified as a major carrier for thiodione in living HeLa cells ¹¹⁰. The work presented in this study uses genetic modification of HeLa cells to compare a wild-type culture with MRP1 overexpressing cells (HeLa-R). The redox mediator ferrocenemethanol (FcCH₂OH) is used to quantify MRP1 activity of these two cell lines through its unique interaction with glutathione, a peptide molecule involved in MRP1-related transport. Tracking the evolution of MRP1 activity and expression is important because direct clinical implications make MRP1 a relatively unique molecular marker in comparison with other prognostic variables identified for several cancer types ^{74,76}.

2.3 Material and Methods

2.3.1 Formation of Cell Culture Patterns

For HeLa cell patterning, the Zeonor substrate was first exposed to oxygen plasma and then brought in contact with an untreated elastomeric membrane containing open through-holes (see SI Text for further details). The cell culture substrate was placed in a 30 mm Petri dish and fixed using biocompatible high-vacuum grease (Dow Corning). Next, 2.5 mL of DMEM+ was added, followed by removal of air bubbles under reduced pressure for 15 min. A suspension of 5×10^5 cells along with 4 mL of DMEM+ was added to the Petri dish, and the sample was incubated at 37

°C in a 5 % (vol/vol) CO₂ atmosphere for 5–24 h. Upon completion of the seeding process, the membrane was peeled off the surface. For HeLa-R cell patterning, the membrane was placed on the Zeonor substrate before treatment with oxygen plasma. The membrane was removed and the Zeonor substrate was placed in a 30 mm Petri dish, followed by addition of a suspension containing 3.5×10^5 cells along with 4 mL of DMEM+. The sample was incubated at 37 °C in a 5 % (vol/vol) CO₂ atmosphere for 5–24 h. To obtain coculture patterns, both Zeonor substrate and membrane were exposed to oxygen plasma. The membrane was then removed and the substrate was placed in a 30 mm Petri dish and fixed using biocompatible high-vacuum grease. A section (~50 %) of the central array comprising 50 µm OPS was covered using a planar PDMS slab. A cell suspension of 5×10^5 green-stained HeLa-R cells was added and completed to 4 mL with DMEM+. The sample was incubated at 37 °C in a 5 % (vol/vol) CO₂ atmosphere for 12 h, followed by washing with DMEM-. Upon removal of the PDMS slab, a suspension of 7×10^5 red-stained HeLa cells was added and completed to 4 mL with DMEM+ if necessary. The sample was incubated at 37 °C in a 5 % (vol/vol) CO₂ atmosphere for 14–18 h.

2.3.2 Electrochemical Measurements

Electrochemical imaging was performed in constant-height mode (12 µm above sample normal) at a scan rate of $15 \mu\text{m}\cdot\text{s}^{-1}$ using an Electrochemical Probe Scanner 3 SECM instrument manufactured by HEKA Elektronik Dr. Schulze GmbH⁶¹. Pt microelectrodes (25 µm in diameter) were fabricated and assembled as described previously⁸⁷. Oxidation of FcCH₂OH (1 mM dissolved in DMEM-) was recorded at a potential of 0.5 V vs. Ag/AgCl for which a steady-state current was determined using cyclic voltammetry. An electrochemical approach curve was recorded at a speed of $2 \mu\text{m}\cdot\text{s}^{-1}$. Before electrochemical measurements, HeLa and HeLa-R cells were exposed to 1 mM FcCH₂OH in DMEM- solution for 75 min. Electrochemical imaging of

[Ru(NH₃)₆]³⁺ (1 mM dissolved in DMEM-) reduction was performed at a potential of -0.35 V vs. Ag/AgCl. SECM data were analyzed using Matlab R2012b (MathWorks).

2.4 Results and Discussion

2.4.1 Patterning of Cell Islands

Comparative SECM measurements on the single-cell level benefit from culture substrates that allow for arrangement of cells in a regular format. A consistent template providing alignment and registration between cells (as opposed to a random distribution) makes it possible to perform measurements multiple times and achieve a high level of reliability. In addition, it facilitates the positioning of cells underneath the microelectrode, thereby reducing preparation and analysis time. Because growth of cells largely depends on the properties of the surface on which they grow, template formation generally requires a patterning step to be performed with the substrate. One approach involves activation of selected regions on a nonresponsive surface. A number of modification schemes involving self-assembled monolayers^{111,112}, polymer films¹¹³, and proteins¹¹⁴ have been shown to direct cell attachment on a variety of natural and artificial substrates. Another approach relies on masking selected sites on an active surface to prevent adhesion of cells in these regions. The use of microfluidic systems^{115,116} and stencil masks^{117,118} are examples of this approach. Both methodologies take advantage of topographic features that provide a physical barrier in the patterning process. Even though many techniques are readily applicable to the patterning of a single cell line, they often fail to be effective when two (or more) cell lines are to be considered for array formation, especially at reduced scale.

Herein, we describe a stencil-based patterning approach that constitutes a practical solution to this end. We use an open through-hole membrane fabricated from an elastomeric

blockcopolymer (e.g., Versaflex CL30, GLS Corp.)¹¹⁹ (see SI Text for details) in combination with oxygen plasma treatment to achieve live cell patterns on an insulating plastic substrate (e.g., Zeonor 1060R, Zeon Chemicals). Versaflex CL30 is a meltprocessable styrenic ethylene/butylene block-copolymer^{120,121}, which has recently been shown to promote the fabrication of thin-film membranes with small-scale openings in a single step using hot embossing lithography (HEL)¹¹⁹. In principle, open through-hole membranes can be produced from other elastomers such as poly(dimethylsiloxane) (PDMS), which to this end constitutes the prime material for soft microfabrication and patterning^{117,118}. However, the method described herein provides several advantages with respect to fabrication and handling of the membranes¹¹⁹. For example, Versaflex CL30 provides off-the-shelf availability as it can be stored (e.g., as an extruded sheet) over extended periods of time, whereas PDMS as a thermoset polymer necessitates timely preparation. Thin, open through-hole membranes obtained with standard PDMS formulations (e.g., Sylgard 184) are relatively fragile, which makes their handling nontrivial and limits the scope of possible applications. Versaflex CL30, on the other hand, provides superior mechanical stability as reflected by 780% elongation at break (whereas PDMS generally does not exceed 140%), diminishing the risk of damage during removal from the mold and providing the possibility of reducing vertical and lateral dimensions of the replicated features. Spin-casting of PDMS further contributes to irregularities in thickness of the membrane¹²², whereas those fabricated from Versaflex CL30 using HEL are smooth and uniform in thickness, with the embossed open through-holes showing excellent lithographic definition. We produced membranes with openings ranging from 50 to 500 μm , as shown in Fig. 1.1A and B. Openings are used to form oxygen plasma-treated spots (OPS) on Zeonor serving as a solid cell culture substrate. Previous work has shown that hydrophilic, oxygen-containing groups promote cell attachment on a Zeonor surface¹¹⁵.

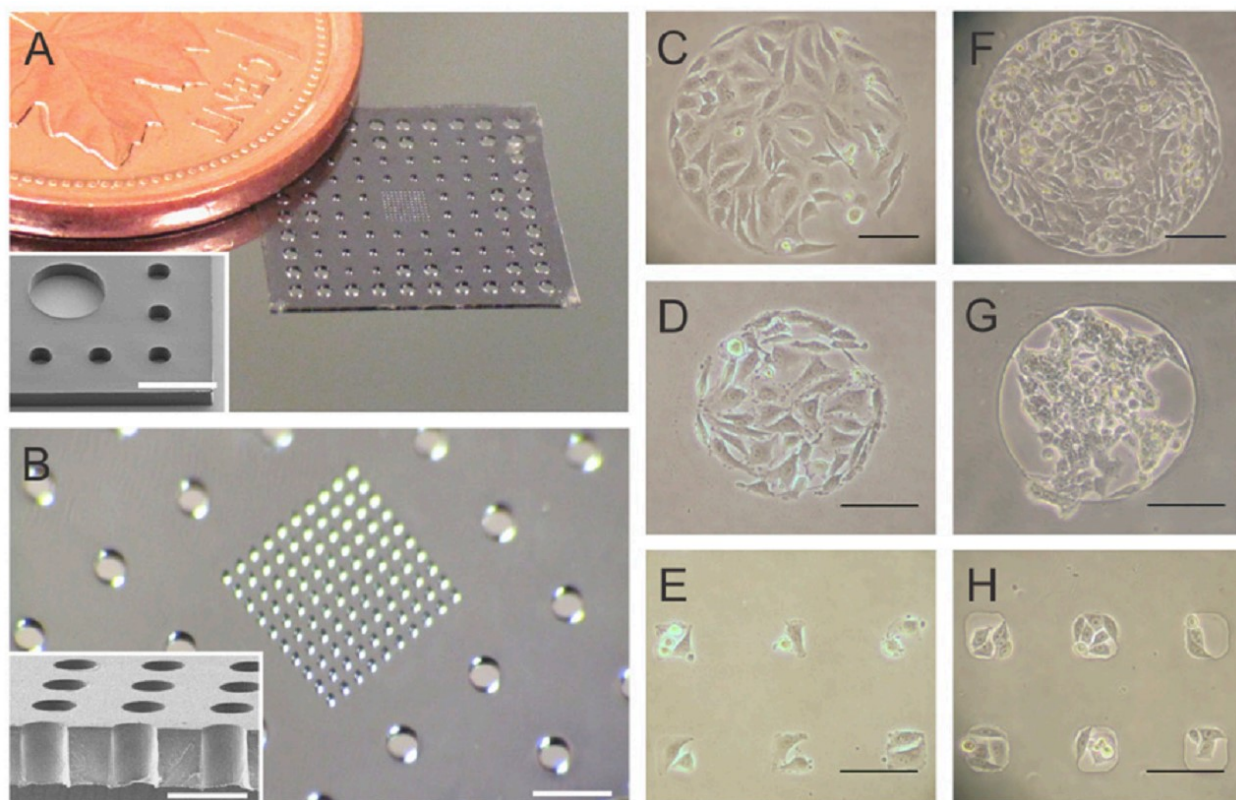


Figure 2.1 Layout of the elastomeric stencil and resulting cell patterns. (A) Photograph of an open through-hole membrane as used within this study. (Inset) Scanning electron micrograph of a corner section. (Scale bar: 500 μm .) (B) Close-up view of the central part of the membrane. The array contains 100 openings of 50 μm in diameter arranged in a 10 \times 10 configuration. (Scale bar: 500 μm .) (Inset) Scanning electron micrograph depicts a cross-sectional view of the array after the membrane had been cut in half using a blade. (Scale bar: 100 μm .) (C–H) Optical micrographs of cell islands formed from HeLa (C–E) and HeLa-R cells (F–H). OPS were generated using circular through-holes of 400 and 200 μm in diameter as well as rectangular features of 50 μm in width and length, respectively. (Scale bar: 100 μm .)

Each membrane made it possible to achieve cell islands with different dimensions, as shown for both HeLa (Fig. 1.1C–E) and HeLaR cells (Fig. 1.1F–H). However, the details of the patterning process must be adjusted for each cell line according to morphology and characteristics of growth.

For example, HeLa cells are more efficiently patterned on OPS provided by an untreated membrane that is placed on the Zeonor slide following exposure to oxygen plasma. Due to their tendency to grow in colonies, HeLa-R cells are preferably seeded on a Zeonor substrate from which the membrane was removed upon oxygen plasma treatment. Regardless of the option used, formation of OPS benefits from the ability of the elastomeric membrane to achieve intimate, yet reversible contact with the substrate ¹¹⁹. OPS ranging from 200 to 400 μm in diameter enable cell growth in defined, well-populated islands, whereas 50 μm OPS (either circular or rectangular) result in groups with a limited number (e.g., 2–9 cells) for both HeLa and HeLa-R cell lines. The defined physical separation of cells provides control over several experimental parameters, such as location of target cells, cell movement during acquisition, and analysis time (which can be extended to at least 8 h). Studies on cell communication or cell signaling, observation of cell death, and examination of the cell response to drugs or other medical treatments will benefit from this patterning procedure.

2.4.2 SECM Imaging

We performed SECM measurements on patterned HeLa cells using a Pt microelectrode biased at a potential where the dissolved redox mediator FcCH_2OH is oxidized to $[\text{FcCH}_2\text{OH}]^+$ (Scheme S1) under mass-transfer control. Fig. 1.2A represents a redox reactant competition mode to illustrate electrochemical reactions during SECM measurements. In this scheme, the reactant FcCH_2OH is “consumed” by the cell through passive diffusion, whereas the microelectrode “consumes” FcCH_2OH to produce the $[\text{FcCH}_2\text{OH}]^+$ that will be regenerated by the cell. The faradaic microelectrode current monitored during SECM imaging inherently contains contributions from both topography and electrochemical activity of the underlying surface.

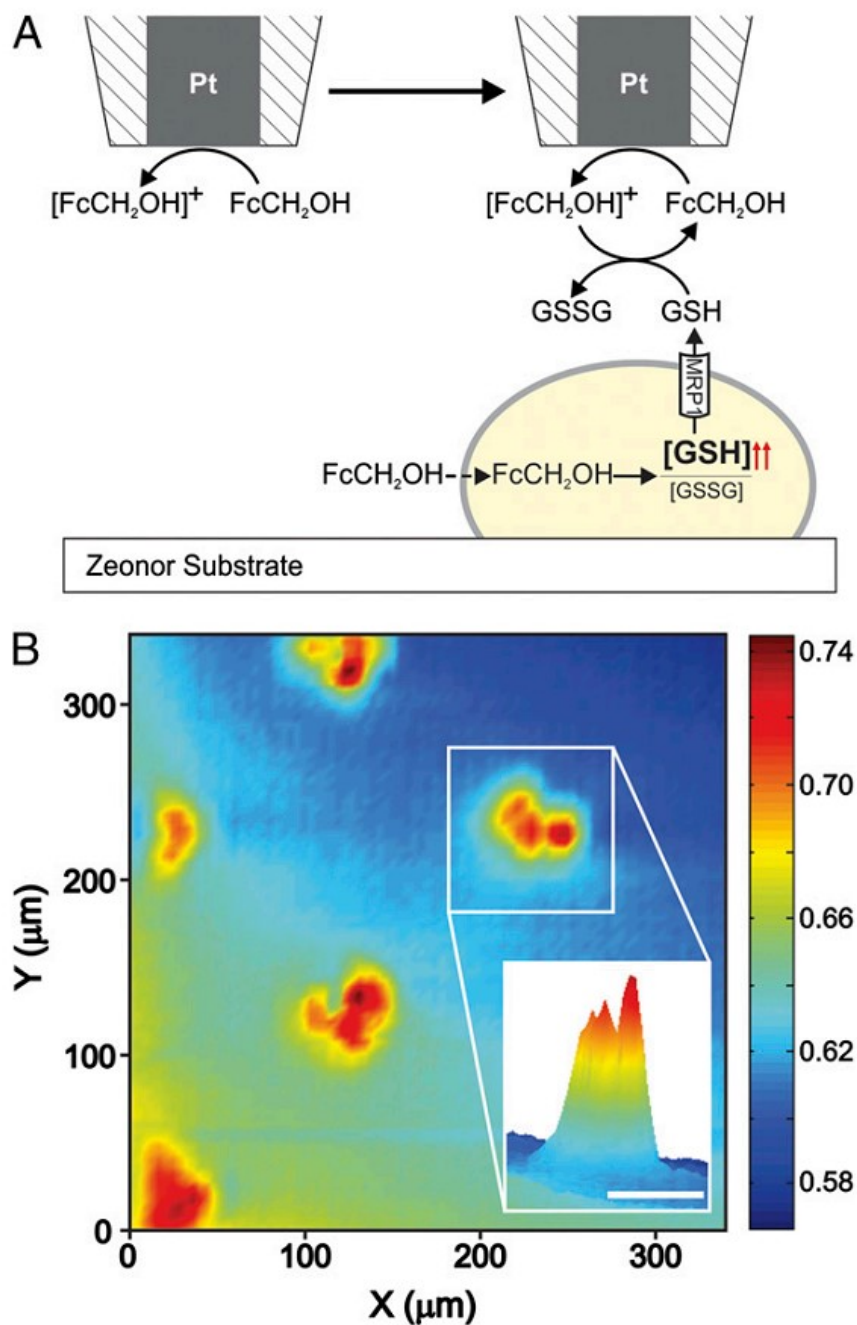


Figure 2.2 Cell imaging using SECM. (A) Schematic illustration of constant-height feedback mode SECM imaging with a living cell in the presence of FcCH_2OH as a redox mediator. FcCH_2OH is oxidized to $[\text{FcCH}_2\text{OH}]^+$ at the Pt microelectrode, and regenerated in proximity to the cell as a result of GSH efflux. (B) Normalized SECM current recorded at a distance of 12 μm above the substrate when HeLa cells were exposed to FcCH_2OH (1 mM) for 75 min. (Inset) Close-up 3D view of the signal obtained from an individual cell island. (Scale bar: 50 μm .)

Because the substrate itself does not show any electrochemical activity, the microelectrode current progressively decreases with decreasing tip-to-substrate distance as a result of the hindered diffusion of the redox mediator. Using this negative feedback signal, the microelectrode is first prepositioned over a bare region of the substrate at a tip-to-substrate distance greater than the maximum cell height (e.g., 12 μm). The biased microelectrode is then scanned at this constant height across a defined area of patterned cells. As the microelectrode scans over the patterned cells, the measured current monitors the gradient in concentration of FcCH_2OH , which is concomitantly affected by the topography of the cell, the cell's permeability to FcCH_2OH , and the glutathione-dependent regeneration of FcCH_2OH (Fig. 1.2A). Overall, the contributions from negative feedback and passive FcCH_2OH diffusion into cells are outweighed by the enhanced mass transport contribution of the regeneration reaction of FcCH_2OH (Fig. 1.2B). The SECM image in Fig. 1.2B shows a distinct, well-separated signal for each cell island, which correlates with the original layout of 50 μm features with a spacing of 100 μm in between. The color bar presents the dimensionless microelectrode current Ni_T described as

$$Ni_T = \frac{i_T}{i_{T\infty}} \quad (2.1)$$

where i_T is the measured microelectrode current and $i_{T\infty}$ is the measured microelectrode current in bulk solution. Regions of increased Ni_T over the patterned cells in Fig. 1.2B result from the action of FcCH_2OH , which is cell-permeable and alters intracellular glutathione disulfide levels, thereby producing an excess of glutathione (GSH) that is expelled from the cell by MRP1. GSH serves as an antioxidant (Scheme S2) in mammalian cells, and can be used as an indicator for a cell's redox state. Furthermore, its concentration is dependent on MDR⁹⁴. The active efflux of GSH from the cell participates in the $\text{FcCH}_2\text{OH}/[\text{FcCH}_2\text{OH}]^+$ redox cycle by reducing $[\text{FcCH}_2\text{OH}]^+$ back to

FcCH₂OH⁸⁷. As a result, the flux of FcCH₂OH to the electrode surface increases, leading to a higher electrochemical signal.

2.4.3 Formation of Cell Coculture Pattern

Uniformity of the pattern geometry and chemistry is critical in coculture formation because both parameters can alter the natural morphology and metabolism of the studied cells¹²³. Within the context of SECM measurements, the dimensions of cocultured patterns should comply with the scan range provided by the instrument to enable simultaneous analysis under identical conditions, which has proven difficult in the past^{123–127}. We responded to this challenge by partly shielding the template with a thin cover slab of PDMS to produce cocultures of HeLa and HeLa-R cells in a side-by-side format (Fig. 1.3). During incubation with a first cell line (e.g., HeLa-R), only non-covered OPS are occupied, whereas the PDMS prevents access of the cells to the surface underneath. Once completed, the cell suspension is removed from the substrate, followed by washing and peeling off the PDMS slab. Subsequent incubation with a second cell line (e.g., HeLa) favors adhesion to OPS previously covered by the PDMS slab. The process can also be performed in an alternative fashion by using an open through-hole membrane for incubation, and covering designated sections with PDMS. In principle, this variant would limit the risk of contaminating OPS because PDMS contains low molecular-weight residues that can be transferred upon contact¹²⁸. Dividing an array of 50 μm OPS using a PDMS slab requires alignment, yet the spacing between features was maintained sufficiently large (e.g., 100 μm) to facilitate manual manipulation using a standard microscope setting. A HeLa-R cell pattern with the PDMS slab still in place is included in Fig. 1.3, demonstrating the ability of the PDMS slab to effectively protect the OPS underneath during the first incubation step. To facilitate discrimination of individual cells in each

segment, we performed patterned coculture using HeLa and HeLa-R cells stained with red and green fluorescent dyes, respectively (see SI Text for details). Inspection of the patterned sample revealed that it is possible to produce high quality arrays in which both cell lines remain perfectly separated from each other as shown by the example in Fig. 1.3. Patterns obtained with 50 μm OPS usually contain 2.8 ± 1.5 HeLa cells and 5.2 ± 2.1 HeLa-R cells. Despite the fact that the number of cells is prone to variation, patterns produced in this way are well suited for quantitative SECM investigation.

2.4.4 SECM Imaging of Cocultures and Data Analysis

We imaged cell cocultures in two different electrochemical solutions to effectively decouple the cell height variability across patterns and quantitatively compare the electrochemical signals produced by each cell line, using the pattern in Fig. 1.4A. The sample comprises HeLa-R (Fig. 1.4A, Left) and HeLa cells (Fig. 1.4A, Right) free of cross-contamination, as confirmed by the fluorescence image in Fig. 1.4B. To decouple topography from electrochemical activity, the coculture was first imaged in a solution of $[\text{Ru}(\text{NH}_3)_6]^{3+}$ (Fig. 1.4C), serving as a control, and then in FcCH_2OH solution (Fig. 1.4D) under the same experimental conditions. As a highly charged cation, $[\text{Ru}(\text{NH}_3)_6]^{3+}$ is a cell-impermeable redox mediator that allows for recording a pure negative feedback response (Fig. 1.4C), which is analogous to surface topography. As the microelectrode is scanned above the patterned cells, the diffusion of $[\text{Ru}(\text{NH}_3)_6]^{3+}$ to the microelectrode surface is hindered by the physical presence of the cells. Increased cell heights lead to more pronounced decrease in Ni_T . Using pure negative feedback theory and the experimental response of $[\text{Ru}(\text{NH}_3)_6]^{3+}$, it was possible to transform the SECM current image (Fig. 1.4C) into a topography image (Fig. 1.4E), where the color bar represents the tip-to-substrate distances

(micrometers). Wittstock et al. have demonstrated a similar transformation procedure ¹²⁹. In our study, the dimensional distances were calculated from the normalized tip-to-substrate distances L , which were extracted from the experimental data using the Nelder–Mead simplex algorithm ¹³⁰ and the analytical approximation for negative feedback current ¹³¹ where Ni_T^{ins} is the normalized current over an insulator, L is the normalized distance defined as the ratio of the tip-to-substrate distance and the radius of the metal wire of the electrode, and RG is the ratio of the microelectrode outer radius and metal wire radius. The L values used to calculate the tip-to-substrate distances in Fig. 1.4E were extracted for a microelectrode with $RG=5.5$, which is within the validity limits of Eq.2 ($RG<200$ and all L values). Also, the value of the normalized distance of the first point in the scan (upper left-hand side corner) was 0.92, which corroborates the value extracted from the prepositioning approach curve (0.96). Finally, the slopes in x and y at the edges of the images remained unaltered following the transformation from Fig. 1.4C to E. Although PBS is known to alter cell's morphology and hence its metabolism over time ⁸⁷, studies on human gastric carcinoma cells have shown a change in cell height of just 55–365 nm when exposed to PBS for a period of 2 h¹³². Even when cells were exposed to hypotonic or hypertonic solutions, a height variation of 0.75–2.00 μm was observed ¹³³. Given an electrode diameter of 25 μm and a significantly more sustaining environment during our studies in cell medium, any possible effect of alteration in cell height lies within the measurement error.

$$Ni_T^{ins} = \frac{\left(\frac{2.08}{RG^{0.358}}\right)\left(\frac{0.145}{RG}\right) + 1.585}{\left(\frac{2.08}{RG^{0.358}}\right)(L + 0.0023RG) + 1.57 + \frac{\ln(RG)}{L} + \left(\frac{2}{\pi RG}\right)\ln\left(1 + \frac{\pi RG}{2L}\right)} \quad (2.2)$$

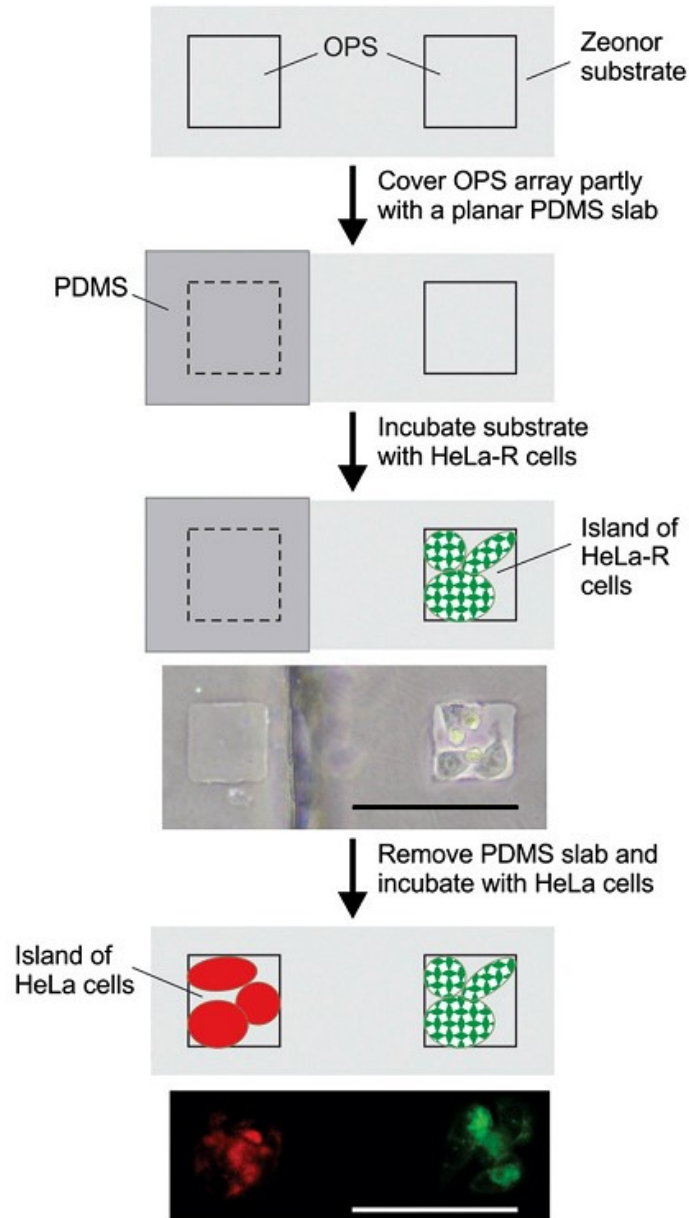


Figure 2.3 Formation of cell coculture patterns in a side-by-side configuration. Patterning scheme involves a template partly covered by a PDMS slab to promote selective adhesion and growth of a first cell line (HeLa-R) on the substrate. The optical microscope image depicts an OPS occupied by three HeLa-R cells whereas the adjacent one remains covered by the PDMS slab. Once the slab is removed, the sample is exposed to a second cell line during which cells adhere on OPS that were inaccessible during the first incubation step. The fluorescence micrograph shows stained HeLa cells (red) and HeLa-R cells (green) in the form of a side-by-side coculture pattern. (Scale bar: 100 μm .)

Following this first SECM scan, the $[\text{Ru}(\text{NH}_3)_6]^{3+}$ solution is removed and replaced by FcCH₂OH solution to acquire a second SECM scan (Fig. 1.4D) using the same experimental conditions. Given the presence of a regeneration reaction, the total normalized microelectrode current Ni_{Tot} , which contains contributions from both cell topography and electrochemical activity, is described by ^{134,135}

$$Ni_{\text{Tot}} = Ni_s \left(1 - \frac{Ni_T^{\text{ins}}}{Ni_T^{\text{cond}}} \right) + Ni_T^{\text{ins}} \quad (2.3)$$

where Ni_s is the kinetically controlled substrate current, Ni_T^{cond} is the normalized current over a conductor, and Ni_T^{ins} is the normalized current over an insulator (see SI Text for further details). The behavior of homogeneous reactions toward SECM is not yet described. We assume the reactions to take place mainly in close proximity to the cell surface. Using Eq.2.3, the extracted normalized distances (from Fig. 1.4E), and the Nelder–Mead simplex algorithm, the SECM current image acquired in FcCH₂OH solution (Fig. 1.4D) is converted into a kinetic map (Fig. 1.4F), where the color bar quantifies the apparent heterogeneous rate constant (k_f). The extracted values for k_f fall within the validity ranges of Eq.2.3, for which $0.1 \leq L \leq 1.5$ and $0.01 \leq \Lambda \leq 1,000$ ¹³⁴. For the bare Zeonor substrate, k_f is on the order of $10^{-7} \text{ cm}\cdot\text{s}^{-1}$, which is indistinguishable from pure negative feedback behavior. The slope in x and y at the edges of the image on the non-patterned plastic surface was also insignificant, which demonstrates that the decoupling procedure successfully removed the topographical component from the total current and allowed for the extraction of the kinetic contribution. In comparing the kinetic constants extracted for both patterned cell areas, a clear differential response is observed between normal HeLa cells and their MDR variant. The overall distribution of k_f values over HeLa cells is significantly lower than over their MDR counterparts. Furthermore, the maximum k_f value observed over HeLa-R cells was 2.4

times greater than over HeLa cells (e.g., $k_f=3.18\times 10^{-6}\text{ cm}\cdot\text{s}^{-1}$ vs. $1.35\times 10^{-6}\text{ cm}\cdot\text{s}^{-1}$, respectively). From Fig. 1.4F, we conclude that the MRP1 phenotype of human cancer cells can be monitored using a nontoxic, electrochemical indicator that causes minimal alterations to the metabolism of the cell.

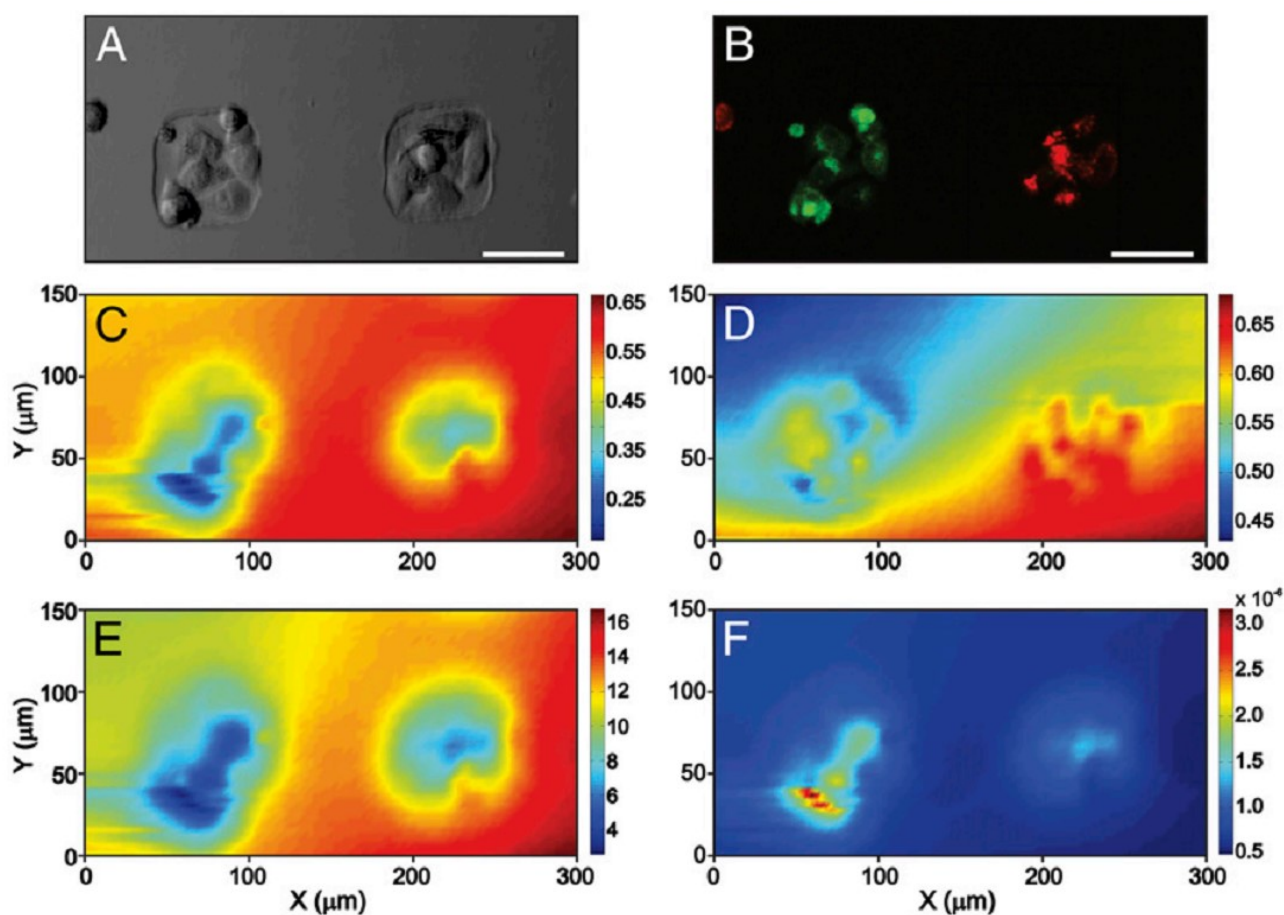


Figure 2.4 SECM imaging and decoupling of feedback response for a HeLa and HeLa-R cell coculture substrate. (A) Optical micrograph of a coculture pattern containing seven HeLa-R cells (Left) and six HeLa cells (Right). (B) Fluorescence micrograph of the sample shown in A, with HeLa-R cells stained green and HeLa cells stained red. (C and D) Normalized SECM currents recorded with the same sample at 12 μm above the substrate in 1 mM $[\text{Ru}(\text{NH}_3)_6]^{3+}$ (C) and 1 mM FcCH_2OH (D). (E) Extracted normalized tip-to-substrate distance profile. (F) Profile of the extracted apparent heterogeneous rate constant ($\text{cm}\cdot\text{s}^{-1}$) for the sample shown in A. (Scale bar: 50 μm .)

2.5 Conclusions

The SECM measurements presented in this study suggest that it is possible to decouple microelectrode current into two separate profiles for topography and electrochemical activity. The extracellular regeneration of FcCH_2OH was detected and imaged in real time by an SECM microelectrode positioned 12 μm above cell patterns. Comparison of electrochemical signal intensities revealed that a differential response is obtained between HeLa and HeLa-R cells, the latter showing increased activity. The ability to produce cocultures of both HeLa and HeLa-R cells in a spatially controlled manner was essential in this context. The stencil-based patterning method differs from preceding work insofar as it employs a cover slab to control the configuration of the cell culture template, making it accessible for cells on demand in subsequent incubation steps. The relative proximity and regular arrangement of cell islands shortens registration and analysis time. Moreover, this configuration enables multiple experiments to be performed under the exact same microenvironmental conditions, promoting the acquisition of electrochemical data with a high statistical significance. It is possible that this quantitative methodology can be generalized and extended to several adhesive cell lines, given the anticipated versatility of the patterning strategy presented herein. Ideally, we envision a series of co-cultured cells having an increasing MRP1 phenotype as obtained through doxorubicin drug challenges¹³⁶. The action of selective or competitive MRP1 inhibitors could then be monitored under normal and stressed conditions. Also, the evolution of MDR in cells having an initial low MDR phenotype could be monitored with increasing chemotherapeutic exposure time. In the future, SECM-based methods could indicate the risk of resistance using cells harvested from biopsies. They could be also used for rapid screening of different MDR inhibitors and classify the resistance signature of several cancer cells so that a patient can receive the most appropriate and personalized treatment.

2.6 Acknowledgments

We thank Dr. Philippe Gros (McGill University) for providing the MRP1-overexpressing variant of the HeLa cells, as well as Denis Flipo, Université du Québec à Montréal (UQÀM), Christian Kuss (UQÀM), Caroline Miville-Godin, National Research Council (NRC), and Dr. Teodor Veres (NRC) for technical assistance and useful discussion. This work was supported in part by the Natural Sciences and Engineering Research Council of Canada and the Canadian Foundation for Innovation.

CHAPTER III

FORCED CONVECTION DURING SCANNING ELECTROCHEMICAL MICROSCOPY IMAGING OVER LIVING CELLS: EFFECT OF TOPOGRAPHIES AND KINETICS ON THE MICROELECTRODE CURRENT

The previous chapter presents an alternative to the constant distance mode available for SECM measurements. Although constant distance offers advantages, such as the immediate separation of topographical and electrochemical signals, it requires highly complicated and expensive instrumentation, which not widely accessible. To use the constant height mode of SECM to study cells, draw backs, such as long imaging times must be improved. Living cells require an adequate temperature and culture medium to maintain a stable metabolism. Long measurements (e.g. 2 hours), as presented in chapter 2, may lead to unwanted alterations in the cell's electrochemical response, as normal culture conditions cannot be guaranteed during acquisition time. Increasing the scan velocity of the microelectrode is one option to shorten measurement time without compromising scan resolution, however a potential influence of convection on the tip current, introduced by the moving tip needs to be assessed. The following chapter investigated the behaviour of forced convection effects on three model substrates.

This chapter has been published in 2013 in the journal *Electrochimica Acta*, Volume 110, Pages 42 to 48 (<http://dx.doi.org/10.1016/j.electacta.2013.03.149>). Sabine Kuss, Christian Kuss, Dao Trinh, Steen Brian Schougaard and Janine Mauzeroll are co-authors of this article. The Supporting Information for this publication can be found in Appendix B. The License Agreement between McGill University and Elsevier was provided by the Copyright Clearance Center (License number 3674390932266).

As explained in detail on pages 25-28, the contribution to this work by all co-authors involved:

- Sabine Kuss: Design of experiments, performance of experiments, data analysis and treatment, preparation of figures and manuscript
- Christian Kuss: Performance of experiments, preparation of manuscript
- Dao Trinh: Numerical Modeling, preparation of manuscript
- Steen Brian Schougaard: Supervision
- Janine Mauzeroll: Supervision, preparation of manuscript

3.1 Abstract

Scanning electrochemical microscopy (SECM) is increasingly applied to study and image live cells. To reduce the overall analysis time during live cell SECM measurements and maintain cell viability, the microelectrode scan rate can be increased. The use of increasing microelectrode scan rates is challenging because our understanding of the downstream convection effects is tied to the ill-defined topography of the imaged live cells. The present study investigates the effect of forced convection on the microelectrode current during SECM imaging of live cells, model non-planar substrates and planar surfaces. Experimentally, we demonstrate that during constant height imaging, the normalized peak current observed during line scans on all three substrates scales linearly with the microelectrode velocity. This quasi-linear relationship is corroborated by finite element simulations of non-planar substrates, which further reveal that the slope is closely related to the electrochemical activity of the substrate.

3.2 Introduction

Scanning electrochemical microscopy (SECM) has been widely used to study complex surfaces, such as corroding metals^{23,137} and biological samples.^{100,105,138,139} SECM is a versatile analytical method that offers several modes of operation. In the feedback mode, the microelectrode approaches a surface while biased at a potential far exceeding the standard potential of a dissolved redox mediator. When approaching an insulating surface, the diffusion of the redox mediator to the microelectrode surface is hindered by the physical presence of the substrate. The hindered diffusion leads to an overall decrease of the microelectrode current with decreasing distance (so-called negative feedback). Alternatively, the overall microelectrode current increases with decreasing distance when the microelectrode approaches a conductive surface, which is capable

of regenerating the chemical species consumed at the microelectrode. This establishes a redox cycle which leads to an enhanced material flux at the microelectrode surface that overrides the hindered diffusion process. A plot of the microelectrode current i_T versus the tip to substrate distance (d) as the microelectrode is moved in a direction normal to the substrate, is called an approach curve. A plot of i_T versus distance as the microelectrode is moved in a line parallel to the substrate, is called a line scan. Typical approach curves and line scans for a conductive substrate (infinite rate of regeneration) and insulating substrate (zero rate of regeneration) are plotted using dimensionless forms of current, to facilitate comparison. Classically, the normalizing current is the microelectrode current observed far away from the substrate. Under steady state conditions (i.e. infinitely slow scanning) the microelectrode current depends exclusively on: the tip to substrate distance, the microelectrode geometry³⁴ and the electrochemical reactivity of the substrate.³¹ However, during high velocity line scans, the displacement of the microelectrode exerts a force on the electrolyte, which results in forced convection that may significantly influence the measured microelectrode current.

Hydrodynamic effects caused by SECM tip displacement were first examined by Combellas et al.⁴² who used hydrodynamic finite element modeling of a scanning microelectrode over a flat substrate. The authors concluded that for small tip to substrate separation, $d \leq 2.72 \mu\text{m}$ and large RG values, $RG > 15$, a Couette type laminar flow is induced below the active part of the moving electrode. This flow deviates from the Couette behavior with increasing microelectrode to substrate distances. Moreover it was shown that the induced mass transport to the electrode is negligible at low scanning velocities, but above a threshold of $v_0 a / D \geq 0.06$ (with v_0 : scanning velocity, a : electrode radius, D : diffusion coefficient of electrochemical species) the current is perturbed by the induced convective flow. Further increases in scanning velocity lead to a second

limiting case, where the current increases linearly with the cube root of the velocity. Further treatments of forced convection in SECM was published in 2007 by Nkuku et al.¹⁴⁰ followed by Cornut et al.¹⁴¹, who analyzed the influence of forced convection on the microelectrode current during approach curves performed in ionic liquids and aqueous solutions respectively. Finally, these studies have also sparked interest in modified SECM techniques, such as tip position modulation SECM¹⁴² or AFM-derived SECM.¹⁴³

Herein, we extend the study of forced convection during SECM imaging to substrates having non-uniform topography and reactivity. Non-planar substrates are expected to generate microelectrode currents concomitantly affected by the microelectrode velocity, the microelectrode geometry, the substrate topography and its reactivity. Significant deviations from the Couette linear flow model are expected and required the development of advanced time dependent finite element modeling in order to explain the experimental behavior observed during constant-height SECM line scans performed over adhered living cells and their electrochemical model systems.

3.3 Material and Methods

3.3.1 Materials and Reagents

Unless otherwise specified, all reagents were purchased from Aldrich, Canada. The electrochemical measurements were performed in “nanopure” water (>18 MΩcm) solutions containing ferrocenemethanol (FcCH₂OH; 97 %), and potassium chloride (KCl) or potassium nitrate (KNO₃). “Nanopure” water was obtained from a Millipore Milli-Q Biocel Ultrapure water system (Fisher, Ottawa, ON). Electrode materials used were 25 μm diameter Pt-wire (purity 99.9 %; hard; Goodfellow, USA), quartz capillaries (L, 150 mm; o.d., 1 mm, i.d., 0.3 mm; Sutter Instrument, USA), electrically conductive silver epoxy (EPOTEK H20E; Epoxy Technology Inc.,

Canada), and standard copper connection wires (diameter, <0.3 mm). Polishing materials (Buehler, Canada) used were abrasive disks (800, 1200 grit), diamond lapping film disks (1, 0.3, and 0.05 μm diamond size), and alumina suspensions (1, 0.3, and 0.05 μm particle diameter). Electrodeposition of mercury onto Pt micro-sized-substrates was accomplished from mercuric nitrate ($\text{Hg}_2(\text{NO}_3)_2 \cdot 2\text{H}_2\text{O}$; 97 %) solutions acidified with 0.5 % HNO_3 . For cell culture, Dulbecco's modified eagle's medium (DMEM high glucose, HyClone, UT, USA) was completed with 10 % (v/v) heat inactivated fetal bovine serum (Gibco/Invitrogen, ON, Canada), 2 mM glutamine, penicillin and streptomycin (50 units/mL) (HYQ HyClone, UT, USA) (DMEM+).

3.3.2 Microelectrode Fabrication

Pt microelectrodes were produced following an established laser pulling protocol²³ that reproducibly yielded microelectrodes of well-defined geometry.³² Briefly, a 25 μm diameter Pt wire was inserted and sealed into a quartz capillary using a laser puller (P2000, Sutter Instrument, USA). The unsealed end of the Pt wire was electrically connected to a larger copper wire with silver epoxy. The sealed end of the microelectrode was polished to expose the disk platinum wire. The diameter of the exposed platinum, following polishing, was measured using an optical microscope (Nikon Eclipse 50i, CAN) and was consistently found to be 25 μm .

In order to produce Pt micro-sized-substrates, the glass embedded Pt microelectrodes were further immobilized into an epoxy polymer (Epoxy Technology, MA, USA) and polished to a flat surface, using a Buehler EcoMet 3000 polisher, BuehlerMet abrasive disks of increasing grit, and alumina suspensions down to 0.1 μm particle size.

Electrodeposition of metallic mercury onto the Pt micro-sized substrate followed a previously published procedure.¹⁴⁴ Briefly, -500 mV vs. an $\text{Hg}/\text{Hg}_2\text{SO}_4/\text{K}_2\text{SO}_4$ (sat) reference electrode was imposed for 300 s at the Pt disk electrode immersed in an aqueous 0.1 M $\text{KNO}_3/10$ mM

$\text{Hg}_2(\text{NO}_3)_2/0.5\%$ HNO_3 solution. The electrodeposition was deemed successful if, following mercury deposition, the proton reduction overpotential shifted to more negative potentials by more than 600 mV from that observed at bare Pt in a 0.1 M KNO_3 solution (Figure B1).

3.3.3 Cell Culture and Sample Preparation

HeLa (CCL-2, American Type Culture Collection, VA, USA) were grown in DMEM+. Cells were maintained in tissue culture flasks (Sarstedt Inc., QC, Canada) at 37 °C and 5 % CO_2 using CO_2 /multi-gas incubator (Sanjo Scientific, Japan). Both cell lines, ranging from 70 % to 90 % confluence, were washed with 37 °C phosphate buffered saline (PBS, Sigma–Aldrich) (pH 7.4 at 25 °C) and harvested with 37 °C 0.25 % (v/v) trypsin–ethylenediaminetetraacetic acid (EDTA, Sigma–Aldrich) solution (2.0 g EDTA, in 0.9 wt.% NaCl). The cells (50,000) were seeded onto a Zeonor plastic substrate in a 15 mm × 30 mm Petri dish and incubated at 37 °C and 5 % CO_2 for 24 h. Immediately prior to the SECM measurements, the cells were incubated in 1 mM FcCH_2OH for 70 min as previously reported.⁸⁷

3.3.4 SECM Measurements

Constant height imaging of live cells was performed on a scanning electrochemical microscope hyphenated with an optical microscope, enabling the precise positioning of the microelectrode above the adhered cell.⁶¹ Constant height imaging of the Pt and Hg/Pt substrates were also performed on this instrument, but did not benefit from the optical microscope capabilities given that both substrates were opaque. Live cell measurements used DMEM as an electrolyte solution in combination Ag/AgCl reference electrode, whereas Pt and Hg/Pt substrates used 0.1 M KNO_3 electrolyte and $\text{Hg}/\text{Hg}_2\text{SO}_4/\text{K}_2\text{SO}_4$ (sat) to avoid mercury salts precipitation. All reported potential in this study have been converted to Ag/AgCl/ Cl^- (0.1 M) reference electrode. A 0.5 mm diameter platinum wire was used as counter electrode in all electrochemical measurements.

Prior to line scan imaging, the 25 μm diameter Pt microelectrode (RG = 5) was vertically positioned 12 μm away from the surface, as determined by a negative feedback approach curve performed at 0.5 V biased, 1 $\mu\text{m/s}$ scan rate in a solution containing 1 mM FcCH₂OH. A 2D image survey of the substrate was then conducted in order to pre-position laterally the microelectrode within a 100 μm of the substrate feature. For the live cells, this was readily accomplished using the optics of the scanning electrochemical microscope. For the Pt and Hg/Pt microelectrode substrates, 150 mV of bias was applied to the substrate to provide electrochemical contrast based on positive feedback during the 2D survey scan. As the microelectrode crossed the biased substrate microelectrode, the [FcCH₂OH]⁺ produced at the scanning microelectrode was reduced back to FcCH₂OH, which leads to enhanced mass transfer, increased current and positive feedback. Following the identification of the location of the investigated feature using the 2D survey scan, the microelectrode was positioned 100 μm to the left of the feature.

Constant height SECM line scans of 300 μm length were performed across the three different substrate features with a measurement frequency of 1 point/ μm . The microelectrode velocity was incrementally varied from 2 $\mu\text{m/s}$ to 50 $\mu\text{m/s}$. To compare the experimental line scans with the numerical simulations, the tip current is normalized. Because of the transient nature of the high velocity experiments, the experimental tip current at each scan velocity is normalized by a single current value such that the resulting normalized current far away from the substrate at steady state is unity. The position of the normalized peak current reported in the high velocity dependencies is selected at the highest microelectrode velocity (50 $\mu\text{m/s}$).

3.4 Theory and Simulations

Numerical simulations were performed to quantify the SECM tip current dependence on the geometry of the substrate, the tip velocity and the heterogeneous kinetics occurring at the substrate. We first defined the mass transport expression, composed of diffusion, migration and convection, which follows the Navier–Stokes equation system for the fluid velocity and pressure.¹⁴⁵ Given the experimental conditions described in Section 2, the contribution from ionic migration is negligible because the initial solution containing 1 mM FcCH₂OH has an excess supporting electrolyte of 0.1 M KCl (or KNO₃). Therefore

$$\frac{\partial c}{\partial t} = \nabla * (D \nabla c) - u * \nabla c \quad (3.1)$$

where c and D are the concentration and diffusion coefficient of FcCH₂OH, respectively ($D = 6 \times 10^{-6}$ cm²/s¹⁴⁶) and u is the fluid velocity of the incompressible fluid flow in solution (m/s). Secondly, we define the simulation domain over which Eq. (1.1) will be solved. The geometrical parameters used in the numerical simulations were chosen based on the experimental setup dimensions (Figure B2). For a given substrate, the geometry of the substrate was fixed effectively neglecting tip induced deformation of the substrate that could arise as the tip velocity was varied. A microelectrode with an RG of 5 was used for numerical simulations. At the microelectrode tip, FcCH₂OH was oxidized with diffusion controlled kinetics: a constant potential $E_{\text{tip}} = 0.5$ V and standard kinetic constant of $k_0 = 0.2$ cm/s were used.^{147,148}

The current density i_{tip} (A/m²) at the microelectrode tip depends on the kinetics and the mass transport of the electroactive species in the solution, herein modeled using the Butler–Volmer equation:

$$i_{tip} = nFk_0(c_{Fc} \exp\left(-\alpha \frac{nF}{RT}(E_{tip} - E^0)\right) - c_{Fc+} \exp\left((1 - \alpha) \frac{nF}{RT}(E_{tip} - E^0)\right)) \quad (3.2)$$

where the number of transferred electrons $n = 1$, the standard potential $E^0 = 0.154$ V, the charge transfer coefficient $\alpha = 0.5^{148}$, and c_{Fc} is the concentration of FcCH₂OH. In the case of a conductive substrate (live cells, Hg/Pt, Pt), the reverse reduction reaction of FcCH₂OH⁺ to FcCH₂OH occurs at the surface of the conductive substrate. In the case of an insulator, such as epoxy or plastic, no regeneration reduction reaction of FcCH₂OH⁺ occurs hence the concentration gradient at the insulator surface is null.

$$\frac{\partial c_{Fc}}{\partial z} = 0 \quad (3.3)$$

By scanning the microelectrode from left to right with different scan velocities, v , the interaction between the solid structure (electrode) and the fluid exerts the force, F , on the fluid. This force is a function of the fluid velocity, u , and the pressure, p :

$$\frac{\partial u}{\partial t} = F - (u * \nabla)u - \frac{1}{\rho} \nabla p + \eta \nabla^2 u \quad (3.4)$$

$$\nabla * u = 0 \quad (3.5)$$

where u is the velocity field (m/s), ρ is the density of the fluid (kg/m³), F is the force exerted on the fluid, p is the pressure field (kg/m³) and η is the dynamic viscosity of the solution (Pa s). The fluid is incompressible, therefore the volume is conserved over time (Eq. (3.5)).

The amount of force exerted on the fluid depends on the scanning velocity of the moving microelectrode.

$$\rho_{solid} \frac{\partial^2 v}{\partial t^2} = F + \nabla * \sigma \quad (3.6)$$

where ρ_{solid} (kg/m³) is the density of the tip material, σ (Pa) is the stress imposed on the tip, which is a function of Young's modulus, Poisson's ratio and the velocity of the moving microelectrode. The values of these parameters are taken in the materials library of Comsol Multiphysics as the properties of the material of the tip (platinum). As boundary conditions, we assume that u is null at the substrate and equal to the scanning velocity (v) at the tip. The simulation framework then solves for u using (1.4) and (1.6). The fluid velocity is considered here as the results of the interactions between the moving rigid solid and the incompressible flow. Using the Arbitrary Lagrange-Eulerian (ALE) methods for the problem of a deforming fluid grid in the presence of Lagrangian moving solid, this framework can calculate the fluid velocity resulting from microelectrode scanning in any direction.

The numerical solution of the equations is performed using Comsol Multiphysics 4.3, with a Dual CPU 3.16 GHz Intel Processor having 4 GB of RAM. The average calculation time for one line scan of 200 μm at a specific scan velocity is about 3 min. The moving mesh algorithm is used with automatic remeshing at each new position of the scanning tip to maintain the minimal mesh quality of 0.05. The element size is calibrated for the fluid dynamics standard and defined as extra fine (3014 elements) at the surface of tip. The element size in the vicinity of the tip is optimized as small as 0.158 μm in order to get a relative error about 0.01 of the simulated tip currents.

3.5 Results and Discussion

The experimental line scans acquired over a conductive flat Pt substrate and over a dome-shaped Hg/Pt substrate are presented in Fig. 3.1a and b, respectively. Fig. 3.1a and b displays

positive feedback currents, which indicates that the conductive substrates biased at 150 mV indeed reduce the FcCH_2OH^+ to FcCH_2OH . For the flat Pt conductive substrate (Fig. 3.1a), the tip current increases with the velocity of the tip, which is in good agreement with Combellas et al.'s work.⁴² As the scanning velocity of the tip over the substrate increases; the tip current is enhanced because of the increased mass transport which stems from forced convection. Hence, the tip currents are proportional to the scanning velocity of the moving tip.

By assuming that the kinetics of the reaction on both the flat Pt conductive substrate and on the Hg drop substrate is infinitely fast, influences of substrate geometry on the tip current can be investigated. Fig. 3.1c compares the tip current dependence on the velocity for different geometry of the substrate: flat geometry of a Pt disk substrate and domed geometry of Hg/Pt substrate. Having comparable diameters (25 μm), the two substrates differ mainly in their geometry. The slope of current–velocity for the flat Pt conductor (0.004 $\text{s}/\mu\text{m}$) is slightly higher than the slope of Hg drop (0.003 $\text{s}/\mu\text{m}$). The domed geometry is less sensitive than the flat conductor because of the enhanced mass transport resulting from forced convection. This result is not unexpected given that the diffusion of the electroactive species normal to the disk Pt microelectrode outweighs the radial diffusion component as the tip is scanned over the conductive substrate.¹⁴⁴ The hemispherical substrate has comparatively more radial diffusion contribution resulting in a lower sensitivity that is inherent to the geometry of the tip. As the tip scans across the dome-shaped conductive substrate, the current measured will systematically be inferior to that measured at the flat Pt substrate.

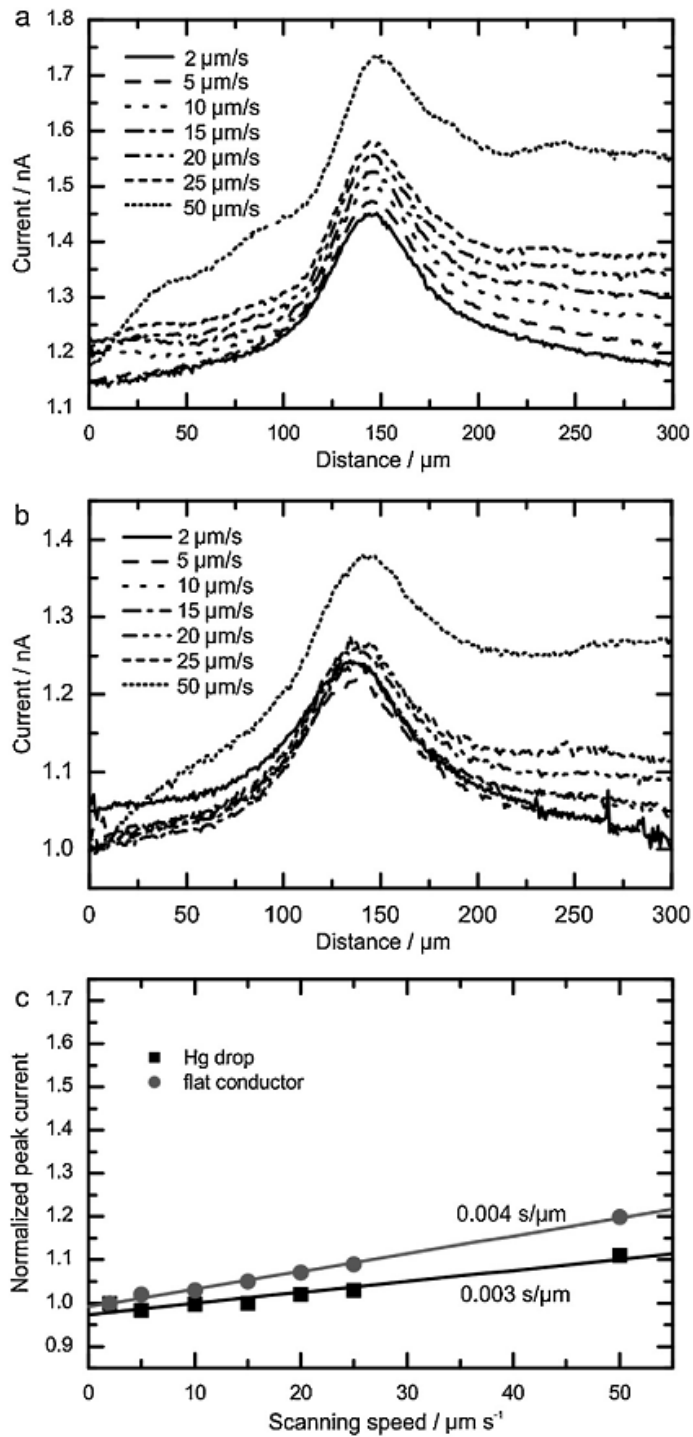


Figure 3.1. Line scans across (a) a flat Pt conductor of 25 μm diameter and (b) a mercury hemisphere of 25 μm diameter in a non-conducting surface. (c) Experimental data and linear fit of the dependence of the normalized peak current on scanning velocity for scans across the two model substrates.

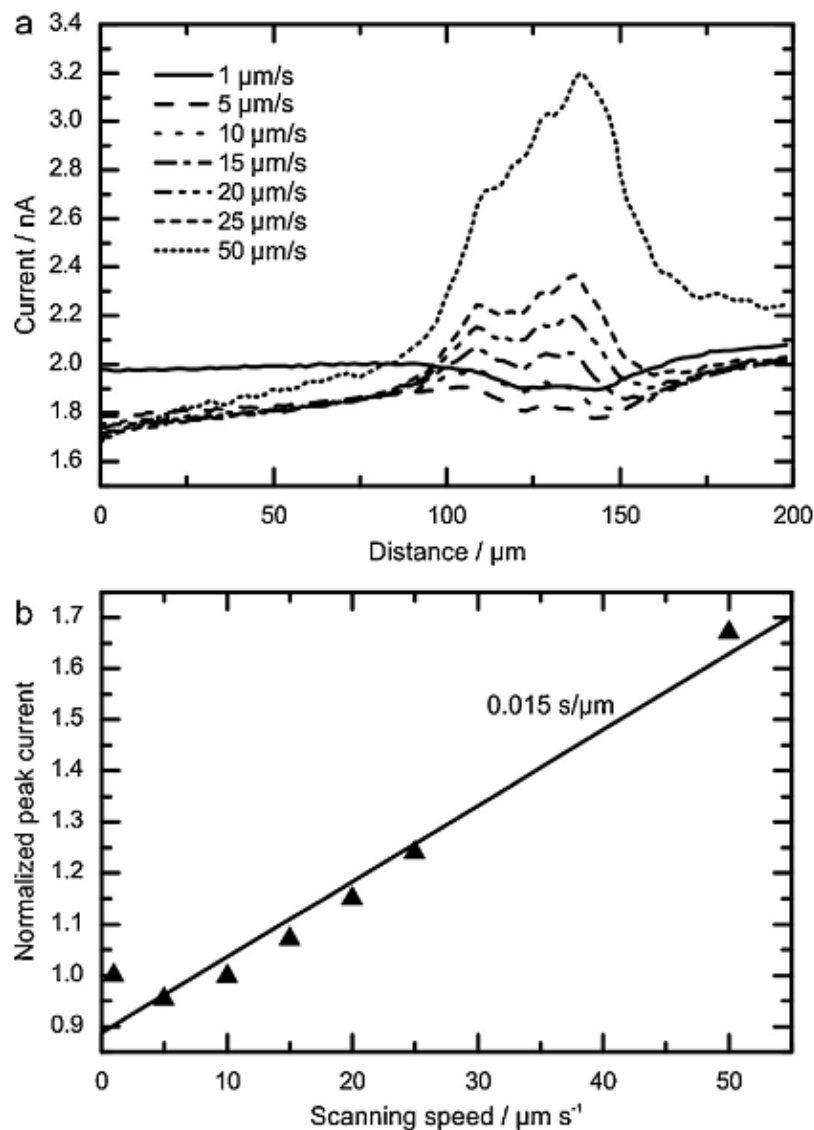


Figure 3.2. (a) Line scans over HeLa cancer cells. (b) Experimental data and linear fit of the dependence of the normalized peak current on scanning velocity for scans over human HeLa cancer cells.

Fig. 3.2 presents the experimental line scans over HeLa cells for different scanning velocities. At low velocities, $v < 15 \mu\text{m/s}$, the negative feedback current is obtained, which shows that the kinetics of the reversed redox reaction on HeLa cells is very slow or almost null. At higher velocity $v > 15 \mu\text{m/s}$, the pseudo positive feedback current is obtained as a result of increased mass

transport to the tip surface due to the forced convection of the moving tip. These results are in good agreement with the previous results of the scanning line over the conductive surface. The tip current is also proportional to the tip velocity. Fig. 3.2b shows that the slope of current–velocity is about $0.015 \text{ s}/\mu\text{m}$, which is much higher than the slope of current–velocity over the Hg/Pt substrate. Considering that the domed geometry of the HeLa cell and the Hg/Pt substrate are almost the same (semi-hemispherical geometry), one can investigate through numerical simulation how the different kinetics on the same geometry affects the current measured at the tip.

The simulated tip current related to scanning over a planar conductive substrate and over a domed conductive substrate at different scanning velocities ($v = 2\text{--}50 \mu\text{m/s}$) is presented in Figs. 3a and 4a, respectively. Above the region of the conductive substrate, due to the reversal of the redox reaction at the conductive substrate, a positive feedback is observed at both slow and fast velocities. This is in good agreement with the experimental results of the flat conductive substrate. Importantly, in this simulation framework, the kinetics of the reversal redox reaction at the conductive substrate is considered much faster than the mass transport of the species ($k_0 \rightarrow \infty$).

The fluid flow profile that develops over the substrates is shown in Figs. 3.3b and 3.4b. As the tip is moved from left to right, the fluid flow vectors show that the fluid moves in the inversed direction of the tip movement, i.e. from right to left. As observed in the research of Combellas et al.⁴² the fluid velocity develops in a region larger than the electrode substrate separation. For a planar substrate, the main contribution to the fluid flow velocity field (v_x) is in the x (scanning) direction (Fig. 3.3b). For a non-planar substrate, the fluid flow velocity field extends in both the x and y direction, as such both v_x and v_y require investigation (Fig. 3.4b). In this case, the velocity profile is no longer linear at the edge of the non-planar substrate.

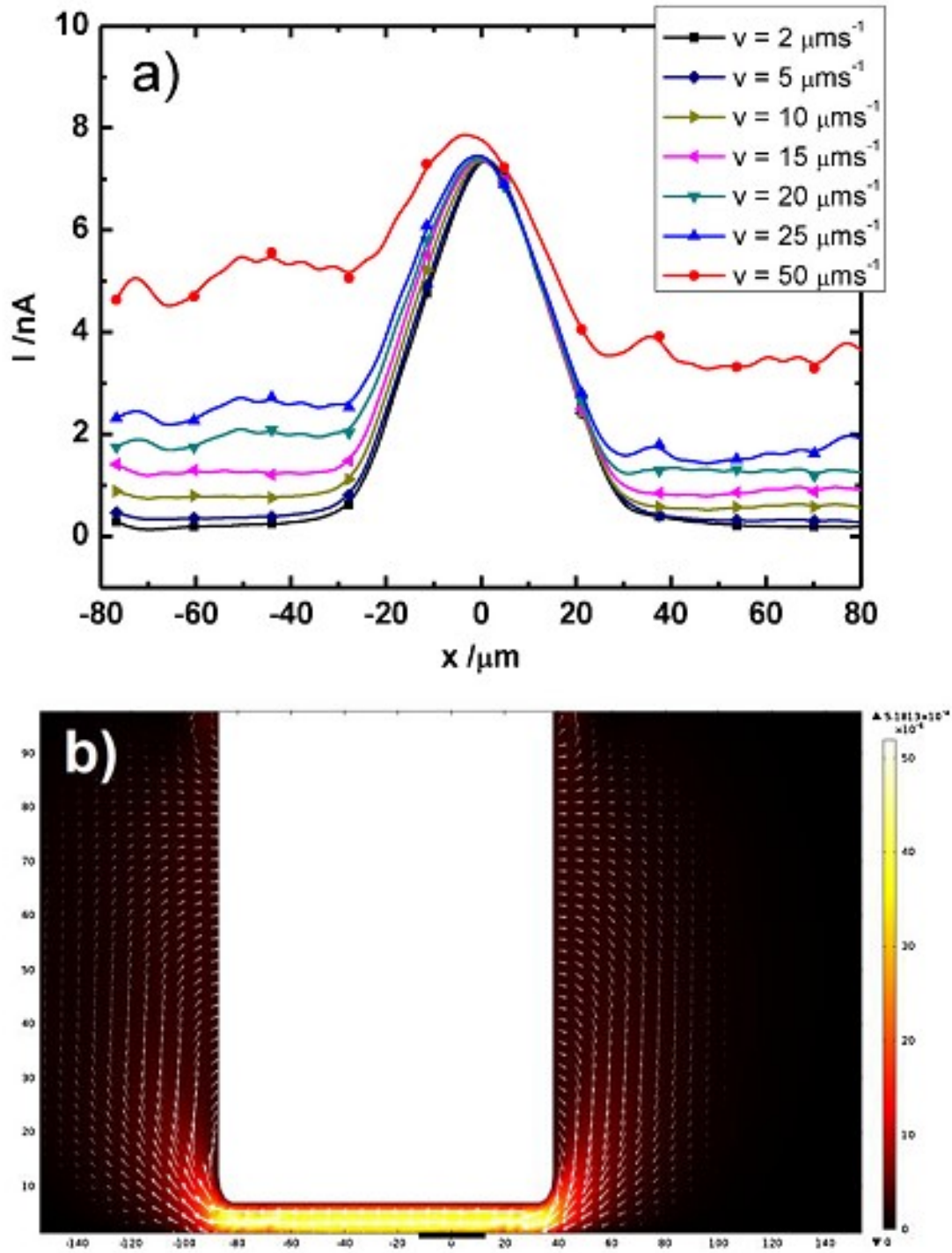


Figure 3.3. (a) Simulation result of the tip current profile of line scans across a flat conductor of 25 μm diameter, the tip-to-substrate distance $d = 8 \mu\text{m}$. (b) Velocity magnitude (m/s) and velocity field of the fluid at $y = 0$ when the tip is scanned over a flat conductive substrate with velocity $v = 25 \mu\text{m/s}$.

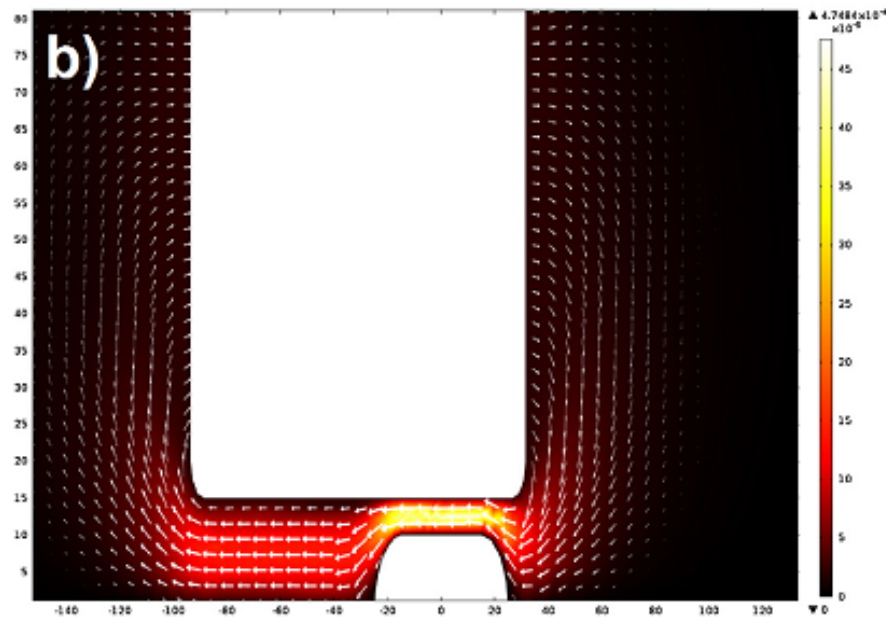
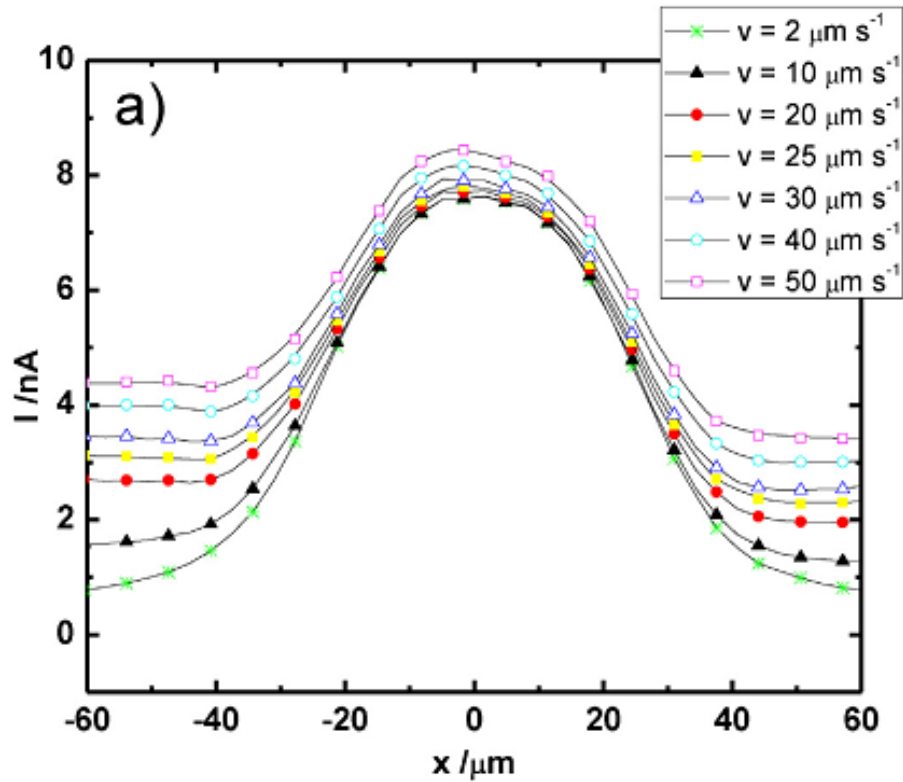


Figure 3.4. (a) Simulation result of the tip current profile at $y = 0$ over a conductive domed substrate (Hg drop) with different scanning velocity $v = 2\text{--}50 \mu\text{m/s}$, the tip-to-substrate distance $d = 15 \mu\text{m}$; (b) velocity magnitude (m/s) and velocity field of the fluid when the tip is scanned over a conductive substrate with velocity $v = 25 \mu\text{m/s}$.

Fig. 3.5a shows the current of the scanning tip over a semi hemispherical insulating substrate with different scan velocities [$v = 2\text{--}50 \mu\text{m/s}$]. At the insulating substrate the reversal of the redox reaction does not take place, i.e. $k_0 = 0$ and the tip current is controlled by negative feedback. At a slow scan velocity $v < 20 \mu\text{m/s}$, the tip current shows the negative feedback behavior over the domed insulating substrate. At a faster scan velocity, the increased current is observed near to the edge of the domed substrate due to the enhanced mass transport. As explained in Fig. 3.4b, the fluid flow develops at a larger region outside the volume under the tip, i.e. the cylindrical volume delimited by the diameter of the tip, the tip surface and the substrate area immediately below; hence the reduction current at the substrate is also increased in areas outside the projection of the tip area onto the substrate. In order to clearly identify the effect of the domed insulating substrate on the tip current, the current is normalized at distances far from the dome substrate (about $x = 60 \mu\text{m}$). At this distance, the tip current is considered constant and independent of the substrate. The normalized tip current for several velocities, presented in Fig. 3.5b, clearly shows that for slow velocity, negative feedback current is obtained when the tip is scanned over the insulating substrate area while for higher scanning velocity ($v \geq 20 \mu\text{m/s}$), a pseudo-positive feedback occurs due to the additional amount of species arriving at the tip by forced convection. These results are consistent with the experimental scanning curve over the HeLa cells (Fig. 3.2). Both the simulation and the experimental results confirm that at higher scan rate, the topography of the cell is magnified, i.e. the difference in topography is easier to measure at higher scan rate because of the enhanced mass transport at the tip. Importantly, these enhancements depend on a convolution the topography of the substrate, the scanning velocity and the kinetics of the reaction occur on the substrate.

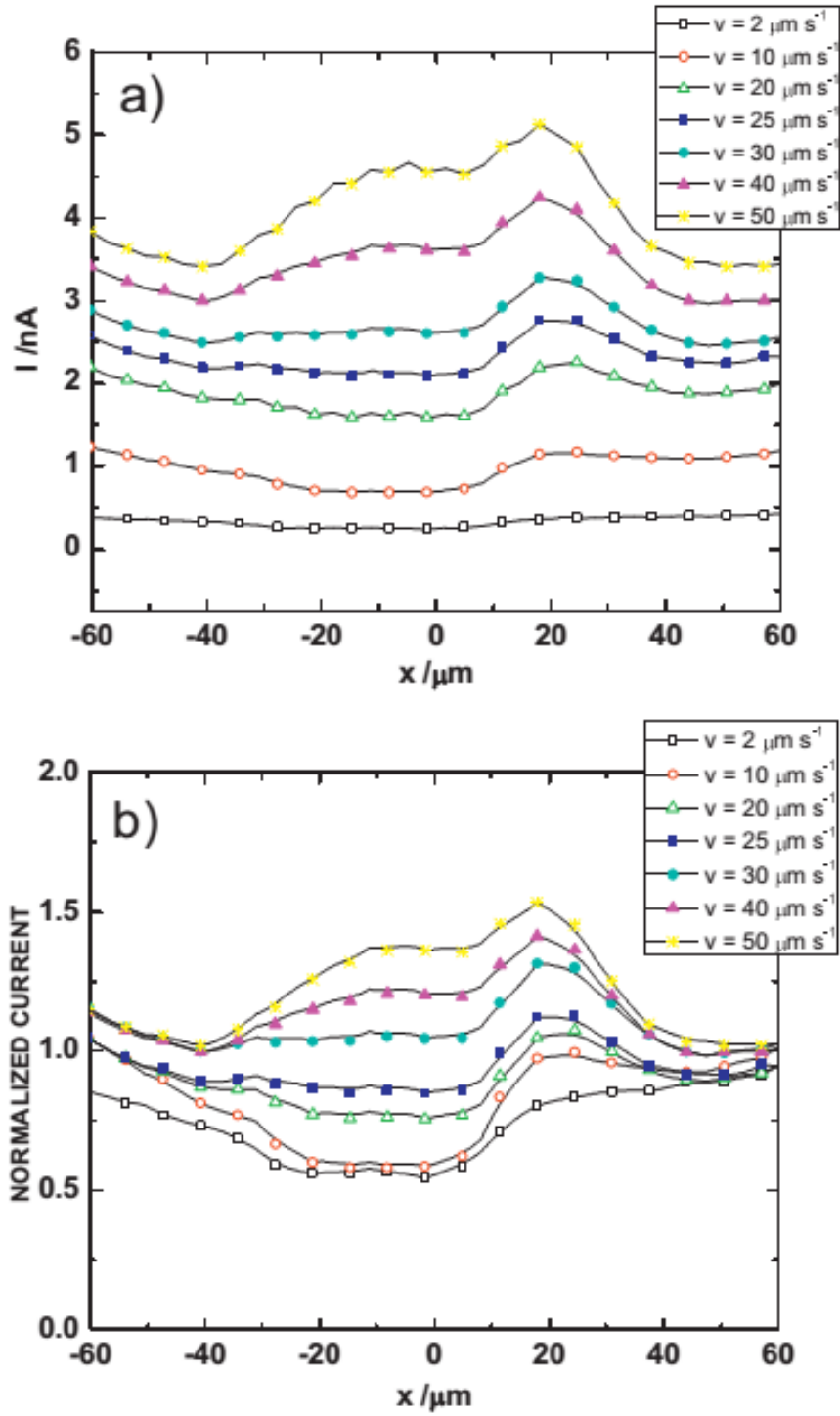


Figure 3.5. Simulation result of (a) the tip current profile and (b) normalized tip current profile over an insulating domed substrate (same shape as in Fig. 3.3b) with different scanning velocity $v = 2\text{--}50 \mu\text{m/s}$, the tip-to-substrate distance $d = 15 \mu\text{m}$, the tip current is normalized at the position far from the substrate ($x = 60 \mu\text{m}$) for each scanning velocity.

Conceptually, the HeLa cell, the modeled domed conductive substrate, and the modeled domed insulator have the same geometry. As such, one can investigate quantitatively the substrate surface kinetics through the influence of the forced convection on the scanning tip current. Fig. 3.6 shows the normalized current of the scan over the HeLa cell, the domed conductive substrate and the domed insulator substrate as a function of scanning velocity. The tip current is taken at the center of the substrate ($x = 0 \mu\text{m}$) and then normalized relative to the steady-state current above the feature ($v = 0 \mu\text{m/s}$), a value that is extracted from the simulation results. In both cases, when the velocity increases the tip current also increases, however, at different rates. The current is quasi linearly proportional to the velocity, and the slope of current–velocity depends on the kinetics of the substrate. The seemingly simple quasi-linear behavior stems from complex hydrodynamical interactions between moving electrode, immobile substrate and the liquid electrolyte. This slope is highest for the domed insulator, and lowest for the domed conductive substrate. The insulating substrate is more sensitive to the forced convection than the conductive one. The slope of HeLa cells lies between the slope of the insulating and conductive substrate, i.e. HeLa cells are not totally inert to the electrochemical reactions, but the regeneration reaction occurring at the HeLa cells has slow kinetics. Because the insulating substrate is more sensitive to the forced convection, by scanning at higher scan rate, the topography of the substrate can be magnified. This approach is useful for the case where it is difficult to determine the topography of a low-contrast substrate or the soft biological cell. On the other hand, if it is desired to avoid any influence from convection caused by the moving tip, it is possible to stop the electrode movement intermittently, in order to record the current.¹⁴⁹ This method, however, can become lengthy, depending on the chosen image size and resolution, and may thus be inadequate for samples that change behavior with time, such as biological cells.

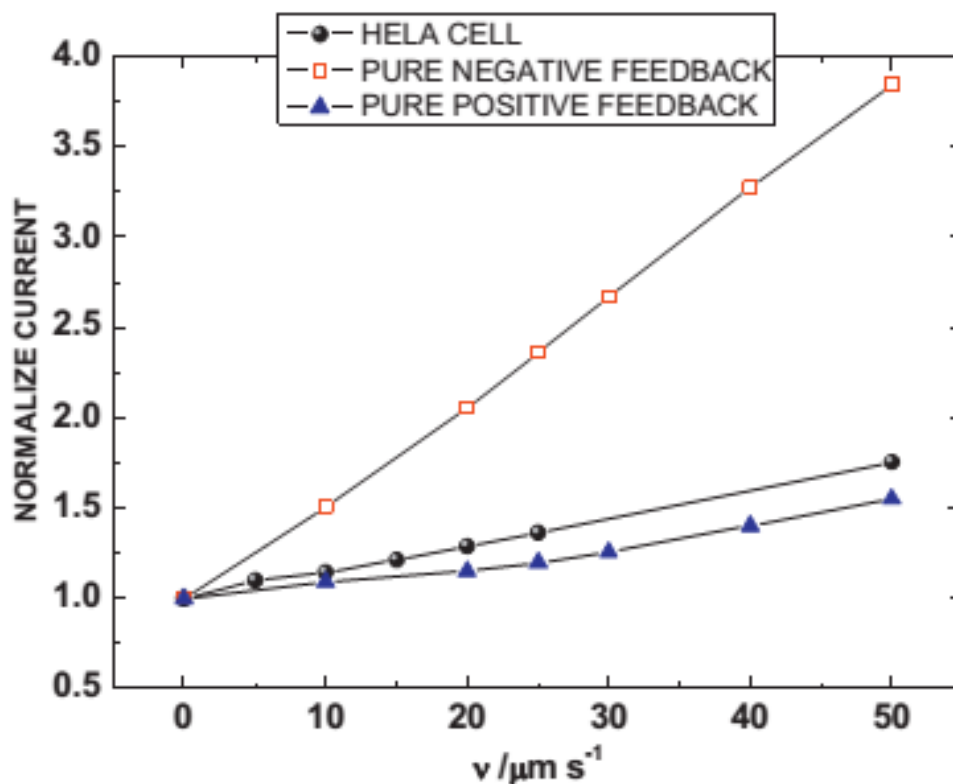


Figure 3.6. Normalized tip current as a function of scanning velocity for pure negative feedback (simulation), pure positive feedback (simulation) and HeLa cell (experiments).

3.6 Conclusions

Our findings reveal a quasi-linear dependence of the normalized peak current on the scanning velocity during SECM imaging of localized features. The slope of this curve was shown to depend only marginally on the morphology of the studied feature, but correlate significantly with its reactivity i.e. the signal of less active features depends more strongly on the scanning velocity. Hence, by varying scanning velocity over samples of similar topography, their mediator regeneration kinetics can be compared. While the current is strongly dependent on the tip to substrate distance, when the electrode is in close proximity to the substrate, the slope of the

normalized peak current as a function of electrode velocity depends mainly on the substrate kinetics, as long as the substrate topography is not perturbed significantly by the moving tip. Hence, the presented relation is particularly useful to compare the kinetics of samples of unclear topography, i.e. where the tip to substrate separation is difficult to determine. In the presented case, HeLa cells exhibit an activity to regenerate FcCH₂OH, but exhibit slow reaction kinetics compared to the diffusional mass transport to the electrode.

In order to use the observed behavior to extract kinetic constants, a separate technique, e.g. shear force SECM, would be necessary to first investigate the samples topography. Having knowledge about the sample topography, it would be possible to obtain local reactivities by fast constant height imaging.

3.7 Acknowledgements

The authors acknowledge the Natural Sciences and Engineering Research Council of Canada (NSERC) for its financial support. The technical support of Renaud Cornut is also acknowledged.

CHAPTER IV

HIGH-SPEED SCANNING ELECTROCHEMICAL MICROSCOPY METHOD FOR SUBSTRATE KINETIC DETERMINATION : METHOD AND THEORY

The previous chapter presents the appearance of a forced convection effect at increased SECM scan velocities, which was investigated over three model substrates. It is now possible to extrapolate an electrochemical signal without the contribution of forced convection and furthermore, long experimental acquisition times can be avoided. High-speed SECM imaging is desirable as live cell measurements become more accurate and controllable (chapter 2). The linear relationship of electrochemical current and scan velocity suggests a possible determination of substrate kinetics, as modeling shows a strong dependence of the linear slope on the substrate kinetics. The following chapter presents the method and theory of a high-speed SECM imaging strategy to determine a substrates apparent heterogeneous rate constant, independent from its topography. A one-step read out method is presented for substrates allowing high-speed SECM imaging. Additionally, for samples sensitive to mechanical force, such as living cells, an alternative kinetic determination method is presented, as soft substrate require investigation at regular SECM scan velocity. A comparison is made between HeLa and HeLa-R cells.

This chapter is an accepted manuscript in the journal of Analytical Chemistry (Manuscript ID: ac-2015-012685). Reprinted with permission from Kuss, S., Trinh, D., Danis, L., Mauzeroll,

J.; *Anal. Chem.* 2015. (DOI: 10.1021/acs.analchem.5b01268). Copyright 2015 American Chemical Society. Permission/License is granted by the Copyright Clearance Center for print and electronic formats.

As explained in detail on pages 25-28, the contribution to this work by all co-authors involved:

- Sabine Kuss: Design of experiments, performance of experiments, data analysis and treatment, preparation of figures and manuscript
- Dao Trinh: Numerical Modeling, preparation of figures and manuscript, supervision
- Laurence Danis: Fabrication of microelectrodes
- Janine Mauzeroll: Supervision, preparation of manuscript

4.1 Abstract

Scanning electrochemical microscopy (SECM) allows imaging and analysis of a variety of biological samples, such as living cells. Up to now, it still remains a challenge to successfully decouple signals related to topography and reactivity. Furthermore, such delicate samples require careful adjustment of experimental parameters, such as scan velocity. The present study proposes a method to extract a substrate's kinetic rate by numerical modeling and experimental high speed constant height SECM imaging. This is especially useful for the determination of substrates with unknown surface reaction kinetics and large topographical features. To make this approach applicable to soft cell samples, which cannot be imaged at high velocity, a nonlinear fit strategy is presented to obtain kinetic rate values also under slow scan velocity conditions.

4.2 Introduction

Since its introduction in 1989,^{45,46} scanning electrochemical microscopy (SECM) has become a successful technique in analytical chemistry for imaging of complex samples, such as living cells. A variety of living organisms has been imaged^{38,39} to obtain qualitative and even quantitative information.^{40,150} However, in vitro cell studies by SECM are not trivial. Once a microelectrode is prepositioned above a target sample, experimental parameters, such as scan velocity, tip to substrate distance, electrolyte content, and total analysis time, have to be chosen sensibly and adapted individually for each sample to ensure cell viability and integrity. Slow scan rates increase analysis time and result in prolonged cell exposure to nonphysiological conditions, which can alter cell metabolism or even lead to cell death.¹¹⁰ Fast scan rates advantageously shorten the overall analysis time during imaging studies. The development of soft microelectrode arrays for high throughput SECM is an interesting approach toward the reduction of analysis

time.^{151–155} These studies are usually carried out in contact mode, where a soft stylus probe is dragged across the underlying substrate, allowing imaging of large and strongly tilted surfaces. However, since living samples are especially sensitive to mechanical force, they are in many cases unsuitable for single cell analysis. Especially, when measuring cell metabolites, physical contact between a microelectrode and a target cell might result in unwanted morphological or metabolic changes of or in the cell of interest.

The effect of forced convection on the microelectrode current due to the displacement of the tip at moderate (5 to 50 $\mu\text{m/s}$) or high scan ($>50 \mu\text{m/s}$) velocities has been investigated for the scan direction normal to the substrate,^{141,156} vertically oscillating microelectrodes,¹⁴² and also parallel to the substrate.^{42,157} The determination of substrate kinetics using SECM approach curves is very possible;^{34,141} however, in addition to the previously mentioned disadvantages of physical contact between electrode and cell, this method holds the risk of damaging or deforming a soft cell sample. Lateral SECM imaging is commonly used for live cell analysis. A microelectrode is placed in close proximity to the surface and rastered horizontally across an area of interest. In SECM feedback mode, either the measured microelectrode current is decreased due to the presence of a nonconductive elevated feature on the surface (negative feedback) or the current signal is enhanced by increasing material fluxes from a so-called conductive substrate (positive feedback). As the microelectrode is scanned in constant height imaging mode across a planar surface, the current increases with increasing velocities, due to increased mass transport which results from forced convection.¹⁵⁷ This current increase becomes very sensitive to the reactivity of the substrate at high scan rates as shown in the literature.⁴² Kanoufi and co-workers studied the velocity profile of the fluid under SECM experiment conditions for planar substrates and showed a fluid flow behavior that followed Couette's law. Also known as linear-shear flow, Couette's law describes the laminar

flow of a viscous medium in between substrate and microelectrode, whereas the fluid velocity changes linearly from zero at the underlying substrate to the tip velocity at the microelectrode surface. At scan velocities exceeding 10 $\mu\text{m/s}$, the tip motion causes a linear shear flow that leads to non-negligible convection currents. Although, at very high scan rates, the microelectrode may even lose its ability to discriminate between conductive or insulating substrates,⁴² such scan rates have to be chosen in cases when a sample, e.g., a biological cell, might degrade under prolonged analysis times.

High speed SECM measurements of single live cells are confronted with the difficult task of decoupling the nonplanar, irregular topography of cells from their electrochemical reactivity. Both, cellular electrochemical reactivity and topography, are strongly dependent on several cellular regulatory factors, such as telomerase activity¹⁵⁸ or NF- κ B function,¹⁵⁹ which are strongly dependent on the cell cycle stage. In order to decouple the current resulting from topographical changes and the signal related to the reactivity of a substrate, alternative SECM modes have been developed, such as constant distance mode^{54,56} or SECM/AFM.^{43,160} However, these approaches represent highly complicated instrumentation compared to the standard constant height mode. Recently, we proposed a method that allows the extraction of the current signal during SECM imaging without the contribution of a forced convection effect, by imaging a target sample at different velocities (2 to 50 $\mu\text{m/s}$).¹⁵⁷ Herein, we propose a strategy to make further use of high speed SECM imaging in constant height in order to investigate the forced convection effect over substrates with large topographical features. By increasing the scan velocity, the analysis time can be reduced from hours to a few minutes; hence, larger sample areas can be measured. Furthermore, it is even possible to extract a substrate's kinetic rate by numerical modeling. SECM instruments, scanning at high velocities, are not standardized, and the overall quantitative analysis of samples

at high scan rates is difficult as shown in literature.¹⁴¹ Our group demonstrated previously that a tip angle misalignment can hardly be avoided and also has an impact on the measured current. For these reasons, we looked at the extraction of substrate kinetics under slow scan velocity conditions experimentally as well as theoretically. If samples, such as living cells, require a more gentle analysis, so that high scan velocities cannot be applied, the extraction of the kinetics becomes more complex but can also be achieved by numerical modeling.

4.3 Materials and Methods

Unless indicated otherwise, all materials and reagents were purchased from Sigma-Aldrich, Canada.

4.3.1 Microelectrode Fabrication.

In short, soda-lime glass capillaries were pulled using a P-2000 micropipette puller in order to fabricate two symmetric micropipette tips. A 1 cm Pt wire was inserted into the pulled micropipette tip. Using a PC-10-CA vertical pipet puller, the wire/fiber was sealed by centering the assembly inside a Kanthal (iron–chromium–aluminum) heating coil and applying heat under vacuum to avoid bubble formation. The sealed wire/fiber was connected to a Cu wire using conductive silver epoxy. The assembly was inserted into a larger borosilicate capillary. A gold connector pin was then soldered to the copper wire, completing the electrode fabrication. The electroactive surface of the UME was exposed using a variable speed grinder/polisher.³⁰

HeLa cells (CCL-2, American Type Culture Collection, VA, USA) were cultured in Dulbecco's Modified Eagle's Medium (L-glutamine, 4500 mg/L glucose, and 110 mg/L sodium pyruvate). The growth medium (DMEM+) was completed with 10 v/v-% heat inactivated fetal

bovine serum, 3.7 g/L sodium bicarbonate, and penicillin and streptomycin (50 units/mL) (HYQ HyClone/Thermo, UT, USA). Cells were grown in tissue culture flasks (Sarstedt Inc., QC, Canada) and incubated at 37°C and 5% CO₂ using an HERAcell150I CO₂/Multigas incubator (ThermoFisher, MA USA). Once cell lines reached a confluence of 75% to 90%, cultures were washed with phosphate buffered saline at 37°C (PBS, pH 7.4 at 25°C) and harvested with 37°C 0.25 v/v-% trypsin-ethylenediaminetetraacetic acid (EDTA) solution (2.0 g EDTA, in 0.9 wt % NaCl). In a 15 mm×30 mm Petri dish, 50 000 cells were seeded and incubated at 37 °C and 5% CO₂ for 19 h. Prior to the SECM measurements, cells were exposed to culture medium lacking serum (DMEM–) containing 1 mM FcCH₂OH for 75 min as previously reported.⁸⁷

4.3.2 SECM Measurements.

All samples were imaged in constant height imaging mode using an SECM (EIProScan system ELP3, with POTMASTER software version V2 ×66 and the EIProScan Controller ESC 3, HEKA Elektronik, Germany), equipped with an integrated optical microscope. Prior to imaging, the 25 μm Pt electrode (RG = 5) was approached manually until the microelectrode tip became visible in the microscopy at approximately 100 μm from the surface. Biased at 0.4 V in 1 mM FcCH₂OH, the microelectrode was positioned 12 μm above the substrate by the negative feedback approach at a scan rate of 1 μm/s. Cell measurements were carried out with an Ag/AgCl reference electrode in DMEM– as electrolyte and a 0.5 mm diameter platinum wire as auxiliary electrode.

Single target cells were quickly identified with the use of the optical microscope. All three model substrates, flat insulator and flat Pt and Hg/Pt hemispherical microelectrode substrate, were imaged over an area of 300 μm length with a resolution of 1 point/μm. All line scans were carried out in the scan direction left to right, as demonstrated in Figure S3, Supporting Information. The Pt electrode velocity was subsequently ranged from 2 to 50 μm/s. Experiments on Pt and Hg/Pt

substrates were performed in 0.1 M KNO₃ electrolyte using an Hg/Hg₂SO₄/K₂SO₄ (sat) reference electrode to avoid mercury salts precipitation. Prior to line scans, the substrate was imaged in a 2D survey scan, while biased at a reductive potential of -100 mV vs Ag/AgCl reference electrode, in order to precisely identify the location of the conducting feature and position the microelectrode tip about 100 μm to the left. During the following experimental line scans, the substrate was held at the same potential constantly. Hence, [FcCH₂OH]⁺, produced at the scanning microelectrode, is reduced to FcCH₂OH at the biased substrate during line scan imaging.

4.4 Theory and Simulations

Numerical simulations in 3D were performed to quantify the SECM tip current dependence on the geometry of the substrate, the tip velocity, and the heterogeneous kinetics occurring at the substrate. The details of the simulation framework are described elsewhere¹⁵⁷ where the laminar flow of the electrolyte fluid was coupled with the mass transport of the electroactive species. The electrochemical kinetics observed at the microelectrode and the conductive substrate were modeled using the Butler–Volmer equation. The dynamic viscosity (0.001 Pa.s) and the density of water (1000 kg.m⁻³) were used for the electrolyte phase.

The geometrical parameters used in the numerical simulations were chosen on the basis of the experimental setup dimensions. A 25 μm Pt electrode with an RG of 5 was used for numerical simulations. The domed geometry (cell, Hg drop) is modeled as a semiellipsoid shape based on the estimated experimental values: 8, 8, and 15 μm. Figure C.1, Supporting Information, provides additional information about experimental setup and parameter estimates. The substrate's kinetic rate varies from 10⁻⁸ to 10¹ m/s. The velocity range of the moving tip is from 2 to 150 μm/s. The

tip current was normalized by the steady state current acquired in solution far away from the substrate at resting position:

$$I_{norm} = \frac{I_{tip}}{I_{ss}} \quad (4.1)$$

where I_{tip} is the measured current of the microelectrode and I_{ss} is the steady-state current of the tip positioned far away from the substrate.

The tip velocity is normalized as a shear Péclet number:

$$P_s = \frac{v a^2}{D d} \quad (4.2)$$

where v is the velocity of the moving microelectrode, a is the radius of the microelectrode, d is the tip–substrate distance, and D the coefficient of diffusion. The simulation results for several substrate kinetic rates were then fitted in an approximated function, which can be used to derive the kinetic rate from the experimental results.

4.5 Results and Discussion

SECM imaging across a nonconductive polymer substrate is presented in Figure 4.1A. Experimental line scans were acquired at different scanning velocities (Figure 4.1A left) and compared with numerical simulations (Figure 4.1A right). At a scan velocity lower than 5 $\mu\text{m/s}$, insignificant convective effects on the microelectrode current were observed. With increasing scanning rate, the measured microelectrode current increases, due to the greater mass transport, as a result of forced convection. A rapid current increase was found initially (Figure 4.1A at $x = 0$ to 100 μm), whereas the signal reached a steady state for velocities lower than 25 $\mu\text{m/s}$, once a

constant fluid movement toward the electrode was established. These results are in good agreement with numerical simulations (Figure 4.1A right) and work presented by Kanoufi and co-workers.⁴² They investigated similar conditions for a thin layer cell and reported increasing convective mass transport, and hence microelectrode current, with increasing scan velocity.

An effect of forced convection on the current signal can also be seen in samples with complex topography. As the influence of substrate geometry on the microelectrode current under forced convection has been investigated in the past,¹⁵⁷ the contribution of substrate kinetics can be analyzed. Experimental line scans across a flat Pt substrate as well as a mercury hemisphere presented in Figure 4.1B,C, respectively, confirm the positive-feedback behavior on both conductive substrates. As the conductive substrates were polarized at a reductive potential in the diffusion limited regime, the rate of electrochemical conversion of $[\text{FcCH}_2\text{OH}]^+$ to FcCH_2OH is diffusion limited. Both model substrates (flat Pt substrate and a mercury hemisphere) exhibit comparable diameters ($25\mu\text{m}$) but differ in their geometry. The current measured at the domed-shaped mercury hemisphere is greater than that at the flat Pt substrate, due to the increased active substrate surface area and the decreased tip-to-substrate distance over the Hg drop. Interestingly, the effect of forced convection on the current was found to be more pronounced at higher kinetics of the two investigated samples. Hence, it appears to depend minimally on the underlying topography. Furthermore, the extraction of the substrate kinetics by numerical simulation can be studied.

A plot of the resulting model for a flat conductor can be seen in Figure 4.2A. The value P_s describes the ratio of convective to diffusive transport in a thin mass transport layer, as stated by Combellas et al.⁴² As seen in Figure 4.2A, the slope of the peak current became very sensitive at high scan velocities ($P_s > 1$).

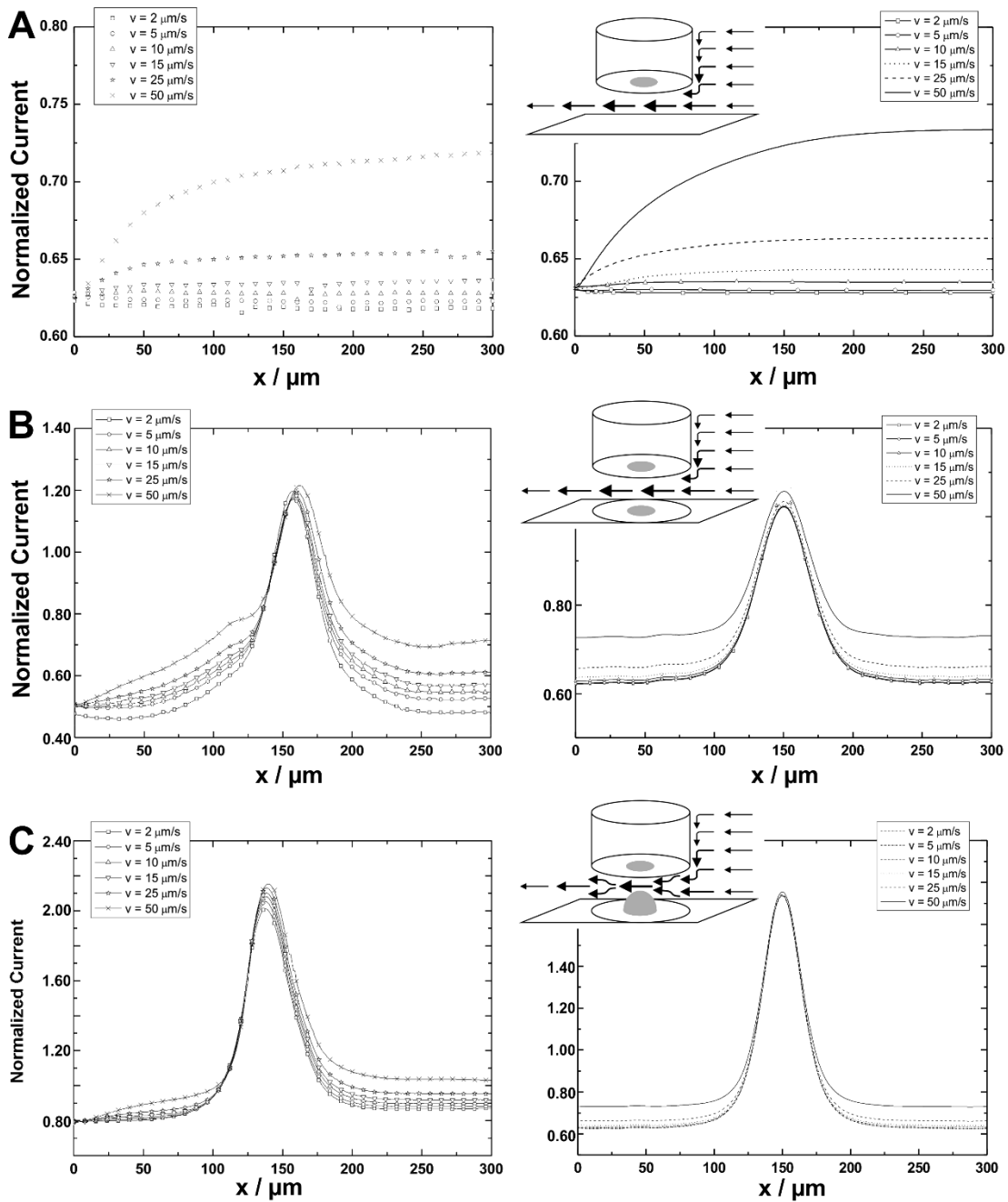


Figure 4.1: Experimental results (left panel) and simulation results (right panel) of the moving tip over a flat insulator (A), a flat conductor embedded into an insulator (B), and a mercury hemisphere deposited on the 25 μm Pt conductor (C) used in (B) at several velocities from 2 to 50 μm/s.

The slope α is defined as:

$$\alpha = \frac{\text{Log}(I_{norm})}{\text{Log}(P_s)} \text{ for } P_s > 1 \quad (4.3)$$

The dependence of the kinetic rate constant on the slope of the peak current can be seen in Figure 4.2B, which allows the extraction of specific substrate kinetics in one step after the peak current slope was determined. Scanning at a velocity of 100 $\mu\text{m/s}$ or faster is not possible with every standard SECM system. Also, delicate samples, such as living biological cells cannot be exposed to such rough mechanical force or fluid shear stress. Hence, a numerical model was developed to extract a substrate kinetic value k_0 employing slower experimental scan velocities. The normalized current depending on P_s and k_0 follows the approximation equation:

$$\text{Log}(I_{norm}) = I_0 + A \text{Exp}(r_0 \text{Log}(P_s)) \quad (4.4)$$

I_0 , A , and r_0 are the fitting parameters which depend on the kinetic k_0 . The experimental results were fitted to the equation above to find I_0 , A , and r_0 . The kinetic is then derived from I_0 , A , and r_0 by interpolation of the values presented in the Table 4.1.

Figure 4.3A represents experimental line scans over a single HeLa cell at different velocities in 1 mM FcCH_2OH . The previously reported relationship of the redox species $\text{FcCH}_2\text{OH}/[\text{FcCH}_2\text{OH}]^+$ and the intracellular glutathione leads to a positive feedback signal during SECM cell imaging.⁸⁷ In short, the diffusion of the redox species FcCH_2OH across the cell membrane promotes the intracellular generation of glutathione (GSH).⁸⁷ The resulting alteration

of the GSH/ glutathione disulfide (GSSG) ratio leads to an enhanced efflux of GSH. In close proximity to the cell membrane surface, GSH reacts with $[\text{FcCH}_2\text{OH}]^+$ to regenerate FcCH_2OH , which diffuses toward the microelectrode. The oxidation of the redox species at the electrode can be quantified as a heterogeneous rate constant. The experimental setup is schematically shown in Figure C.2, Supporting Information. At scan velocities lower than $5 \mu\text{m/s}$, the current profile shows 2 valleys (Figure 4.3B, at $x = 70$ and $93 \mu\text{m}$) that are assumed to result from the hindered diffusion of FcCH_2OH toward the approaching electrode. Once the probe was close enough to the cell to detect the species' regeneration, the current signal increased. At this moment, the positive feedback was over compensating negative feedback. When the electrode passed the cell, it is again the hindered diffusion toward the tip, now coming from the back, which caused a decrease in current, shown as a second valley. This assumption is confirmed when imaging a comparable single HeLa cell with a cell membrane impermeable redox mediator, $\text{Ru}[\text{NH}_3]_6^{3+}$, as also two valleys are visible in the current profile (Figure 4.3B). In this case, only the second valley appears sensitive to forced convection. Here, $\text{Ru}[\text{NH}_3]_6^{3+}$ gives only information about topography, where the physical presence of the cell leads to diffusion blockage of redox species toward the electrode, resulting in pure negative feedback without the contribution of regenerated material.

If pure negative feedback is reached at slow scan velocity, the current signal obtained in close proximity to the cell cannot be increased by enhanced mass transport beforehand. In contrast, once the microelectrode had passed the center of the cell and was moving out of the diffusion blockage zone, new redox species became available from solution. Similar to the effect described in Figure 4.3A, the diffusion can still be blocked on the backside of the electrode and will be dependent on the scan velocity. The appearance of two valleys is confirmed by numerical simulations as presented in Figure C.4, Supporting Information.

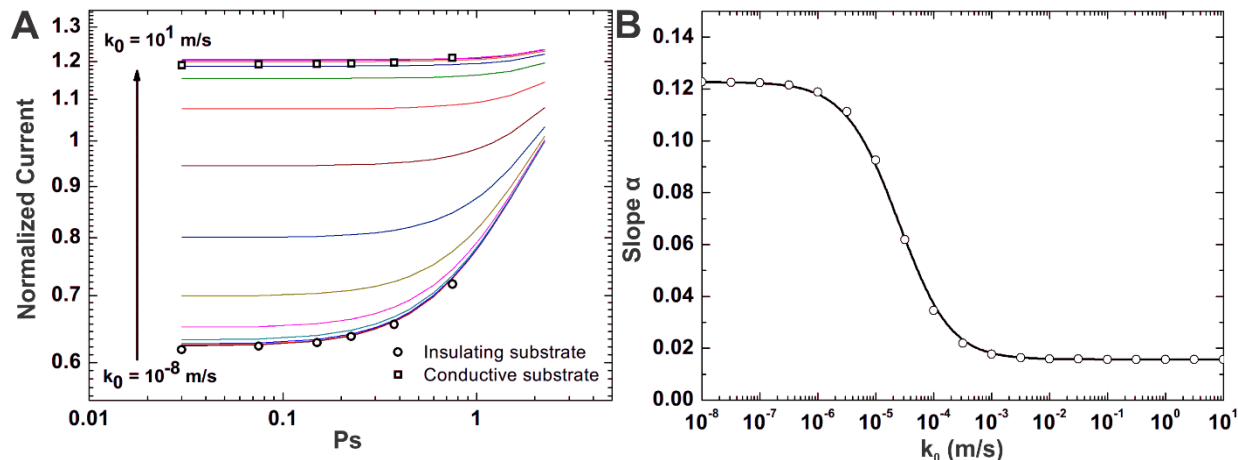


Figure 4.2: (A) Normalized current as a function of Ps in log scale: simulation results (line) for several kinetics varied from 10^{-8} to 10^1 m/s, experimental results over the insulating substrate (circle) and experimental results (square) over the conductive substrate. (B) The slope α of the normalized current taken at high Ps > 1 as a function of kinetic k_0 .

Log(k_0)	FLAT SUBSTRATE			DOMED SUBSTRATE		
	I_0	A	r_0	I_0	A	r_0
-8	-2.15331	-2.15331	2.75804	-1.63438	2.21861	0.0615935
-7.5	-2.06611	-2.06611	2.67159	-1.60699	2.19152	0.0622748
-7	-1.90093	-1.90093	2.50849	-1.59844	2.1837	0.0624185
-6.5	-1.48474	-1.48474	2.09877	-1.55621	2.1438	0.0632816
-6	-0.73557	-0.73557	1.3688	-1.47412	2.06893	0.0647512
-5.5	0.06298	0.06298	0.62118	-1.24393	1.86074	0.0692512
-5	0.58695	0.58695	0.20292	-0.721286	1.40047	0.0820847
-4.5	0.88382	0.88382	0.05526	0.0592858	0.765538	0.112157
-4	1.05518	1.05518	0.0183	0.735453	0.317631	0.157187
-3.5	1.14299	1.14299	0.00954	1.11095	0.146964	0.188654
-3	1.17862	1.17862	0.00745	1.27023	0.0984009	0.198164
-2.5	1.19109	1.19109	0.00687	1.32765	0.0848148	0.199513
-2	1.19518	1.19518	0.00669	1.34704	0.0805347	0.199975
-1.5	1.19648	1.19648	0.00664	1.3538	0.0787309	0.201022
-1	1.1969	1.1969	0.00662	1.35586	0.0782688	0.201117
-0.5	1.19709	1.19709	0.00657	1.35653	0.0781065	0.201177
0	1.19715	1.19715	0.00656	1.35672	0.078069	0.201168
0.5	1.19709	1.19709	0.00661	1.35678	0.0780597	0.201159
1	1.19704	1.19704	0.00665	1.35682	0.078041	0.20119

Table 4.1: I_0 , A and r_0 as a function of k_0 for the flat substrate and domed cell.

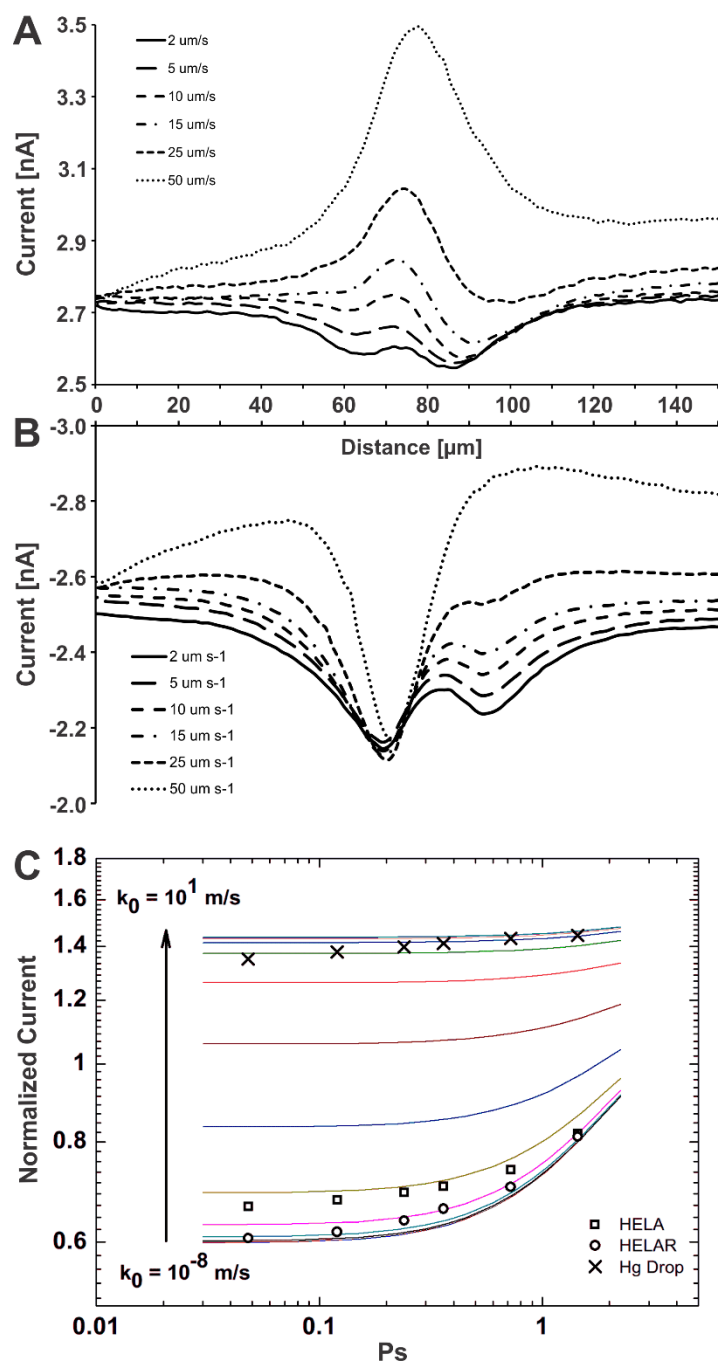


Figure 4.3: (A) Line scan across a single HeLa cell in FcCH₂OH during SECM imaging at different velocities ranging from 2 to 50 $\mu\text{m/s}$. (B) SECM imaging of a comparable HeLa cell exposed to $[\text{Ru}(\text{NH}_3)_6]^{3+}$. (C) Normalized current as a function of Ps in log scale: simulation results (line) for several kinetics varied from 10^{-8} to 10^1 m/s, experimental results over a HeLa cell (square) and a Hela-R cell (circle) as well as over a mercury drop (\times) in FcCH₂OH.

Figure 4.3C presents the numerical model adapted to conductive features with large topography. As expected, the peak current values of the mercury hemisphere model fit well in the positive feedback regime of the model. Multiple line scan cell measurements were performed in FcCH₂OH. Due to the straightforward tip positioning prior to the experiments (see Experimental Section), each single cell measurement could be completed within 10 min, so no significant change in solution temperature or salt concentration can be assumed. The average of measurements on five single HeLa cells is shown, and it can be concluded that HeLa and HeLa-R cells in their normal *in vitro* environment, without the exposure to harmful substances, exhibit a slow kinetic rate constant value (2.2×10^{-5} and 2.1×10^{-5} m/s, respectively).

4.6 Conclusion

In conclusion, we demonstrated that a substrate's electrochemical reaction kinetics can be obtained during SECM imaging in constant height mode by scanning at different scan velocities. Furthermore, the presented numerical model can also be employed for substrates with large topographical features, such as living cells, where a signal contribution from topography as well as reactivity cannot be neglected. The decoupling of topography and reactivity is otherwise only possible with significantly more complex instrumentation. The reliable determination of single cell reaction kinetics is achieved, and the effects of external stimuli on these kinetics are currently investigated.

4.7 Acknowledgements

The authors acknowledge the Natural Sciences and Engineering Research Council of Canada (NSERC) for its financial support.

CHAPTER V

HIGH-SPEED SCANNING ELECTROCHEMICAL MICROSCOPY METHOD FOR SUBSTRATE KINETIC DETERMINATION : APPLICATION TO LIVE CELL IMAGING OF HUMAN CANCER

The previous chapter presents the method and theory of a high-speed SECM imaging method for substrate kinetic determination. Substrates measured at velocities exceeding 50 $\mu\text{m/s}$ can be analysed rapidly and kinetics can be determined in a one-step procedure. Soft samples, such as living cells require regular speed SECM, however, the extraction of cell kinetics is possible, nevertheless. The following chapter presents the application of the strategy, presented in chapter IV to HeLa-cells that were exposed to Epigallocatechin gallate (EGCg), a catechins that is extracted from green tea. The antioxidant and chemopreventive properties of EGCg make it a suitable tool to induce environmental stress to cells. The electrochemical signal, related to the intracellular redox environment, is monitored over time in single living HeLa cells and gives information about the cellular timely response to such harmful substances.

This chapter shows how the SECM studies, conducted during the presented PhD work, ranging from preliminary experiments to imaging method development, can be applied to biological interesting systems and useful information are extracted.

This chapter is an accepted manuscript in the journal of Analytical Chemistry (Manuscript ID: ac-2015-012697). Reprinted with permission from Kuss, S., Trinh, D., Mauzeroll, J.; Anal. Chem. 2015. (DOI: 10.1021/acs.analchem.5b01269). Copyright 2015 American Chemical Society. Permission/License is granted by the Copyright Clearance Center for print and electronic formats.

As explained in detail on pages 25-28, the contribution to this work by all co-authors involved:

- Sabine Kuss: Design of experiments, performance of experiments, data analysis and treatment, preparation of figures and manuscript
- Dao Trinh: Numerical Modeling, preparation of figure 3
- Janine Mauzeroll: Supervision, preparation of manuscript

5.1 Abstract

Scanning electrochemical microscopy (SECM) is increasingly applied to study and image live cells. Quantitative analyses of biological systems, however, still remain challenging. In the presented study, single human adenocarcinoma cervical cancer cells are electrochemically investigated by means of SECM. The target cell's electrochemical response is observed over time under the influence of green tea catechins (GTC), which are suggested to offer chemopreventive and therapeutic effects on cancer. The electrochemical response of living target cells is measured experimentally and quantified in an apparent heterogeneous rate constant by using a numerical model, based on forced convection during high speed SECM imaging. The beneficial effect of GTC on cancer cells could be confirmed by SECM, and the presented study shows an alternative approach toward unraveling the mechanisms involved during inhibition of carcinogenesis.

5.2 Introduction

The application of electrochemical techniques to the field of biology or medical research has become increasingly important, as electrochemistry can inform on the effect of promising therapeutic substances, such as green tea catechins (GTC) on cancer. GTC are polyphenols that are known for their antioxidative properties. In addition to their antioxidant function^{161,162} by donating hydrogen atoms to capture free radicals,¹⁶³ their beneficial effect is also related to the ability to modulate signal transduction pathways,¹⁶⁴ altering the cycle¹⁶⁵ and immune response¹⁶⁶ of a cell. The most commonly studied GTCs are Epicatechin (EC), Epicatechin gallate (ECg), Epigallocatechin (EGC), and Epigallocatechin gallate (EGCg), where the latter is the most abundant and is thought to have the strongest preventive effect against chronic diseases, diabetes, neurodegenerative disease, and cancer.¹⁶⁷⁻¹⁷¹

The protective properties of GTCs on breast cells against carcinogenesis were shown in the past by various *in vitro* and *in vivo* studies.¹⁷² Most *in vitro* investigations include immunohistochemical and biochemical assays, such as immunofluorescence, flow cytometry, polymerase chain reaction, Western blotting, or gene expression microarrays in order to study cell mobility, cell proliferation, and migration (e.g., refs ¹⁷³ and ¹⁷⁴). GTCs have also been characterized electrochemically, where their oxidation and its pH, temperature, and time dependency was monitored by cyclic voltammetry.^{175,176} GTCs were found to adsorb on the electrode surface during their oxidation, whereby the oxidation product is not electroactive and results in fouling of the microelectrode.¹⁷⁶ Electrochemically, GTC levels in biological fluids, such as human serum¹⁷⁷ and plasma¹⁷⁸ after oral ingestion, were quantified, but electrochemical studies have yet to investigate the observed GTC effects on living cancer cells. With the help of electroanalytical techniques, such as scanning electrochemical microscopy (SECM), health beneficial properties of GTC, such as inhibition of carcinogenesis, can be better understood.

SECM allows the monitoring of topography and reactivity of biological samples, such as cancer cells.¹⁰⁰ Since its first application to biological samples in the 1990s, a variety of living samples was analyzed, including bacteria (e.g., refs ¹⁷⁹ and ¹⁸⁰), plant (e.g., ref ¹⁸¹) and human cell tissue (e.g., ref ¹⁸²), or cultures (e.g., refs ¹⁸³ and ¹⁸⁴). A live cell's redox environment can be followed noninvasively and even on the single cell level.¹⁸³ In principle, a microelectrode positioned in close proximity to a target cell is biased at a potential specific to a redox mediator in solution. While the microelectrode is scanned laterally across the surface, a current depending on the diffusion of the redox species toward the electrode is measured. Thereby, the obtained current signal is mainly influenced by the topography and reactivity of the sample.⁴⁵ The constant advancement of SECM has led to quantitative studies about a cell's efflux rate of metabolites, such

as glutathione (GSH)¹⁵⁰ and reaction kinetics.^{157,185} We showed previously, that with the help of numerical modeling, based on the geometry of the sample, the microelectrode velocity, and the heterogeneous kinetics of the sample, it is possible to extract a single cell's reaction kinetics and to quantify its redox environment.¹⁸⁵ The GSH/glutathione disulfide (GSSG) is the major redox couple in mammalian cells,³ and it is responsible for many cell regulatory events, such as signal transduction, gene expression, and apoptosis.^{186,187} As its concentration is superior to any other intracellular thiol redox couples, the GSH/GSSG redox state is considered a good representation of the overall cellular redox environment.¹

The present study demonstrates quantitative time-lapse cell response measurements on living human adenocarcinoma cervical cancer cells (HeLa), that were exposed to EGCg, known for its cancer preventive and health beneficial potential. Herein, the cells' ability to regenerate a redox species is measured by SECM. Depending on the cell's efficiency, the redox species diffuses to the tip of the microelectrode where it is electrochemically oxidized at a certain rate. The heterogeneous rate constant of this reaction at the microelectrode tip varies and is determined by numerical modeling, based on the previously established forced convection effect.¹⁸⁵ The recorded decrease of cellular metabolic activity confirms the beneficial effect of EGCg on cancer cells.

5.3 Materials and Methods

Unless indicated otherwise, all material and reagents were purchased from Sigma-Aldrich, Canada.

5.3.1 Microelectrode Fabrication.

Microelectrodes were fabricated using soda-lime glass capillaries and assembled following a procedure reported in the literature.³⁰ Electrodes were polished using a variable speed polisher.

5.3.2 Cell Culture and Sample Preparation.

HeLa cells (CCL-2, American Type Culture Collection, VA, USA) were cultured in Dulbecco's Modified Eagle's Medium (L-glutamine, 4500 mg/L glucose, and 110 mg/L sodium pyruvate), harvested, and seeded in Petri dishes following an established protocol as previously reported.¹⁸⁵

5.3.3 Cell Viability Measurements.

HeLa cells were seeded in 15×60 mm Petri dishes (200 000 cells/dish) and incubated for 3 days at 37°C and 5% CO₂. Complete cell growth medium (DMEM+) was substituted by cell medium lacking serum (DMEM-) to allow maximal EGCg uptake by the cells. Concentrations of EGCg, ranging from 0 to 40 μM, were added to the dish, and samples were incubated for 4 h at 37 °C and 5% CO₂. The solution was removed, and cell samples were washed using PBS. Cell viability was determined by Trypan blue staining and cell counting using a hemocytometer.¹⁸⁸ Optical micrographs were taken through an inverted microscope at a magnification of 20× (Nikon Eclipse TS100) equipped with a digital camera (Olympus CAMEDIA C-500 ZOOM). Images were analyzed using open source software "Gimp 2.4".

5.3.4 SECM Measurements.

Using 25 μm Pt electrodes (RGs ranging from 4 to 5), all samples were imaged in SECM constant height imaging mode. All measurements were performed using an Ag/AgCl reference electrode in DMEM-, providing a Cl⁻ concentration of 0.07 mol/L. A 0.5 mm diameter platinum wire was used as auxiliary electrode. During the experiment, cell morphology was observed using

the SECM integrated inverted microscope. An adequate temperature (37°C) in the Petri dish was assured by a temperature control station plate positioned inside the SECM.

Cells were preincubated for 75 min in DMEM⁻ containing 1 mM FcCH₂OH at 37°C and 5% CO₂ to ensure cells' redox environment homeostasis. Once the cell sample was transferred to the SECM instrument, the electrode was repositioned at a tip to substrate distance of about 150 to 200 μM using the SECM-integrated optical microscope. The probe was biased at 0.4 V in 1 mM FcCH₂OH and positioned 12 μm above the plastic substrate by the negative feedback approach at a distance of 100 μm to the left of the target cell. To avoid damaging or irritation of the cell, approach curves were performed over plastic and lateral line scan imaging was the method of choice. For SECM line scans across a single living HeLa cell, the scan velocity was set to 50 μm/s and imaging was carried out over an area of 300 μm length with a resolution of 1 point/μm.

As a control, a line scan across the target cell was acquired every 10 min for 60 min in total to let the cell adjust to the basic experimental conditions (absence of serum, temperature variations, etc.). Once the cell's electrochemical signal stabilized, the electrode was retracted in the z-direction and the working solution was substituted for DMEM⁻, containing 25 μM EGCg. After a cell incubation of 60 min in the presence of EGCg, the working solution was again substituted for DMEM⁻, containing 1 mM FcCH₂OH, and SECM line scans were performed for 2 h every 10 min.

5.3.5 Fluorescent Microscopy.

HeLa cells were seeded in 15×60 mm Petri dishes (200 000 cells/dish) and incubated until they reached a confluence of 90%. Cells were washed once with DMEM⁻ and a total of 5 mL DMEM⁻ (control) or 20 μM EGCg in DMEM⁻ was added. On the basis of viability studies (Figure 5.1A), samples were incubated for 60 min at 37°C and 5% CO₂. Cells were then washed once with

DMEM-, and a total of 5 mL of PBS including 3 μ M 5-chloromethylfluorescein diacetate (CMFDA) was added to the Petri dish, to allow maximal CMFDA uptake. Samples were incubated at RT for 3.5 min, while tapping the dish repeatedly to ensure a homogeneous CMFDA distribution in the dish. Cells were washed once with PBS, and 5 mL of PBS was added before fluorescent images could be taken using an Upright Research Microscope for Advanced Imaging (Zeiss Axio Imager.M2). Images were analyzed using the open source software “imageJ”

5.4 Results and Discussion

Electrochemical Monitoring of Live Cell's Redox Behavior. Alterations in cells' metabolic rate can be recorded by biological SECM. An initial line scan across a single living HeLa cell (Figure 5.1A, inset) prior to EGCg treatment shows an increase in electrochemical current when scanning across the living HeLa cell (Figure 5.1, black curve). This enhanced current is due to the active regeneration of FcCH₂OH by the cell, as reported previously.⁸⁷ In short, FcCH₂OH diffuses into the cell where it promotes the intracellular generation of GSH. The altered ratio of the redox couple GSH/glutathione disulfide leads to an enhanced GSH efflux from the cell. On the outside, GSH reacts with [FcCH₂OH]⁺, actively regenerating FcCH₂OH.⁸⁷ It is assumed that this reaction occurs fast and close to the cell membrane surface. The microelectrode is hence detecting the enhanced flux of FcCH₂OH from the cell, which is quantified as a heterogeneous rate constant. Previously, it has been shown that [FcCH₂OH]⁺ is thereby not able to diffuse across the cell membrane,⁸⁷ and hence, no flux of intracellular regenerated FcCH₂OH needs to be considered.

As catechin adsorption on the electrode surface could be confirmed as reported in the literature^{175,176} (Figure D.1, Supporting Information), the microelectrode was retracted from solution during cell exposure to EGCg to avoid microelectrode blockage. The working solution

was removed, and a fresh solution containing 25 μM EGCg was added to the Petri dish for incubation at 37°C for 1 h. A concentration of 25 μM EGCg was chosen on the basis of viability studies, presented in Figure D.2, Supporting Information. After incubation, EGCg was removed by replacing the incubation medium with fresh DMEM-. After the microelectrode was repositioned in solution, a peak current, exceeding the initial normalized current by 0.12, was observed after EGCg incubation during line scans (Figure 5.1A, red curves, peak current at $x = 140 \mu\text{m}$) across the same cell, indicating higher amounts of intracellular reduced glutathione.⁸⁷ The signal decreased over a time of 2 h toward the value found prior to EGCg exposure (Figure 5.1A, red curves). The linear scaling of the peak current behavior as a function of velocity can be seen in Figure 5.1B. Exposure to EGCg results in an increase of the slope. Furthermore, this slope decreases within 2 h to its initial value upon removal of the GTC (Figure 5.1B, red curves). To ensure that this effect is not majorly determined by a change in morphology, the target cell was monitored throughout the experiment using the SECM integrated microscope and no significant change in cell size or position could be observed.

Figure 5.2A displays a summary of experiments under different conditions (control, placebo, EGCg), with each point measured in quadruplets. The velocity is normalized by P_s , the Péclet number, which describes the ratio of convective to diffusive transport in a thin mass transport layer, as stated by Combellas et al.⁴² Herein, the tip velocity is normalized as:

$$P_s = \frac{v a^2}{D d} \quad (5.1)$$

In this equation, v is the velocity of the moving microelectrode (m/s), a is the radius of the microelectrode (m), d is the tip–substrate distance (m), and D the diffusion coefficient (m^2/s).

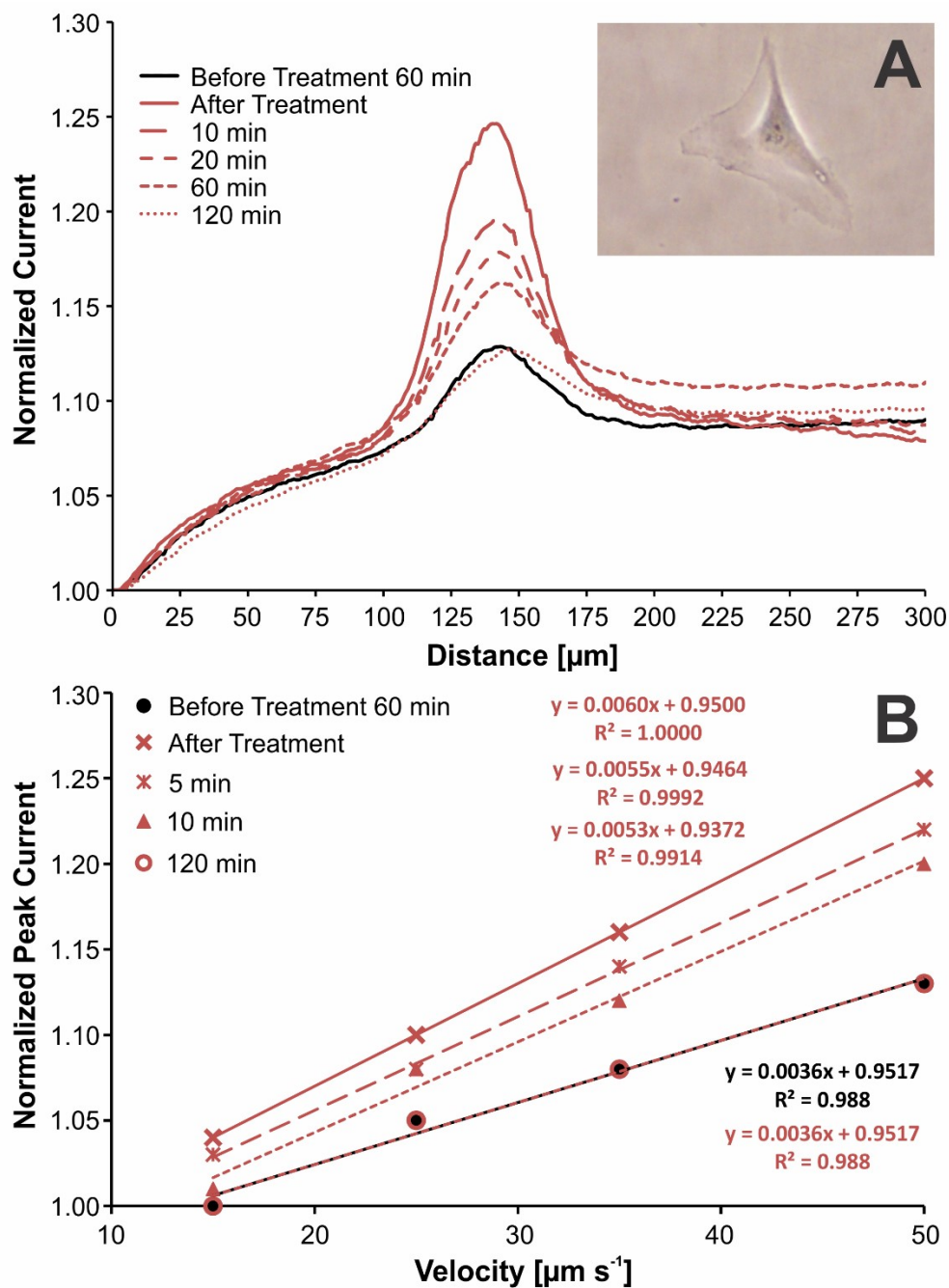


Figure 5.1: (A) SECM line scan profile at 12 μm above a single living HeLa cell at 50 $\mu\text{m/s}$ scan rate before and after treatment with EGCg. (B) Linear dependency of normalized peak current on scan velocity before and after treatment with EGCg.

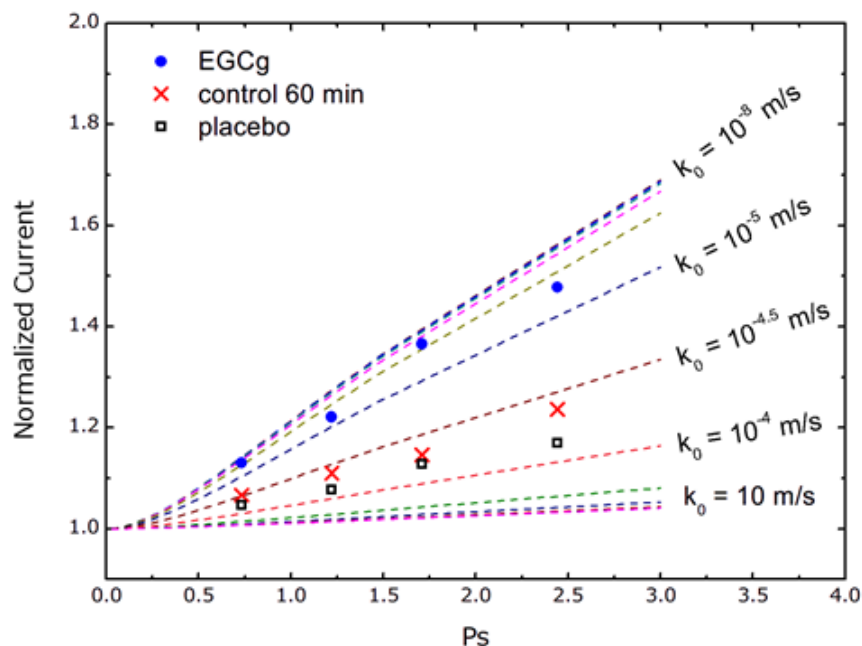


Figure 5.2: Results summary of the three experimental sample groups: control (before treatment), placebo (treated with DMEM-), and EGCg treated sample. The dashed lines represent the simulated normalized peak currents for several substrate kinetics ranging from 10^{-8} to 10^1 m/s. The probe is positioned at $12\mu\text{m}$ above the samples

In our previous work, we demonstrated that, with the help of numerical modeling, a substrate's electrochemical reaction kinetics can be determined by SECM constant height imaging, based on a forced convection effect, which can be induced by increasing the scan velocity.¹⁸⁵ Prior to EGCg exposure, HeLa cells exhibited an average heterogeneous rate constant of 0.72×10^{-4} m/s. Similarly, cells incubated in DMEM- (placebo) instead of EGCg, show a kinetic rate of 1.02×10^{-4} m/s, demonstrating that there is only a minor effect from continuous starvation at this time. The cells seem to become slightly more active, probably to increase their nutritional intake. In contrast, the heterogeneous rate constant of cells exposed to EGCg strongly decreased to 0.16×10^{-4} m/s, which is indicating a slower metabolic rate of these cells. These results suggest that these cancer

cells actively reduce their metabolism in the presence of GTC. It is thought to act as a defense mechanism against harmful substances, which cannot be metabolized and hence cause cell death when entering the cell at a high concentration. This result is in good agreement with the literature, where EGCg as well as ECg was shown to reduce metabolic activity, which is required to maintain cancer cell proliferation and metastasis in colon cancer¹⁸⁹ and breast cancer.¹⁹⁰ As EGCg was removed, the cells seem to recover from the induced stress by the GTC, as the rate constant increases over time back to its initial value of 0.72×10^{-4} m/s. This effect was anticipated, as no significant morphological changes were observed during the 1 h exposure to EGCg, indicating that no irreversible initiation of apoptosis or necrosis occurred at this time and concentration.

Time Dependent Reaction Cascade and Cellular GSH Regulation Following EGCg Exposure. To confirm GSH regulation by the cell as a response to EGCg, fluorescence microscopy studies were conducted. Interestingly, cells seem to respond to the catechin treatment notably around 30 min as the error bars increase (Figure 5.3A). A significant higher GSH content was observed after 60 min of exposure to EGCg, whereas a significantly lower GSH amount was found after 90 min of treatment. Improvement of GSH levels and activity after EGCg administration is reported in literature and is said to be responsible for an enhanced glutathione peroxidase (GP) activity, antioxidant status, and glutathione redox system of the organism.^{191,192} Glutathione and its regulative mechanisms protect organisms from oxidative damage, and GTCs are known to induce the production of GP, catalase, and glutathione-s-transferase.^{193,194} As GSSG is converted to GSH by the glutathione reductase (GR), NADPH is deprotonated.¹⁹⁵ Furthermore, by converting GSH back to GSSG, harmful substances, such as H₂O₂, can be reduced to H₂O.¹⁹⁶ As summarized in Figure 5.3B, our studies suggest that, following the EGCg exposure, it takes about 30 min for GR to take effect (Figure 5.3A). As a result, the intracellular GSH content increases, which can be

seen in SECM constant height line scan measurements after 60 min of incubation (Figure 5.1). In order to cope with EGCg, the GP comes into force. However, if the concentration of EGCg is too high or the time of exposure is prolonged, the cell is unable to cope with EGCg and irreversible cell death cascades are activated and GSH decreases.

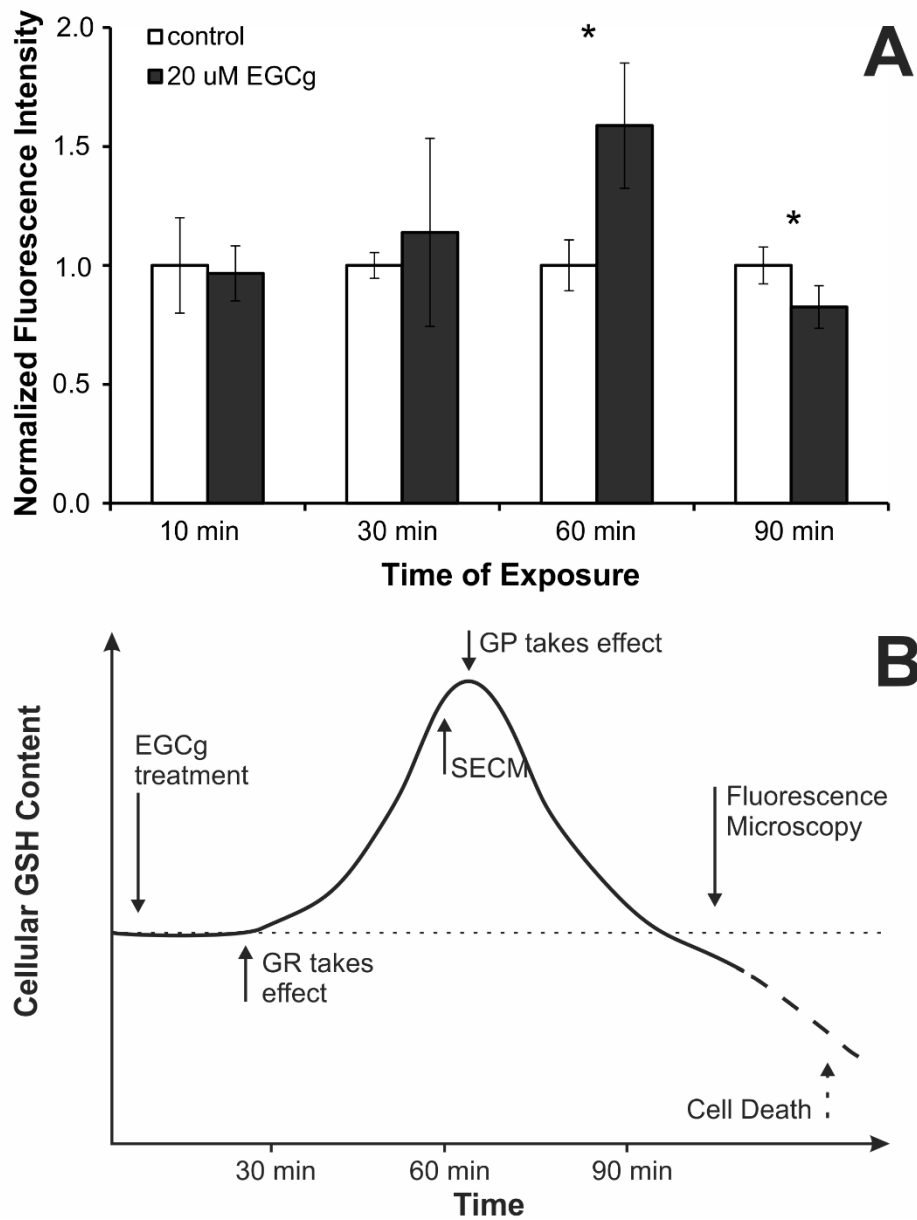


Figure 5.3: (A) Time dependent CMFDA response depending on intracellular GSH content. (B) Proposed time dependent reaction scheme for EGCg effect leading to alterations of intracellular GSH content and, eventually, cell death.

5.5 Conclusion

In conclusion, we demonstrate that SECM constant height line scan imaging can be used to simultaneously observe the cell redox environment, which is determined by alterations in the GSH/GSSG ratio, and reaction kinetics in single human cancer cells. Thereby, the heterogeneous reaction rate of the redox mediator at the microelectrode tip is quantitatively determined and depends on the regeneration reaction of the redox species by the cell. It is shown that not only prolonged exposure to EGCg leads to irreversible cell death but also short time exposure leads to an increase of cellular GSH. Additionally, using numerical modeling based on the forced convection effect, a reduction in metabolic activity of the cell was revealed. The reliable and simultaneous determination of cell reaction kinetics as well as the GSH mechanism is achieved in the presented SECM studies and displays the potential of this technique to further investigate mechanisms involved during inhibition of carcinogenesis.

5.6 Acknowledgements

The authors acknowledge the Natural Sciences and Engineering Research Council of Canada (NSERC) for its financial support. Technical assistance of Ivon Vassileva and Laurence Danis is also acknowledged.

CHAPTER VI

SUMMARY AND CONCLUSIONS

The previous chapters presented two strategies to measure a live cell's metabolic rate kinetics non-invasively. In the following, the introduced methods will be directly compared and discussed. To a deeper understanding of the experimental results, attention will be given to the experimental conditions and requirements, in order to directly compare both solutions. Quantitative SECM analyses have been studied in the past and are reported in literature. The following chapter also gives an overview of the reported methodologies and evaluate their advantages and disadvantages compared to the strategies presented in this dissertation.

6.1 Summary of Objective Achievements

Investigation of biological cells on the molecular level are commonly based on techniques, which are invasive, meaning that tested cells will not be able to survive the experimental analysis. Furthermore, most methods require a high number of cells, in order to reach a substance concentration that is above a detection limit. SECM monitors single electron transfers locally, and thereby requires no dilution. The first objective for this PhD work was to establish a cell patterning method that allows SECM measurements on single living cells and to develop and adapt this patterning method for cell co-cultures. As presented in chapter II, successful cell patterns were

achieved in different sizes ranging from 500 μm to as small as 50 μm , using an elastomeric through-hole membrane placed on a polymer slide before or after treatment with oxygen plasma. Both, HeLa as well as HeLa-R cells, were efficiently patterned in cell islands or single cells. The addition of the well-known polymer membrane PDMS allows the application of this method for co-culturing. Multiple cells lines can now be studied at the same time and under the exact same conditions, such as microelectrode parameters, temperature or incubation time.

Being able to position target cells in defined areas on a plastic substrate, enabled us to measure and quantify the efflux of GSH from a single cell, in order to establish a reliable method for the investigation of cancer cells in the Mauzeroll laboratory. To achieve this second objective, HeLa and HeLa-R cells were patterned in small groups in close proximity to each other. SECM 3D imaging in constant height based on two independent redox mediators was employed to record the GSH efflux of both cell lines. As HeLa-R cells are overexpressing MRP1, the presence of additional membrane pumps was expected to result in a significant difference to the efflux from HeLa cells. This expectation was confirmed when SECM data was treated and analysed in Matlab to extract the heterogeneous rate constant for both cell lines, whereby HeLa-R cells showed a 2.4 times greater activity than HeLa cells. This approach represents the first method to determine cells' kinetic rate by SECM.

Although the established technique for the extraction of cellular kinetics based on the use of different redox mediators displays a promising method, non-ideal experimental conditions, such as possible variations in solution temperature and salt concentration and long term starvation of cells, had to be addressed. Such issues are mainly associated with an extensive analysis time during SECM imaging. The reduction of acquisition time could be achieved by increasing the scan velocity of the microelectrode. As a third objective, the investigation of the scan velocity during

SECM measurements lead to the discovery of a forced convection effect that can be used for the determination of the electrochemical signal without the influence of forced convection and furthermore the extraction of cell kinetics employing numerical simulations. This SECM convection method reduces the experimental analysis time by a factor of 10 to 15. The reduction of acquisition time, lets us control the experimental set up and conditions in a much more precise manner, as changes in solution temperature and salt concentration become less likely.

As a fourth and final objective, the SECM convection method had to be tested on a model system, as it is presented in chapter V. We chose to expose HeLa cells to EGCg, a green tea catechin, to monitor the cellular electrochemical response over time. We found a change in metabolism upon EGCg exposure, more specific, a decrease in metabolic activity, compared to a control group, which was exposed to a placebo. This decrease is thought to be a protective measure of the cell, protecting itself from the uptake of the threatening substance. Overall, these results show the usefulness of the established determination method for apparent cellular heterogeneous kinetics.

6.2 Comparison of the Presented Methodologies for Cell Kinetic Determination

Chapter II presents the determination and quantification of cell kinetics based on SECM imaging employing two independent redox mediators. Cell mobility is controlled by patterning target cell in a defined manner on a plastic substrate. This patterning technique allows cells to establish their ordinary physical shape after attachment, but are limited to a 50 by 50 μm area, hence cell “crawling” is successfully avoided. This is particularly useful, as the redox mediator based method requires an SECM imaging time of about 2 to 3 hours. Cell proliferation is usually not an issue when working with HeLa or HeLa-R cells, as their cell cycle permits a cell division

approximately every 6 hours. However, 2 to 3 hours of experimental analysis is sufficient to significantly alter the position and location of potential target cells. As the experimental part of the SECM convection method takes only about 10 min to obtain the data required for kinetic parameter extraction, cell movement is usually not an issue. However, when a target cell is studied for a prolonged period of time, the cell position as well as the alignment with the electrode must be verified and if necessary controlled by cell patterning or adjusted by using the SECM integrated microscope.

Both, the redox mediator based technique as well as the SECM convection method, allow the analysis of single cells. However, with the former, it is not recommended to image target cells more than once, due to the relatively long analysis time that could impact cell metabolism due to starvation and temperature change inside the petri dish. Using the SECM convection method, cells can be analysed multiple times over a period of at least one hour, or even longer if a temperature control station is accessible. Hence, the time dependent effect of substances, such as chemopreventive products as presented in chapter V by the means of EGCg, extracted from green tea, can be investigated. Furthermore, this approach offers great consistency and reproducibility, also related to the short experimental time interval and also due to the fact that solutions don't need to be exchanged as often.

Overall, the SECM convection method displays a fast and convenient way for single cell SECM analysis for the determination of cellular metabolic kinetics. Due to its quick data collection and high reproducibility, it offers important advantages over the redox mediator based method and would be the technique of choice in future SECM cell metabolism measurements.

6.3 SECM Studies on Biological Samples

Glutathione is one cell component that can be probed by SECM, but other means of SECM imaging and investigation of biological samples have also been conducted. Application of SECM to biological samples emerged in the 1990s.¹⁹⁷ Although biological SECM studies have been carried out mostly on Eukaryotes, some bacterial organisms have also been investigated. Thereby interest has grown by either their pathogen nature, as in the case of *Staphylococcus aureus*¹⁹⁸ and *Salmonella typhimurium*¹⁹⁹, or their rather simple grow conditions and metabolic products make them ideal for testing new analytical techniques, as for example *Rhodobacter sphaeroides*²⁰⁰ and *Paracoccus denitrificans*.²⁰¹ The most commonly studied bacteria by SECM is the gram-negative purple sulfur bacteria *Escherichia coli*. Among others, also experiments on the interaction of redox mediators, such as ferricyanide and ferrocyanide couple with the bacteria have been performed.^{202,203} In 2004 Bard and co-workers investigated the MRP1-mediated efflux of thiodione from yeast and hepatoblastoma cells, showing it is possible to estimate the export rate of thiodione by SECM.^{108,109}

Overall, a variety of Eukaryotes has been investigated, at which studies focused on multiple cells, single cells, and even intracellular measurements.^{40,100} The analysis of single human cells began in 1998, when Yasukawa and co-workers investigated the respiration activity in colon cancer cells. The cytotoxic properties of potassium cyanide were confirmed, when the cellular respiration was found to decrease upon potassium cyanide exposure.¹⁰¹ Our model cell type HeLa is one of the most commonly studied cell types by biological SECM. As an example, Takahashi and co-workers recorded levels of secreted alkaline phosphatase and green fluorescent protein using a shear-force-controlled SECM, whereby the green fluorescent protein was recognized by a photomultiplier detector.⁵⁷ In the past two decades the study of biological matter has found

increasing interest in the SECM community and extensive reviews of these publications can be found in literature.^{40,100}

The development of SECM for biological systems is past the first applications, and research focuses now on the development of standardized routine applications, that can be applied in medical and biological research.

6.3.1 Quantitative SECM Studies in Literature

Quantitative analyses of charge transfer kinetics on biologically relevant samples have been conducted on a variety of substrates and interfaces, where SECM studies focused on the recognition of intracellular metabolites.²⁰⁴ All of these are using the substrate generation – tip collection method but applied to different relevant substrates.

A first quantitative study of MRP1 activity was performed by the group of Dr. Allen J. Bard in 2004, quantifying thiodione efflux, and verifying its export through MRP1 using an MRP1 blocker.^{108,109,110} Similarly, Dr. Wenrui Jin and co-workers investigated peroxidase enzyme activity, by providing human neutrophils with H₂O₂ and hydroquinone as enzyme substrates, while measuring the efflux of benzoquinone in line scans across the cell.²⁰⁵ Both studies suffered, however, from one of the major challenges in SECM imaging – the separation of topographic and reactivity contribution to the signal. Changes in cell morphology during the measurements, which affect the diffusion behavior of the observed substances, have not been taken into account. The latter study furthermore exposed the cells to invasive treatments, particularly ultramicroinjection of the substrate solutions. This brings into question whether the thus measured enzyme activity is representative of its activity in an undisturbed environment.

Of impact to the investigation of trans-membrane transport in living cells should also have been a study from 2012 investigating passive diffusion through a nano-porous silicon membrane with nanoelectrode SECM.²⁰⁶ The application of the presented methodology to biological cells has not yet been published and may be difficult, given that the authors performed constant height measurements at 1.3nm distance, whereas the ruggedness of cells would require a constant-distance approach.^{207,208}

What crystallizes from this discussion is the necessity to decouple topographic and reactive signal of a surface. This can be avoided, when using constant distance SECM. Shear force SECM is one of the most developed constant distance techniques. The principle of the constant distance mode, based on shear force has already been introduced in chapter I (section 1.3.4.3) and the application for biological cell studies has been reviewed in literature.²⁰⁹ However, aside from the fact that the shear force based SECM set up remains expensive and complicated, requiring a skilled and devoted operator with interdisciplinary knowledge, the cause of the shear force effect is still not fully understood.⁵⁵ It is possible that a physical contact between electrode and substrate is required, which could lead to cell damage. Even if no physical contact is required for creating a shear force zone, a vibrating microelectrode at a nanometer scale distance from the cell surface might cause morphological and metabolic alterations of the target cell.

Alternating Current-SECM (AC-SECM) has also been suggested to be able to maintain a constant substrate-tip separation.⁴⁹ The constant distance control is achieved by applying an alternating rather than constant potential at the WE. An internal oscillator of a lock-in amplifier is thereby sending a sinusoidal wave function to the potentiostat. The current that is measured, alternates naturally at the same frequency, but with a phase shift. Current amplitude and phase shift together are measured as a complex impedance. As this impedance signal is dependent on the

tip-to-sample distance, it can be and has been used for topographical measurements²⁰⁷, SECM tip positioning^{210,211} and kinetic measurements.^{50,212–214} Studies on living cells involve topographical studies on neurons²¹⁵ and oxygen consumption studies on pancreatic insulin-secreting cells²¹⁶. In 2005, Baur and co-workers, however, pointed out a major disadvantage of the AC-SECM technique during live cell studies. The local concentration of ionic species (ionic strength) influences the measured impedance. Since the concentration of ionic species varies across a cell surface and over time, the concentration dependent and distance dependent impedance changes are convoluted and interfere with the maintenance of constant distance.²¹⁵ Nevertheless, Ding and co-workers investigated topography and metabolic cellular activity in monkey kidney (cos-7) cells in 2007.⁵¹ Thereby information about topography and cellular metabolic activity were obtained using an AFM-AC-SECM and could not be obtained simultaneously.

It becomes clear that topographic and reactive decoupling is difficult with constant distance mode for biological samples. As such, the presented method to reduce the impact of topography on the extracted kinetic rates is a significant step forward towards quantification of kinetic parameters from biological samples. While the presented strategy requires scans over a single topographical feature, it should improve accuracy, reproducibility and comparability of the quantified parameters, and enable observation of the time-dependent reaction of cells towards external stimuli, as presented in chapter V.

6.4 Potential Future Studies

Suggestions for future studies, presented in the following, are oriented in three directions: (A) The application of the presented method (chapter IV and V) to alternative cell lines, (B) the possible further development and improvement of the presented SECM convection method and

(C) a suggestion for future work combining SECM and AFM to further investigate multidrug resistance.

6.4.1 Effect of GTC on Other Cell Lines

The influence of GTC on MRP1 overexpressing cells, such as HeLa-R can be studied. Yang and co-workers investigated the cellular uptake and biotransformation of EGCg in HT-29 Human Colon Adenocarcinoma Cells.¹⁹³ In this study, multidrug resistant proteins were inhibited by the cell exposure to indomethacin and probenecid, which lead to an accumulation of EGCg in HT-29 cells. Interestingly, Pgp inhibitors had no effect on intracellular EGCg accumulation. These results suggests that a link exists between MRPs and EGCg export from cells, hence it is expected that a much higher concentration of EGCg has to be chosen in order to achieve similar effects of EGCg as presented in chapter V. Also, the time dependent response of HeLa-R cells might differ from what was seen in HeLa cells.

Furthermore, more impactful cell lines could be chosen, such as lung cancer or brain tumor cells, to investigate the impact of GTC on different carcinogenetic tissues.

6.4.2 Further Development of the SECM Convection Method

The determination method for the GSH efflux from living cells as presented in chapter IV and V is based on the assumption that a HeLa cell exhibits a hemispherical shape close to that of a deposited mercury drop as mentioned in the results and discussion section of chapter IV. Thereby the impact of a change in topography was defined as a change in height, rather than a change in the overall shape of the cell. The kinetic value k_0 , obtained by SECM convection method was

found to be independent from topographical alterations. It could be interesting to see whether the shape of the cell has an impact on k_0 . This information could be achieved by numerical simulations based on the convection method presented, carried out on different theoretical cell geometries. In the same way, it could be investigated if a kinetic determination across a homogeneously rough surface, such as a cell monolayer, could be obtained. This is useful, because a kinetic map, as extracted in chapter II could be established over an area containing multiple cells of either same or different nature.

Furthermore, it could be explored whether the determined k_0 value and the measured electrochemical current at the slowest scan speed could be used to extract a living cells height. Therefore, k_0 could be introduced into the established analytical approximation for the current without convection effect. This value can be extrapolated from the linear behavior of the normalized peak current as a function of velocity, as presented in chapter III (Figure 6.1A). As the normalized peak current depends on the dimensionless radius of glass of the microelectrode (R_G), the normalized distance (L) and the kinetic of the substrate (k_0), L can be extracted from the analytical approximation used in chapter II (equation (A.1)). When the microelectrode is positioned above a target cell, the height of a cell (d_{CS}) could then be determined easily by subtracting the tip-to-cell distance (d_{TC}) from the known tip-to-substrate distance (d), as shown in figure 6.1. Such an approach would allow the determination of cell height and monitoring over time on the nanometer scale, which could be confirmed by AFM measurements.

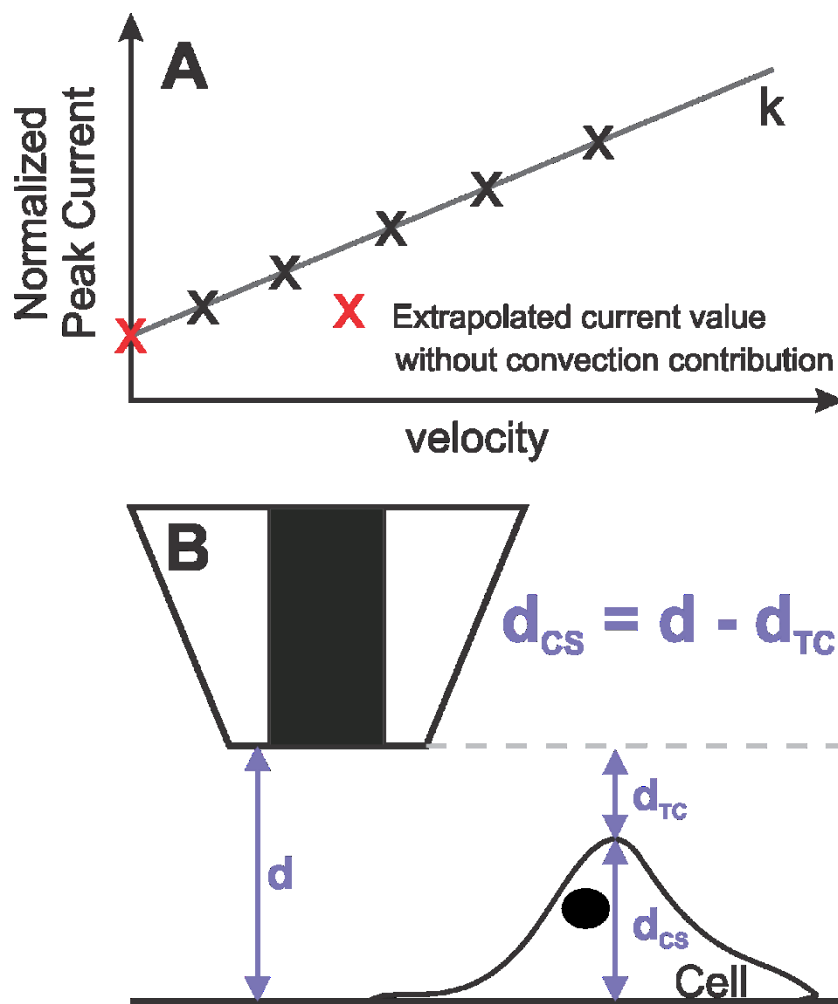


Figure 6.1: Schematic representation of cell height determination by means of the SECM convection method. (A) Extrapolation of the current value without contribution of convection. (B) Calculation of cell height (d_{CS}) from tip-to-substrate distance (d) after obtaining the tip-to-cell distance (d_{TC}) by numerical simulations.

6.4.3 MRP1 Distribution in HeLa and HeLa-R

To investigate the phenomenon of multidrug resistance further, the distribution of MRP1 pumps on the cell membrane can be determined. The MRP1 expression could thereby not only be investigated by the technique of western plotting⁸⁷, but also be visualized by microscopy

techniques, such as Scanning Electron Microscopy (SEM), Transmission Electron Microscopy (TEM) or Atomic Force Microscopy (AFM).

To recognize MRP1 pumps on the cell membrane, functionalized gold nanoparticles (Au-NPs) can be synthesized. Therefore, 10 nm nanoparticles seem suitable, as they will be small enough to allow a sufficient resolution between membrane pumps, but also large enough to be identified in the above mentioned microscopy approaches. The functionalization of Au-NPs can be achieved in four steps: A) The coupling of biotinylated thiols to the Au-NPs, B) the blockage of unspecific binding sites by bovine serum albumin, C) the linkage of neutravidin to the biotinylated Au-NPs and finally, D) the attachment of a specific antibody, which binds to an extracellular recognition sequence of MRP1, as shown in figure 6.2. After attachment of the Au-NPs, cells can be fixed following established protocols in literature.^{217,218} SEM and TEM will give high resolution images of the distribution of MRP1 pumps. Not only would it be interesting to compare HeLa and HeLa-R cells and to compare the results to the results obtained by SECM, which were presented in chapter II and IV, but also to see if MRP1 pumps are distributed equally across the cell membrane.

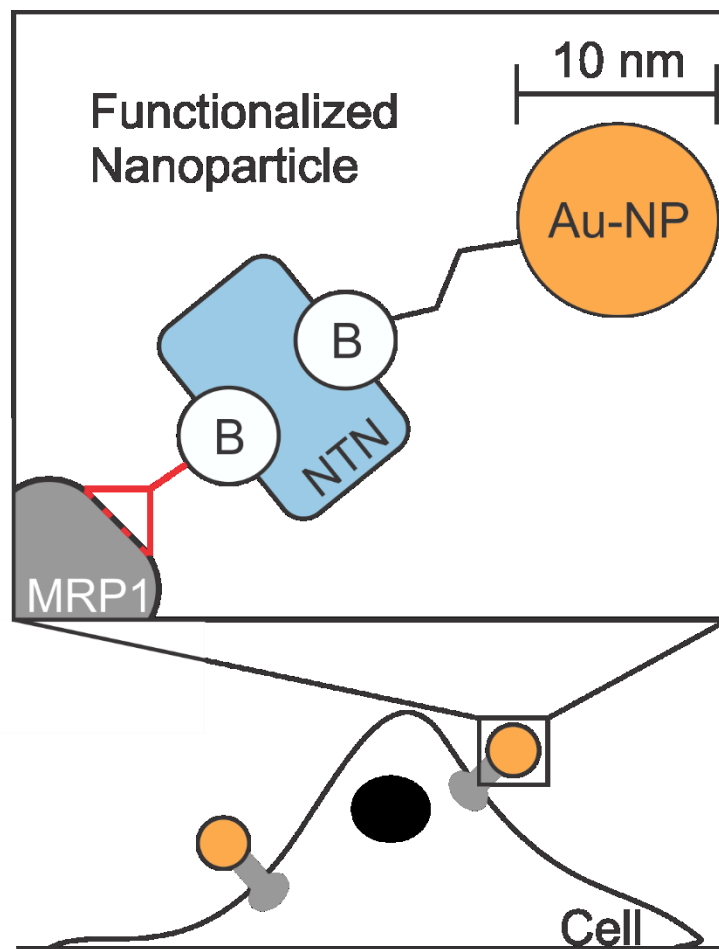


Figure 6.2: Schematic representation of MRP1 pump recognition using functionalized Au-NP. MRP1 can be recognized by a specific antibody (red), binding to a specific sequence (red dotted line). Its biotinylation (B) allows linkage to neutravidin (NTN), which is tied to a biotinylated 10 nm Au-NP.

Furthermore, it is thinkable to combine SECM and AFM as presented in literature⁴⁴, to increase spatial resolution from the μm to the nm scale and build on a more established technique to determine substrate topography. As a result, information about the activity of single membrane pumps expressed on the cell surface may become available. As an example, HeLa-R cells might exhibit a 50 % increase of MRP1 membrane pumps, but not all of these pumps may be active at the same time. While a functionalized AFM tip recognizes MRP1 pumps, the associated GSH

efflux from single MRP1 pumps could be measured by an integrated SECM nanoelectrode.²¹⁹ However, the quantitative evaluation of the current signal needs thereby be established, as diffusive and convective fluxes of a redox species towards the sensor become more complex, due to the geometry of the AFM tip.

Using the established cell patterning method, presented in chapter 2, histochemical cross talk between cells may be studied. During the development of the proposed cell patterning procedure, it was observed that HeLa cells, positioned in different cell islands, started to grow towards each other and trying to bridge spaces between the oxygen plasma treated islands, if the incubation time exceeded 48 h at 37 °C and 5 % CO₂. Such cell signalling actions could be investigated by SECM imaging and fluorescent labelling of transmitter molecules, such as pheromones. Another approach could be to position HeLa cells in close proximity to HeLa-R cells, in order to observe the electrochemical signal of both cell types over time. A mild stimulation with a stress inducer could be performed to initially observe a difference in electrochemical current measured above these target cells, which might change over time due to histochemical cross talk between HeLa and HeLa-R.

APPENDIX A

SUPPORTING INFORMATION TO CHAPTER II “ASSESSMENT OF MULTIDRUG RESISTANCE ON CELL COCULTURE PATTERNS USING SCANNING ELECTROCHEMICAL MICROSCOPY”

A.1 Cell Management

Cells were cultured according to published procedures⁸⁷. Staining of cells was performed using a PKH2 (green) or a PKH26 (red) Fluorescent Cell Linker Kit (SigmaAldrich). These fluorescent markers label the cell membrane by incorporation into the lipid region of the biphospholipid layers²²⁰. Cells were harvested with a 0.25% (vol/vol) Trypsin-EDTA solution (10×, 2.0 g EDTA, in 0.9 wt% NaCl) at 37 °C. Next, 2×10^7 cells were transferred into a 15 mL Falcon tube (Sarstedt) and washed once with basic medium without serum (DMEM–). Cells were centrifuged at 400 g for 5 min, followed by removal of the supernatant. The cells were then resuspended in 1 mL of Diluent C (supplied with the Cell Linker Kit), and added to 1 mL PKH2 or PKH26 dye (4 μM). The suspension was incubated at 25 °C for 4 min, during which the tube was frequently inverted to assure homogeneous mixing. The staining reaction was stopped by adding 2 mL 1 % BSA solution. The cell suspension was diluted by adding 4 mL DMEM+ and centrifuged at 400 g for 10 min to separate cells from the staining solution. The supernatant was removed and cells were transferred into a new 15 mL Falcon tube (BD Biosciences). Three washes were performed using 8 mL DMEM+ each and centrifugation at 400 g for 10 min. Cells were resuspended and the suspension was used in appropriate dilutions during the cell patterning procedure.

A.2 Preparation of Plastic Substrates

Zeonor slides (25×75 mm² in area, 1 mm in thickness) were prepared by injection molding using a Boy 30A injection tool (Dr. Boy GmbH). Zeonor 1060R (Zeon Chemicals) was molded at a temperature of 250–260 °C, an injection speed of 40 mm·s⁻¹, and a pressure of 132 bar. The mold (stainless steel, custom-fabricated) was cooled for 15 s before the slide was released. Disks (23 mm in diameter) were obtained by punching Zeonor slides manually, followed by washing with methanol, ethanol, and deionized water (18.2 MΩcm), respectively, to remove monomers or residual plasticizing agents from the surface. Cell culture substrates were exposed to oxygen plasma (Plasmalab80Plus, Oxford Instruments) at a pressure of 0.067 mbar and a power/gas flow ratio of 40 W·sccm⁻¹ for 4 min¹¹⁵.

A.3 Fabrication of Membranes and Cover Slabs

Elastomeric throughhole membranes were fabricated from Versaflex CL30 (GLS Corp.) using hot embossing lithography (HEL). The mold was prepared by photolithography using SU-8 (GM1040, Gersteltec) on a 4 inch silicon wafer (Silicon Quest International, Inc.). The wafer was first baked on a hot plate at 200 °C for 10 min; SU-8 resist was applied through spin-coating, which was followed by a prebake at 65 and 95 °C for 5 and 15 min, respectively, using a temperature ramp of 2 °C·min⁻¹. Resist was exposed to UV light with a wavelength of 365 nm (Hg i-line) at 280 μJ·cm⁻² through a high-resolution transparency photomask (FineLineImaging) using a 6200 mask aligner (EV Group). Post exposure bake was done using the same conditions as for the prebake. Resist features were developed in propylene glycol monomethyl ether acetate (PGMEA; Sigma-Aldrich) for 2 min; the wafer was rinsed with PGMEA and isopropanol (Anachemia) and dried with a stream of nitrogen gas. The resultant resist pattern was hard-baked at 130 °C for 2 h. Finally, the master was coated with a thin, anti-adhesive layer formed from 1H,1H,2H,2H-

perfluorooctyl-trichlorosilane (Sigma-Aldrich) using deposition from the vapor phase under reduced pressure. Versaflex CL30 was received in the form of pellets; the material was extruded at 165 °C to yield a film of 150 µm thickness. For the fabrication of the open through-hole membranes, a circular piece (4 inches in diameter) was cut from the extruded sheet and placed between the mold and an unstructured counter plate. The counter plate consisted of a silicon wafer coated with a thin (20–100 µm) layer of poly(dimethylsiloxane) (PDMS, Sylgard 184; Dow Corning) deposited by spin-coating a degassed prepolymer mixture (elastomer base/curing agent=10/1, wt/wt) followed by curing at 200 °C for 2 h. HEL was performed using an EVG 520 embossing tool (EV Group) operated at 160 °C, an applied force of 1×10^4 N, and a pressure of 1×10^{-3} mbar. All fabrication steps were carried out in a clean room environment (class 1000). Planar PDMS slabs were prepared from Sylgard 184 (Dow Corning) by curing the mixed prepolymers of PDMS (elastomer base/curing agent=10/1, wt/wt) on a flat polystyrene surface (Corning, Petri dish; Sigma-Aldrich) in an oven at 60 °C for 12 h.

A.4 Imaging

Cell patterns were inspected using a Nikon Eclipse TS100 inverted microscope (Nikon) equipped with an Olympus CAMEDIA C-500 ZOOM digital camera (Olympus Canada). Fluorescence images were acquired using a Nikon TE-300 confocal microscope. Scanning electron micrographs were recorded using an S-4800 scanning electron microscope (Hitachi) operated at an acceleration voltage of 2.0 kV. The membrane was coated with a thin layer of Pt using electron-beam deposition to facilitate imaging.

A.5 Data Analysis

The specific contributions to the total measured microelectrode current (Eq.3) have been previously described by ¹³⁴ where L is the normalized distance defined as the ratio of the tip-to-

substrate distance and the radius of the metal wire of the electrode, Ni_s is kinetically controlled substrate current, Ni_T^{cond} is normalized current over a conductor, D is the diffusion coefficient of the redox mediator ferrocenemethanol ($FcCH_2OH$) ($D=7.8 \times 10^{-6} \text{ cm}^2 \cdot \text{s}^{-1}$), d is the tip-to-substrate distance, and k_f is the apparent heterogeneous rate constant.

$$Ni_s = \frac{0.78377}{L + \frac{1}{\Lambda}} + \frac{0.3315 * \exp\left(-\frac{1.0672}{L}\right) + 0.68}{1 + \left[\frac{\left(\frac{11}{\Lambda L}\right) + 7.3}{110 - 40L}\right]} \quad [\text{A.1}]$$

$$Ni_T^{cond} = \frac{0.78377}{L} + 0.3315 * \exp\left(-\frac{1.0672}{L}\right) + 0.68 \quad [\text{A.2}]$$

$$\Lambda = \frac{k_f * d}{D} \quad [\text{A.3}]$$

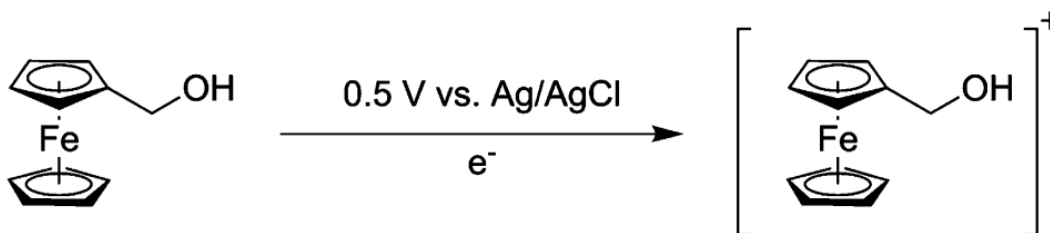


Figure A.1. Oxidation of $FcCH_2OH$ to $[FcCH_2OH]^+$.

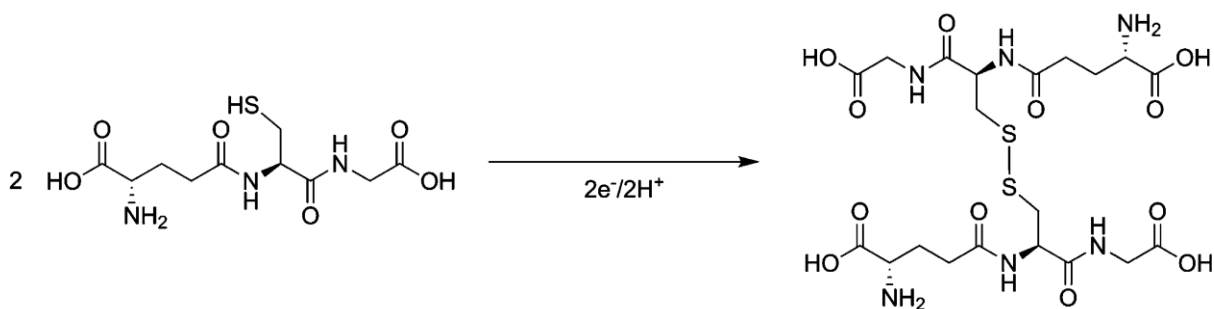


Figure A.2. Formation of glutathione disulfide through intermolecular coupling of glutathione.

APPENDIX B

SUPPORTING INFORMATION TO CHAPTER III “FORCED CONVECTION DURING SCANNING ELECTROCHEMICAL MICROSCOPY IMAGING OVER LIVING CELLS: EFFECT OF TOPOGRAPHIES AND KINETICS ON THE MICROELECTRODE CURRENT”

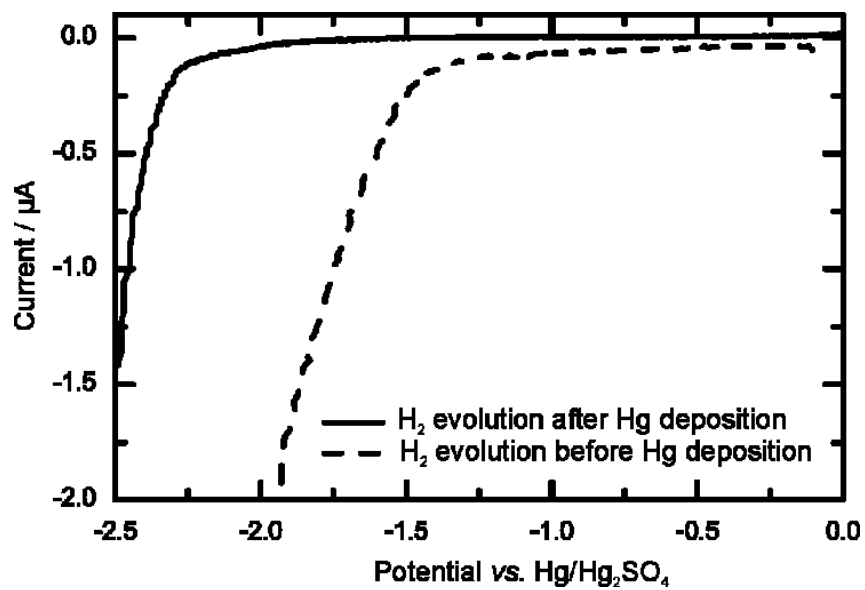


Figure B.1. The hydrogen evolution potential increases upon mercury deposition on the platinum electrode.

APPENDIX C

SUPPORTING INFORMATION TO CHAPTER IV “HIGH-SPEED SCANNING ELECTROCHEMICAL MICROSCOPY METHOD FOR SUBSTRATE KINETIC DETERMINATION: METHOD AND THEORY”

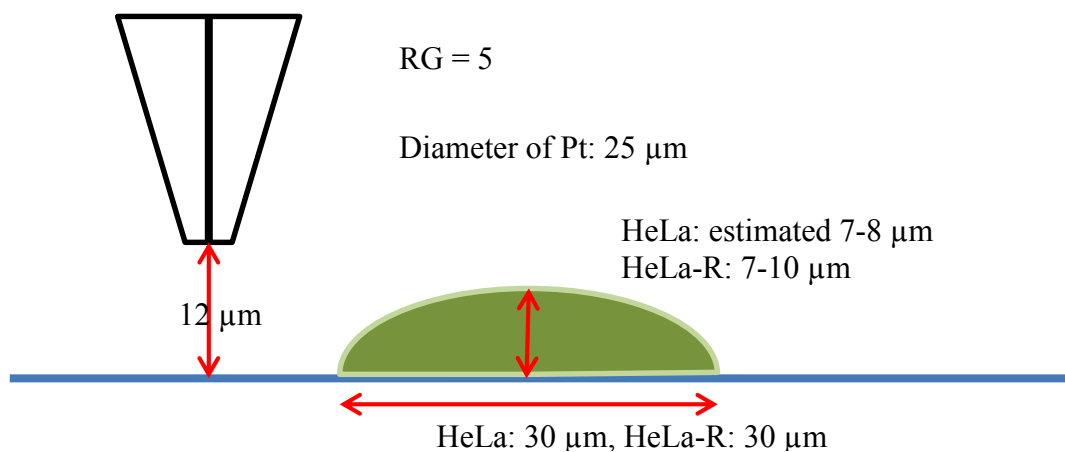


Figure C.1. Schematic representation of experimental setup and parameters for numerical simulations.

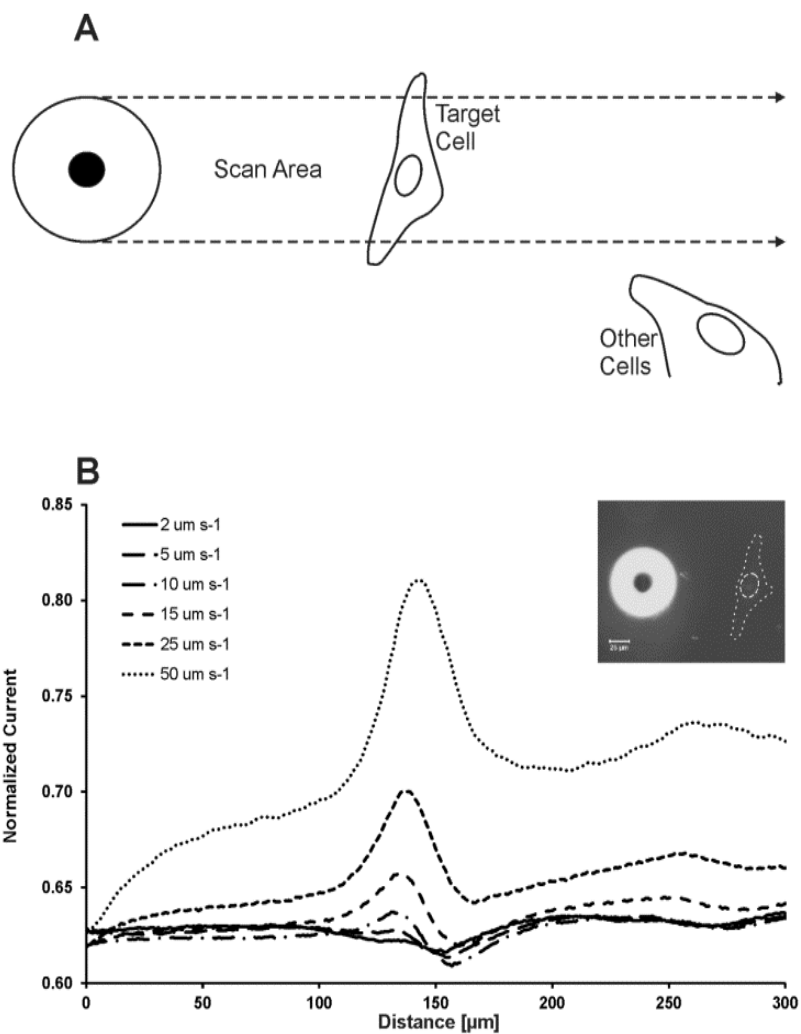


Figure C.2. SECM imaging of a single living HeLa cell. (A) Schematic representation of experimental procedure. The microelectrode is positioned 12 μm above the substrate and about 100 μm to the left of a target cell. The biased tip scans across the center of the cell at velocities ranging from 2 to 50 $\mu\text{m/s}$.

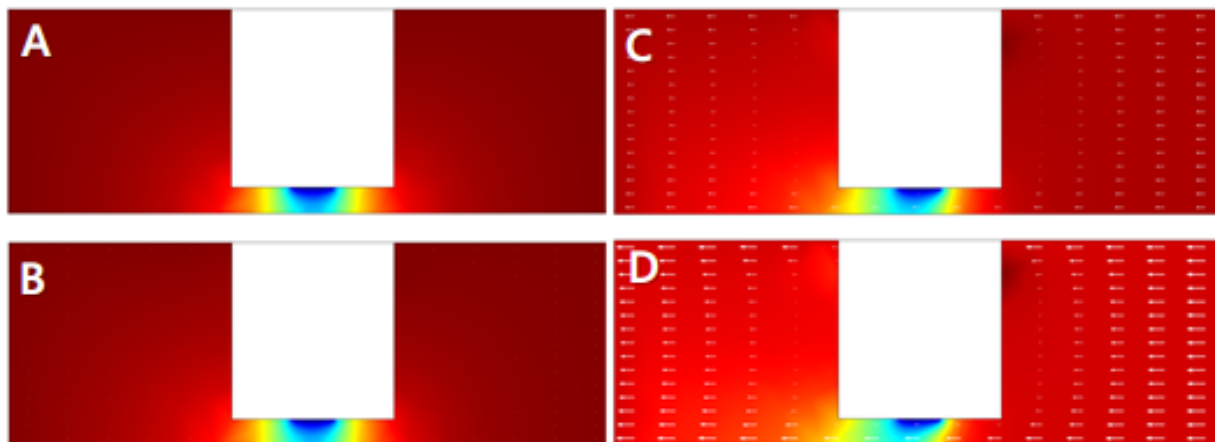


Figure C.3. Scan direction and fluid movement during SECM scan. The microelectrode (white) is scanned from left to right at (A) 0 $\mu\text{m/s}$, (B) 2 $\mu\text{m/s}$, (C) 10 $\mu\text{m/s}$ and (D) 20 $\mu\text{m/s}$, which causes a fluid flow from right to left.

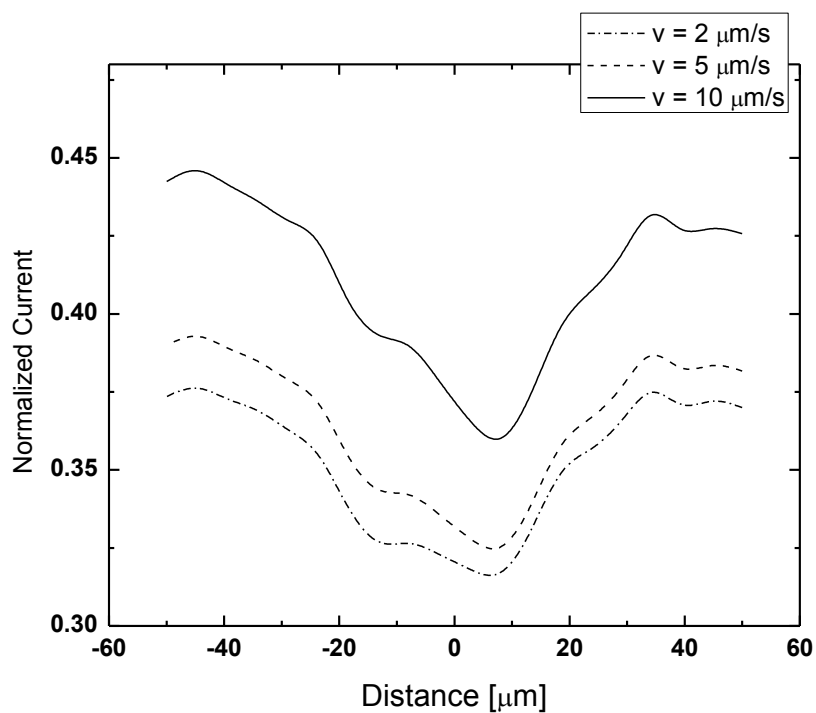


Figure C.4. Numerical simulations of an SECM scan across a domed substrate at velocities ranging from 2 to 10 μm . Simulation parameters: initial tip-to-substrate distance is 12 μm , mediator is 1mM ferrocyanide, 25 μm Pt microelectrode with $\text{RG}=5$.

APPENDIX D

SUPPORTING INFORMATION TO CHAPTER V “HIGH-SPEED SCANNING
ELECTROCHEMICAL MICROSCOPY METHOD FOR SUBSTRATE KINETIC
DETERMINATION: APPLICATION TO LIVE CELL IMAGING IN HUMAN CANCER”

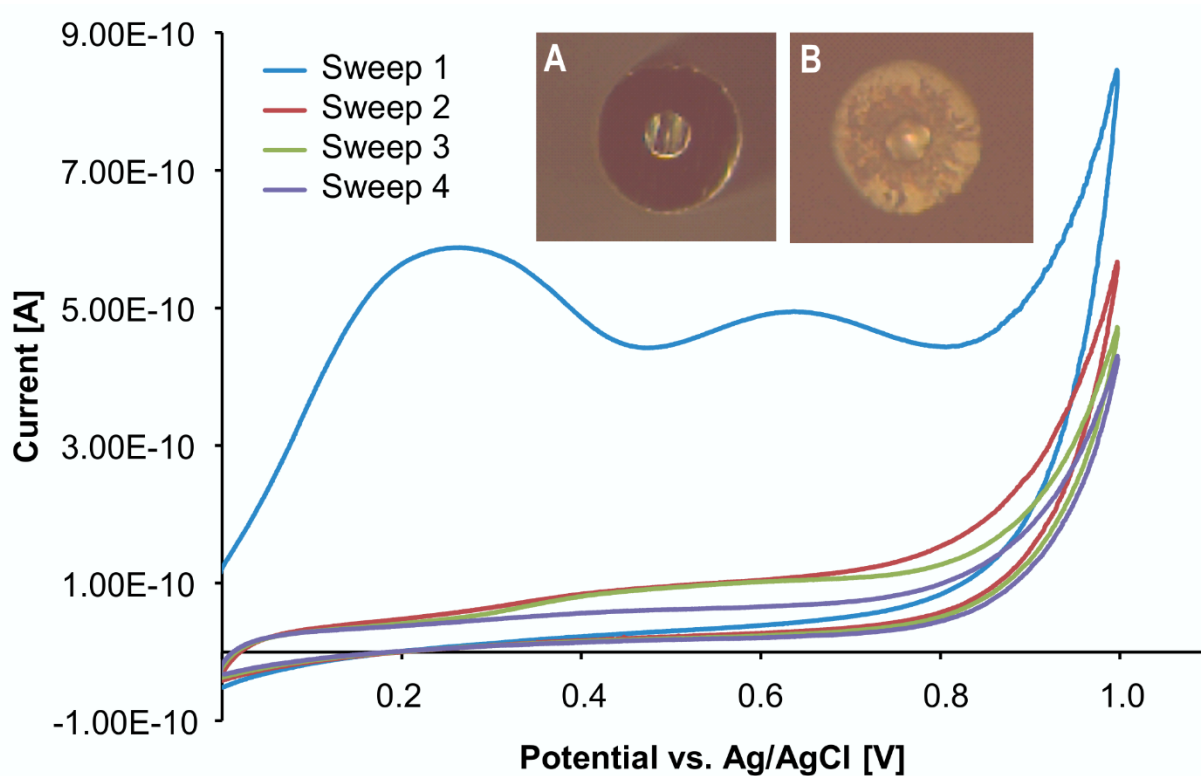


Figure D.1. (A) Cyclic Voltammogram of 1 mM EGCg in PBS. An irreversible two electron transfer reaction is obvious during the oxidation of EGCg. Due to electrode blockage by the oxidation product of EGCg, the electrochemical signal diminishes after one initial sweep. Insets showing optical micrographs of the electrode before (A) and after (B) 21 sweeps in 1 mM EGCg solution.

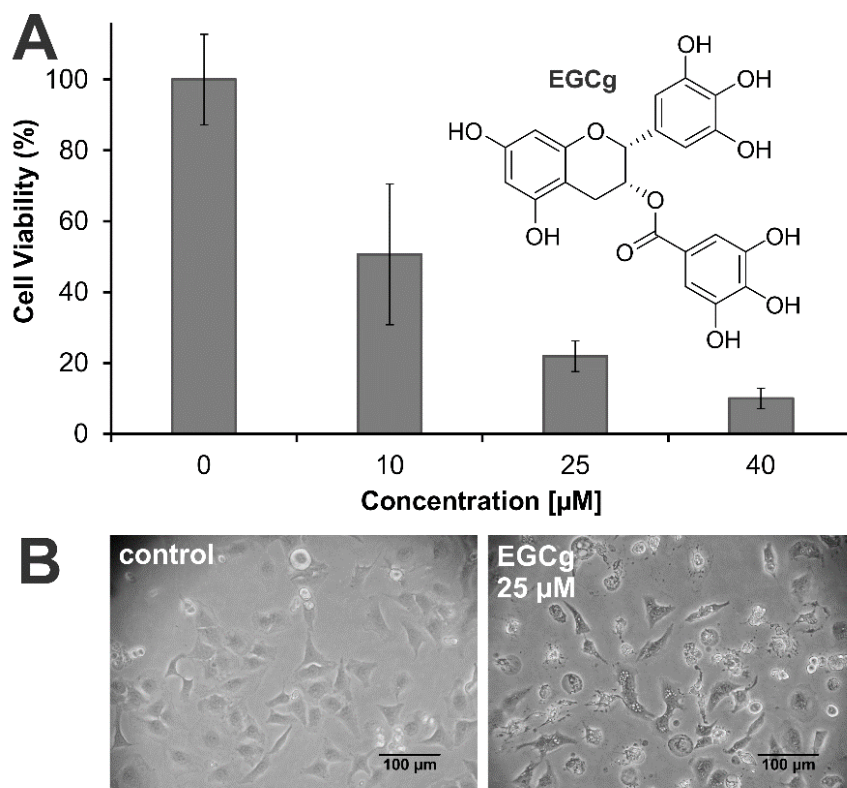


Figure D.2. (A) Cell viability depending on EGCg concentration over a period of 4 hours. (B) Optical micrographs of HeLa cells incubated in DMEM- (left panel) or 25 μM EGCg in DMEM- for 24 hours.

Catechin effect on cell viability. In order to quantitatively evaluate a human cancer cell's metabolic rate under the influence of EGCg, a suitable catechin concentration needed to be identified. A concentration of 25 μM EGCg over an incubation period of one hour was identified from viability studies to impact cell metabolism without leading to immediate cell death. Figure 1A shows, this concentration eventually leads to necrosis in about 75 % of cells after 4 hours of incubation with only small effect variation among cells (small error bars). The long term effect of EGCg on cells' morphology and viability is shown in optical micrographs (Figure 1B), where typical signs of necrosis, e.g. swelling or matter disintegration can be seen in almost all cells after 24 hours of incubation.

REFERENCES

- (1) Schafer, F. Q.; Buettner, G. R. *Free Radic. Biol. Med.* 2001, 30, 1191–1212.
- (2) Li, Y.; Wei, G.; Chen, J. *Appl. Microbiol. Biotechnol.* 2004, 66, 233–242.
- (3) Gilbert, H. F. In *Advances in Enzymology*; Meister, A., Ed.; Wiley Interscience, New York, 1990; Vol. 63, pp. 69–173.
- (4) Smith, C. V.; Jones, D. P.; Guenther, T. M.; Lash, L. H.; Lauterburg, B. H. *Toxicol. Appl. Pharmacol.* 1996, 140, 1–12.
- (5) Griffith, O. W. *Free Radic. Biol. Med.* 1999, 27, 922–935.
- (6) Lu, S. C. *FASEB J.* 1999, 13, 1169–1183.
- (7) Dringen, R. *Prog. Neurobiol.* 2000, 62, 649–671.
- (8) Cotgreave, I. A.; Gerdes, R. G. *Biochem. Biophys. Res. Commun.* 1998, 242, 1–9.
- (9) Lantz, R. C.; Lemus, R.; Lange, R. W.; Karol, M. H. *Toxicol. Sci.* 2001, 60, 348–355.
- (10) Markovic, J.; Borrás, C.; Ortega, A.; Sastre, J.; Vina, J.; Pallardo, F. V. *J. Biol. Chem.* 2007, 282, 20416–20424.
- (11) Meister, A. *Cancer Res.* 1994, 54, 1969–1975.
- (12) Meister, A. *J. Biol. Chem.* 1994, 269, 9397–9400.
- (13) Wang, W.; Ballatori, N. *Pharmacol. Rev.* 1998, 50, 335–356.
- (14) Lu, S. C. *Curr. Top. Cell. Regul.* 2001, 36, 95–116.
- (15) Stenzel, J. D.; Welty, S. E.; Benzick, A. E.; Smith, E. O.; Smith, C. V.; Hansen, T. N. *Free Radic. Biol. Med.* 1993, 14, 531–539.
- (16) Jones, D. P.; Carlson, J. L.; Samiec, P. S.; Sternberg Jr., P.; Mody Jr., V. C.; Reed, R. L.; Brown, L. A. *S. Clin. Chim. Acta* 1998, 275, 175–184.
- (17) Kosower, N. S.; Kosower, E. M. *Int. Rev. Cytol.* 1978, 54, 109–160.
- (18) Chatterjee, S.; Noack, H.; Possel, H.; Keilhoff, G.; Wolf, G. *Glia* 1999, 27, 152–161.
- (19) Griffith, O. W.; Meister, A. *Proc. Natl. Acad. Sci. U. S. A.* 1985, 82, 4668–4672.
- (20) Wahlländer, A.; Soboll, S.; Sies, H.; Ingrid, L.; Monika, M. *FEBS Lett.* 1979, 97, 138–140.

- (21) Bellomo, G.; Vairetti, M.; Stivala, L.; Mirabelli, F.; Richelmi, P.; Orrenius, S. *Proc. Natl. Acad. Sci. U. S. A.* 1992, 89, 4412–4416.
- (22) Soboll, S.; Grundel, S.; Harris, J.; Kolb-Bachofen, V.; Ketterer, B.; Sies, H. *Biochem. J.* 1995, 311, 889–894.
- (23) Mauzeroll, J.; LeSuer, R. J. In *Handbook of Electrochemistry*; Zorski, C. G., Ed.; Elsevier B.V.: Amsterdam, 2007; Vol. 1, pp. 199–211.
- (24) Bagotsky, V. S. In *Fundamentals of Electrochemistry*; Wiley-Interscience, 2006; pp. 590–591.
- (25) Man, R. C.; Ismail, A. F.; Ghazali, N. F.; Fuzi, S. F. Z. M.; Illias, R. M. *Biochem. Eng. J.* 2015, 98, 91–98.
- (26) Kunamneni, A.; Prabhakar, T.; Jyothi, B.; Ellaiah, P. *Enzyme Microb. Technol.* 2007, 40, 1538–1542.
- (27) Lehninger, A.; Nelson, D.; Cox, M. *Lehninger Biochemie*; 3rd editio.; Springer-Verlag Berlin Heidelberg New York, 2001.
- (28) Bronaugh, R. L.; Collier, S. W.; Storm, J. E.; Stewart, R. F. J. *Toxicol. - Cutan. Ocul. Toxicol.* 1989, 8, 453–467.
- (29) Kamisato, J. K.; Nowakowski, M. *Immunopharmacol. (New York)* 1988, 16, 89–96.
- (30) Danis, L.; Polcari, D.; Kwan, A.; Gateman, S. M.; Mauzeroll, J. *Anal. Chem.* 2015, 87, 2565–2569.
- (31) Bard, A. J.; Mirkin, M. V. *Scanning Electrochemical Microscopy*; Second.; Marcel Decker Inc.: USA: New York, 2001.
- (32) Mezour, M. A.; Morin, M.; Mauzeroll, J. *Anal. Chem.* 2011, 83, 2378–2382.
- (33) Engstrom, R. C.; Weber, M.; Wunder, D. J.; Burgess, R.; Winqvist, S. *Anal. Chem.* 1986, 58, 844–848.
- (34) Lefrou, C.; Cornut, R. *ChemPhysChem* 2010, 11, 547–556.
- (35) Fernández, J. L.; Bard, A. J. *Anal. Chem.* 2004, 76, 2281–2289.
- (36) Bard, A. J.; Mirkin, M. V. *Scanning Electrochemical Microscopy*; Second.; Taylor & Francis Group: Boca Raton, 2012.
- (37) Amemiya, S.; Bard, A. J.; Fan, F.-R. F.; Mirkin, M. V.; Unwin, P. R. *Annu. Rev. Anal. Chem.* 2008, 1, 95–131.

- (38) Mirkin, M. V.; Nogala, W.; Velmurugan, J.; Wang, Y. *Phys. Chem. Chem. Phys.* 2011, 13, 21196–21212.
- (39) Bergner, S.; Vatsyayan, P.; Matysik, F.-M. *Anal. Chim. Acta* 2013, 775, 1–13.
- (40) Beaulieu, I.; Kuss, S.; Mauzeroll, J.; Geissler, M. *Anal. Chem.* 2011, 83, 1485–1492.
- (41) Bard, A. J.; Faulkner, L. R. *Electrochemical Methods: Fundamentals and Applications*; 2nd Editio.; Jonh Wiley & Sons Inc.: New Jersey, 2001.
- (42) Combellas, C.; Fermigier, M.; Fuchs, A.; Kanoufi, F. *Anal. Chem.* 2005, 77, 7966–7975.
- (43) Kranz, C.; Friedbacher, G.; Mizaikofft, B.; Lugstein, A.; Smoliner, J.; Bertagnolli, E. *Anal. Chem.* 2001, 73, 2491–2500.
- (44) Kranz, C. *Analyst* 2014, 139, 336–352.
- (45) Bard, A. J.; Fan, F.-R.; Kwak, J.; Lev, O. *Anal. Chem.* 1989, 61, 132–138.
- (46) Kwak, J.; Bard, A. J. *Anal. Chem.* 1989, 61, 1794–1799.
- (47) Lee, C.; Bard, A. J. *Anal. Chem.* 1990, 62, 1906–1913.
- (48) Lee, Y.; Ding, Z.; Bard, A. J. *Anal. Chem.* 2002, 74, 3634–3643.
- (49) Eckhard, K.; Schuhmann, W. *Analyst* 2008, 133, 1486–1497.
- (50) Eckhard, K.; Etienne, M.; Schulte, A.; Schuhmann, W. *Electrochem. Commun.* 2007, 9, 1793–1797.
- (51) Diakowski, P. M.; Ding, Z. *Phys. Chem. Chem. Phys.* 2007, 9, 5966–5974.
- (52) Diakowski, P. M.; Ding, Z. *Electrochem. commun.* 2007, 9, 2617–2621.
- (53) Dunn, R. C. *Chem. Rev.* 1999, 99, 2891–2927.
- (54) Ludwig, M.; Kranz, C.; Schuhmann, W.; Gaub, H. E. *Rev. Sci. Instrum.* 1995, 66, 2857–2860.
- (55) Hengstenberg, A.; Kranz, C.; Schuhmann, W. *Chem. Eur. J.* 2000, 6, 1547–1554.
- (56) James, P. I.; Garfias-Mesias, L. F.; Moyer, P. J.; Smyrl, W. H. *J. Electrochem. Soc.* 1998, 145, L64–L66.
- (57) Takahashi, Y.; Shiku, H.; Murata, T.; Yasukawa, T.; Matsue, T. *Anal. Chem.* 2009, 81, 9674–9681.

- (58) Ballesteros Katemann, B.; Schulte, A.; Schuhmann, W. *Chem. - A Eur. J.* 2003, 9, 2025–2033.
- (59) Etienne, M.; Anderson, E. C.; Evans, S. R.; Schuhmann, W.; Fritsch, I. *Anal. Chem.* 2006, 78, 7317–7324.
- (60) Etienne, M.; Dierkes, P.; Erichsen, T.; Schuhmann, W.; Fritsch, I. *Electroanalysis* 2007, 19, 318–323.
- (61) Cougnon, C.; Bauer-Espindola, K.; Fabre, D. S.; Mauzeroll, J. *Anal. Chem.* 2009, 81, 3654–3659.
- (62) Alberts, B.; Johnson, A.; Lewis, J.; Raff, M.; Roberts, K.; Walter, P. *Molecular Biology of the Cell*; 4th ed.; Taylor & Francis Books, Inc., 2002.
- (63) Bachmann, B. J. *Microbiol. Rev.* 1990, 54, 130–197.
- (64) Stein, W. D. *Channels, Carriers and Pumps: An Introduction to Membrane Transport*; San Diego: Academic Press, 1990.
- (65) Higgins, C. F. *Annu. Rev. Cell Biol.* 1992, 8, 67–113.
- (66) Almers, W.; Stirling, C. J. *Membr. Biol.* 1984, 77, 169–186.
- (67) Tanford, C. *Annu. Rev. Biochem.* 1983, 52, 379–409.
- (68) Bianchet, M. A.; Ko, Y. H.; Amzel, L. M.; Pedersen, P. L. J. *Bioenerg. Biomembr.* 1997, 29, 503–524.
- (69) Kirk, K. L.; Wang, W. J. *Biol. Chem.* 2011, 286, 12813–12819.
- (70) Mu, J.; Ferdig, M. T.; Feng, X.; Joy, D. A.; Duan, J.; Furuya, T.; Subramanian, G.; Aravind, L.; Cooper, R. A.; Wootton, J. C.; Xiong, M.; Su, X.-Z. *Mol. Microbiol.* 2003, 49, 977–989.
- (71) Goldstein, L. J.; Pastan, I.; Gottesman, M. M. *Crit. Rev. Oncol. Hematol.* 1992, 12, 243–253.
- (72) Dean, M.; Hamon, Y.; Chimini, G. J. *Lipid Res.* 2001, 42, 1007–1017.
- (73) Gottesman, M. M.; Fojo, T.; Bates, S. E. *Nat. Rev. Cancer* 2002, 2, 48–58.
- (74) Larbcharoensub, N.; Leopairat, J.; Sirachainan, E.; Narkwong, L.; Bhongmakapat, T.; Rasmeepaisarn, K.; Janvilisri, T. *Hum. Pathol.* 2008, 39, 837–845.
- (75) Persidis, A. *Nat. Biotechnol.* 1999, 17, 94–95.

- (76) Styczynski, J.; Wysocki, M.; Debski, R.; Czyzewski, K.; Kolodziej, B.; Rafinska, B.; Kubicka, M.; Koltan, S.; Koltan, A.; Pogorzala, M.; Kurylak, A.; Olszewska-Slonina, D.; Balwierz, W.; Juraszewska, E.; Wieczorek, M.; Olejnik, I.; Krawczuk-Rybak, M.; Kuzmich, M.; Kowalczyk, J.; Stefaniak, J.; Badowska, W.; Sonta-Jakimczyk, D.; Szczepanski, T.; Matysiak, M.; Malinowska, I.; Stanczak, E. *J. Cancer Res. Clin. Oncol.* 2007, 133, 875–893.
- (77) Scherer, W. F.; Syverton, J. T.; Gey, G. O. *J. Exp. Med.* 1953, 97, 695–710.
- (78) Paloma Vizcaino, A.; Moreno, V.; Xavier Bosch, F.; Muñoz, N.; Barros-Dios, X. M.; Maxwell Parkin, D. *Int. J. Cancer* 1998, 75, 536–545.
- (79) Bubenik, J. *Curr. Cancer Drug Targets* 2008, 8, 180–186.
- (80) Hampl, M. *Minerva Med.* 2007, 98, 121–130.
- (81) Sasso, S. V.; Pierce, R. J.; Walla, R.; Yacynych, A. M. *Anal. Chem.* 1990, 62, 1111–1117.
- (82) Kast, C.; Gros, P. *Biochemistry* 1998, 37, 2305–2313.
- (83) Kast, C.; Grost, P. *J. Biol. Chem.* 1997, 272, 26479–26487.
- (84) Puck, T. T.; Marcus, P. I.; Cieciora, S. J. *J. Exp. Med.* 1956, 103, 273–284.
- (85) Bourguignon, L. Y. W.; Xia, W.; Wong, G. J. *Biol. Chem.* 2009, 284, 2657–2671.
- (86) Bergner, S.; Wegener, J.; Matysik, F.-M. *Anal. Methods* 2012, 4, 623–629.
- (87) Kuss, S.; Cornut, R.; Beaulieu, I.; Mezour, M. A.; Annabi, B.; Mauzeroll, J. *Bioelectrochemistry* 2011, 82, 29–37.
- (88) Au, W. Y.; Chim, C. S.; Lie, A. K. W.; Pang, A.; Kwong, Y. L. *Haematologica* 2002, 87, 1109–1111.
- (89) Grunebach, F.; Griese, E. U.; Schumacher, K. J. *Cancer Res. Clin. Oncol.* 1994, 120, 539–544.
- (90) Hayashi, T.; Kobayashi, H.; Miyachi, H.; Ohshima, T.; Ujiiye, T.; Kawase, M.; Hotta, T.; Takemura, Y. *Clin. Chim. Acta* 2004, 342, 115–126.
- (91) Kobayashi, H.; Takemura, Y.; Kawai, Y.; Miyachi, H.; Kawabata, M.; Matsumura, T.; Yamashita, T.; Mori, S.; Furihata, K.; Shimodaira, S.; Motoyoshi, K.; Hotta, T.; Sekiguchi, S.; Ando, Y.; Watanabe, K. *J. Lab. Clin. Med.* 2000, 135, 199–209.
- (92) Li, N.; Nemirovskiy, O. V.; Zhang, Y.; Yuan, H.; Mo, J.; Ji, C.; Zhang, B.; Brayman, T. G.; Lepsy, C.; Heath, T. G.; Lai, Y. *Anal. Biochem.* 2008, 380, 211–222.

- (93) Li, Y.; Wang, Y. Z. *Prog. Biochem. Biophys.* 1998, 25, 146–147.
- (94) Souslova, T.; Averill-Bates, D. A. *Int. J. Radiat. Oncol. Biol. Phys.* 2004, 60, 1538–1551.
- (95) Lu, H.; Gratzl, M. *Anal. Chem.* 1999, 71, 2821–2830.
- (96) Binyamin, L.; Assaraf, Y. G.; Reiter, Y. *Int. J. Cancer* 2005, 116, 703–709.
- (97) Feller, N.; Kuiper, C. M.; Lankelma, J.; Ruhdal, J. K.; Scheper, R. J.; Pinedo, H. M.; Broxterman, H. J. *Br. J. Cancer* 1995, 72, 543–549.
- (98) Olson, D. P.; Taylor, B. J.; Ivy, S. P. *Commun. Clin. Cytom.* 2001, 46, 105–113.
- (99) Pallis, M.; Russell, N. H. *Br. J. Haematol.* 1998, 100, 194–197.
- (100) Mauzeroll, J.; Schougaard, S. B. *Electrochemical Microscopy of Living Cells. (Chapter 12)* In *Scanning Electrochemical Microscopy*, 2012, 379.
- (101) Yasukawa, T.; Kondo, Y.; Uchida, I.; Matsue, T. *Chem. Lett.* 1998, 8, 767–768.
- (102) Liu, B.; Cheng, W.; Rotenberg, S. A.; Mirkin, M. V. *J. Electroanal. Chem.* 2001, 500, 590–597.
- (103) Liu, B.; Rotenberg, S. A.; Mirkin, M. V. *Proc. Natl. Acad. Sci.* 2000, 97, 9855–9860.
- (104) Mirkin, M. V.; Liu, B.; Rotenberg, S. A. *Methods Enzymol.* 2002, 352, 112–122.
- (105) Rotenberg, S. A.; Mirkin, M. V. *J. Mammary Gland Biol. Neoplasia* 2004, 9, 375–382.
- (106) Koley, D.; Bard, A. J. *Proc. Natl. Acad. Sci. U. S. A.* 2010, 107, 16783–16787.
- (107) Li, X.; Bard, A. J. *J. Electroanal. Chem.* 2009, 628, 35–42.
- (108) Mauzeroll, J.; Bard, A. J.; Owhadian, O.; Monks, T. J. *Proc. Natl. Acad. Sci.* 2004, 101, 17582–17587.
- (109) Mauzeroll, J.; Bard, A. J. *Proc. Natl. Acad. Sci.* 2004, 101, 7862–7867.
- (110) Koley, D.; Bard, A. J. *Proc. Natl. Acad. Sci. U. S. A.* 2012, 109, 11522–11527.
- (111) Luk, Y.-Y.; Kato, M.; Mrksich, M. *Langmuir* 2000, 16, 9604–9608.
- (112) Mrksich, M.; Dike, L. E.; Tien, J.; Ingber, D. E.; Whitesides, G. M. *Exp. Cell Res.* 1997, 235, 305–313.

- (113) Csucs, G.; Michel, R.; Lussi, J. W.; Textor, M.; Danuser, G. *Biomaterials* 2003, 24, 1713–1720.
- (114) Wilson Jr, W. C.; Boland, T. *Anat. Rec. - Part A Discov. Mol. Cell. Evol. Biol.* 2003, 272, 491–496.
- (115) Beaulieu, I.; Geissler, M.; Mauzeroll, J. *Langmuir* 2009, 25, 7169–7176.
- (116) Takayama, S.; McDonald, J. C.; Ostuni, E.; Liang, M. N.; Kenis, P. J. A.; Ismagilov, R. F.; Whitesides, G. M. *Proc. Natl. Acad. Sci. U. S. A.* 1999, 96, 5545–5548.
- (117) Folch, A.; Jo, B. H.; Hurtado, O.; Beebe, D. J.; Toner, M. J. *Biomed. Mater. Res.* 2000, 52, 346–353.
- (118) Tourovskaia, A.; Barber, T.; Wickes, B. T.; Hirdes, D.; Grin, B.; Castner, D. G.; Healy, K. E.; Folch, A. *Langmuir* 2003, 19, 4754–4764.
- (119) Brassard, D.; Clime, L.; Li, K.; Geissler, M.; Miville-Godin, C.; Roy, E.; Veres, T. *Lab Chip* 2011, 11, 4099–4107.
- (120) Geissler, M.; Roy, E.; Diaz-Quijada, G. A.; Galas, J.-C.; Veres, T. *ACS Appl. Mater. Interfaces* 2009, 1, 1387–1395.
- (121) Roy, E.; Geissler, M.; Galas, J. C.; Veres, T. *Microfluid. Nanofluidics* 2011, 11, 235–244.
- (122) Ostuni, E.; Kane, R.; Chen, C. S.; Ingber, D. E.; Whitesides, G. M. *Langmuir* 2000, 16, 7811–7819.
- (123) Hu, J.; Shi, J.; Zhang, F.; Lei, L.; Li, X.; Wang, L.; Liu, L.; Chen, Y. *Microelectron. Eng.* 2010, 87, 726–729.
- (124) Irimia, D.; Karlsson, J. O. M. *Biomed. Microdevices* 2003, 5, 185–194.
- (125) Ishizaki, T.; Saito, N.; Takai, O. *Langmuir* 2010, 26, 8147–8154.
- (126) Jin, L. H.; Yang, B. Y.; Zhang, L.; Lin, P. L.; Cui, C.; Tang, J. *Langmuir* 2009, 25, 5380–5383.
- (127) Mercey, E.; Obeïd, P.; Glaise, D.; Calvo-Muñoz, M.-L.; Guguen-Guillouzo, C.; Fouqué, B. *Biomaterials* 2010, 31, 3156–3165.
- (128) Graham, D. J.; Price, D. D.; Ratner, B. D. *Langmuir* 2002, 18, 1518–1527.
- (129) Wittstock, G.; Emons, H.; Kummer, M.; Kirchhoff, J. R.; Heineman, W. R. *Fresenius. J. Anal. Chem.* 1994, 348, 712–718.

- (130) Lagarias, J. C.; Reeds, J. A.; Wright, M. H.; Wright, P. E. *SIAM J. Optim.* 1999, 9, 112–147.
- (131) Cornut, R.; Lefrou, C. *J. Electroanal. Chem.* 2007, 608, 59–66.
- (132) Xue, Y.; Lei, J.; Xu, X.; Ding, L.; Zhai, C.; Yan, F.; Ju, H. *Chem. Commun.* 2010, 46, 7388–7390.
- (133) Liebetrau, J. M.; Miller, H. M.; Baur, J. E.; Takacs, S. A.; Anupunpisit, V.; Garris, P. A.; Wipf, D. O. *Anal. Chem.* 2003, 75, 563–571.
- (134) Mirkin, M. V.; Fan, F.-R. F.; Bard, A. J. *J. Electroanal. Chem.* 1992, 328, 47–62.
- (135) Wei, C.; Bard, A. J.; Mirkin, M. V. *J. Phys. Chem.* 1995, 99, 16033–16042.
- (136) Tada, Y.; Wada, M.; Migita, T.; Nagayama, J.; Hinoshita, E.; Mochida, Y.; Maehara, Y.; Tsuneyoshi, M.; Kuwano, M.; Naito, S. *Int. J. Cancer* 2002, 98, 630–635.
- (137) Niu, L.; Yin, Y.; Guo, W.; Lu, M.; Qin, R.; Chen, S. *J. Mater. Sci.* 2009, 44, 4511–4521.
- (138) Schulte, A.; Nebel, M.; Schuhmann, W. *Annu. Rev. Anal. Chem.* 2010, 3, 299–318.
- (139) Zhang, M. M. N.; Long, Y.-T. T.; Ding, Z. *J. Inorg. Biochem.* 2012, 108, 115–122.
- (140) Nkuku, C. A.; LeSuer, R. J. *J. Phys. Chem. B* 2007, 111, 13271–13277.
- (141) Cornut, R.; Poirier, S.; Mauzeroll, J. *Anal. Chem.* 2012, 84, 3531–3537.
- (142) Edwards, M. A.; Whitworth, A. L.; Unwin, P. R. *Anal. Chem.* 2011, 83, 1977–1984.
- (143) Davoodi, A.; Farzadi, A.; Pan, J.; Leygraf, C.; Zhu, Y. *J. Electrochem. Soc.* 2008, 155, C474–C485.
- (144) Mauzeroll, J.; Hueske, E. A.; Bard, A. J. *Anal. Chem.* 2003, 75, 3880–3889.
- (145) Potter, M.; Wiggart, D. *Schaum's Outline of Fluid Mechanics*; McGraw-Hill, USA, 2008.
- (146) Liljeroth, P.; Johans, C.; Slevin, C. J.; Quinn, B. M.; Kontturi, K. *Electrochem. commun.* 2002, 4, 67–71.
- (147) Bourdillon, C.; Demaille, C.; Moiroux, J.; Saveant, J.-M. *J. Am. Chem. Soc.* 1995, 117, 11499–11506.
- (148) Cannes, C.; Kanoufi, F.; Bard, A. J. *J. Electroanal. Chem.* 2003, 547, 83–91.

- (149) Wittstock, G.; Emons, H.; Ridgway, T. H.; Blubaugh, E. A.; Heineman, W. R. *Anal. Chim. Acta* 1994, 298, 285–302.
- (150) Kuss, S.; Polcari, D.; Geissler, M.; Brassard, D.; Mauzeroll, J. *Proc. Natl. Acad. Sci. U. S. A.* 2013, 110, 9249–9254.
- (151) Cortés-Salazar, F.; Träuble, M.; Li, F.; Busnel, J.-M.; Gassner, A.-L.; Hojeij, M.; Wittstock, G.; Girault, H. H. *Anal. Chem.* 2009, 81, 6889–6896.
- (152) Cortés-Salazar, F.; Lesch, A.; Momotenko, D.; Busnel, J.-M.; Wittstock, G.; Girault, H. H. *Anal. Methods* 2010, 2, 817–823.
- (153) Cortés-Salazar, F.; Momotenko, D.; Lesch, A.; Wittstock, G.; Girault, H. H. *Anal. Chem.* 2010, 82, 10037–10044.
- (154) Cortés-Salazar, F.; Momotenko, D.; Girault, H. H.; Lesch, A.; Wittstock, G. *Anal. Chem.* 2011, 83, 1493–1499.
- (155) Lesch, A.; Vaske, B.; Meiners, F.; Momotenko, D.; Cortés-Salazar, F.; Girault, H. H.; Wittstock, G. *Angew. Chemie - Int. Ed.* 2012, 51, 10413–10416.
- (156) Borgwarth, K.; Ebling, D.; Heinze, J. *Electrochim. Acta* 1995, 40, 1455–1460.
- (157) Kuss, S.; Kuss, C.; Trinh, D.; Schougaard, S. B.; Mauzeroll, J. *Electrochim. Acta* 2013, 110, 42–48.
- (158) Lu, M. Q.; Chen, S. L.; Xiao, B.; Xia, C. Q.; Qi, M. *Zhonghua Nei Ke Za Zhi* 2006, 45, 45–48.
- (159) Ledoux, A. C.; Perkins, N. D. *Biochem. Soc. Trans.* 2014, 42, 76–81.
- (160) Macpherson, J. V.; Unwin, P. R.; Hillier, A. C.; Bard, A. J. *J. Am. Chem. Soc.* 1996, 118, 6445–6452.
- (161) Rice-Evans, C. A.; Miller, N. J.; Paganga, G. *Trends Plant Sci.* 1997, 2, 152–159.
- (162) Greenwald, P.; Clifford, C. K.; Milner, J. A. *Eur. J. Cancer* 2001, 37, 948–965.
- (163) Balentine, D. A.; Wiseman, S. A.; Bouwens, L. C. M. *Crit. Rev. Food Sci. Nutr.* 1997, 37, 693–704.
- (164) Dong, Z.; Ma, W.-Y.; Huang, C.; Yang, C. S. *Cancer Res.* 1997, 57, 4414–4419.
- (165) Khafif, A.; Schantz, S. P.; Chou, T. C.; Edelstein, D.; Sacks, P. G. *Carcinogenesis* 1998, 19, 419–424.

- (166) Katiyar, S. K.; Mukhtar, K. *Int. J. Oncol.* 1996, 8, 221–238.
- (167) Higdon, J. V.; Frei, B. *Crit. Rev. Food Sci. Nutr.* 2003, 43, 89–143.
- (168) Yang, C. S.; Maliakal, P.; Meng, X. Inhibition of carcinogenesis by tea. *Annual Review of Pharmacology and Toxicology*, 2002, 42, 25–54.
- (169) Siddiqui, I. A.; Afaq, F.; Adhami, V. M.; Ahmad, N.; Mukhtar, H. *Antioxidants Redox Signal.* 2004, 6, 571–582.
- (170) Grove, K. A.; Lambert, J. D. *J. Nutr.* 2010, 140, 446–453.
- (171) Lambert, J. D.; Elias, R. J. *Arch. Biochem. Biophys.* 2010, 501, 65–72.
- (172) Yiannakopoulou, E. C. *Eur. J. Cancer Prev.* 2014, 23, 84–89.
- (173) Rathore, K.; Wang, H.-C. *R. Mol. Carcinog.* 2012, 51, 280–289.
- (174) Rathore, K.; Wang, H. C. *R. Cancer Lett.* 2013, 333, 113–123.
- (175) Kilmartin, P. A.; Hsu, C. F. *Food Chem.* 2003, 82, 501–512.
- (176) Janeiro, P.; Oliveira Brett, A. M. *Anal. Chim. Acta* 2004, 518, 109–115.
- (177) Narumi, K.; Sonoda, J.-I.; Shiotani, K.; Shigeru, M.; Shibata, M.; Kawachi, A.; Tomishige, E.; Sato, K.; Motoya, T. *J. Chromatogr. B Anal. Technol. Biomed. Life Sci.* 2014, 945-946, 147–153.
- (178) Kotani, A.; Miyashita, N.; Kusu, F. *J. Chromatogr. B Anal. Technol. Biomed. Life Sci.* 2003, 788, 269–275.
- (179) Zhan, D.; Fan, F.-R. F.; Bard, A. J. *Proc. Natl. Acad. Sci.* 2008, 105, 12118–12122.
- (180) Yasukawa, T.; Matsue, T. *Electrochemistry* 1999, 67, 264–268.
- (181) Kasai, S.; Shiku, H.; Torisawa, Y.-S.; Noda, H.; Yoshitake, J.; Shiraishi, T.; Yasukawa, T.; Watanabe, T.; Matsue, T.; Yoshimura, T. *Anal. Chim. Acta* 2005, 549, 14–19.
- (182) Zhan, D.; Li, X.; Zhan, W.; Fan, F.-R. F.; Bard, A. J. *Anal. Chem.* 2007, 79, 5225–5231.
- (183) Zhao, X.; Diakowski, P. M.; Ding, Z. *Anal. Chem.* 2010, 82, 8371–8373.
- (184) Koley, D.; Bard, A. J. *Proc. Natl. Acad. Sci.* 2010, 107, 16783–16787.
- (185) Kuss, S.; Trinh, D.; Danis, L.; Mauzeroll, J. *Anal. Chem.*; DOI: 10.1021/acs.analchem.5b01268.

- (186) Sies, H. *Free Radic. Biol. Med.* 1999, 27, 916–921.
- (187) Townsend, D. M.; Tew, K. D.; Tapiero, H. *Biomed. Pharmacother.* 2003, 57, 145–155.
- (188) Nielsen, L. K.; Smyth, G. K.; Greenfield, P. F. *Biotechnol. Prog.* 1991, 7, 560–563.
- (189) Sánchez-Tena, S.; Alcarraz-Vizán, G.; Marín, S.; Torres, J. L.; Cascante, M. J. *Agric. Food Chem.* 2013, 61, 4310–4317.
- (190) Puig, T.; Vázquez-Martín, A.; Relat, J.; Pétriz, J.; Menéndez, J. A.; Porta, R.; Casals, G.; Marrero, P. F.; Haro, D.; Brunet, J.; Colomer, R. *Breast Cancer Res. Treat.* 2008, 109, 471–479.
- (191) Patil, L. J.; Bothara, S. B.; Balaraman, R. *Int. J. Green Pharm.* 2010, 4, 170–173.
- (192) Senthil Kumaran, V.; Arulmathi, K.; Srividhya, R.; Kalaiselvi, P. *Exp. Gerontol.* 2008, 43, 176–183.
- (193) Hong, J.; Lu, H.; Meng, X.; Ryu, J.-H.; Hara, Y.; Yang, C. S. *Cancer Res.* 2002, 62, 7241–7246.
- (194) Youn, H. S.; Lee, J. Y.; Saitoh, S. I.; Miyake, K.; Kang, K. W.; Choi, Y. J.; Hwang, D. H. *Biochem. Pharmacol.* 2006, 72, 850–859.
- (195) Tate Jr., D. J.; Newsome, D. A.; Oliver, P. D. *Investig. Ophthalmol. Vis. Sci.* 1993, 34, 2348–2351.
- (196) Harlan, J. M.; Levine, J. D.; Callahan, K. S.; Schwartz, B. R.; Harker, L. A. *J. Clin. Invest.* 1984, 73, 706–713.
- (197) Kwak, J.; Bard, A. J. *Anal. Chem.* 1989, 61, 1221–1227.
- (198) Nagamine, K.; Kaya, T.; Yasukawa, T.; Shiku, H.; Matsue, T. *Sensors Actuators B Chem.* 2005, 108, 676–682.
- (199) Matsui, N.; Kaya, T.; Nagamine, K.; Yasukawa, T.; Shiku, H.; Matsue, T. *Biosens. Bioelectron.* 2006, 21, 1202–1209.
- (200) Cai, C.; Liu, B.; Mirkin, M. V.; Frank, H. A.; Rusling, J. F. *Anal. Chem.* 2002, 74, 114–119.
- (201) Nagamine, K.; Matsui, N.; Kaya, T.; Shiku, H.; Nakayama, T.; Nishino, T.; Matsue, T. *Biosens. Bioelectron.* 2005, 21, 145–151.
- (202) Holt, K. B.; Bard, A. J. *Biochemistry* 2005, 44, 13214–13223.

- (203) Kaya, T.; Numai, D.; Nagamine, K.; Aoyagi, S.; Shiku, H.; Matsue, T. *Analyst* 2004, 129, 529–534.
- (204) Lu, X.; Wang, Q.; Liu, X. *Anal. Chim. Acta* 2007, 601, 10–25.
- (205) Gao, N.; Wang, X.; Li, L.; Zhang, X.; Jin, W. *Analyst* 2007, 132, 1139–1146.
- (206) Shen, M.; Ishimatsu, R.; Kim, J.; Amemiya, S. *J. Am. Chem. Soc.* 2012, 134, 9856–9859.
- (207) Etienne, M.; Schulte, A.; Schuhmann, W. *Electrochem. commun.* 2004, 6, 288–293.
- (208) Ballesteros Katemann, B.; Schulte, A.; Schuhmann, W. *Electroanalysis* 2004, 16, 60–65.
- (209) Schulte, A.; Nebel, M.; Schuhmann, W. *Methods Enzymol.* 2012, 504, 237–254.
- (210) Horrocks, B. R.; Schmidtke, D.; Heller, A.; Bard, A. J. *Anal. Chem.* 1993, 65, 3605–3614.
- (211) Kashyap, R.; Gratzl, M. *Anal. Chem.* 1999, 71, 2814–2820.
- (212) Ballesteros Katemann, B.; Schulte, A.; Calvo, E. J.; Koudelka-Hep, M.; Schuhmann, W. *Electrochem. commun.* 2002, 4, 134–138.
- (213) Gabrielli, C.; Huet, F.; Keddou, M.; Rousseau, P.; Vivier, V. *J. Phys. Chem. B* 2004, 108, 11620–11626.
- (214) Alpuche-Aviles, M. A.; Wipf, D. O. *Anal. Chem.* 2001, 73, 4873–4881.
- (215) Kurulugama, R. T.; Wipf, D. O.; Takacs, S. A.; Pongmayteegul, S.; Garris, P. A.; Baur, J. E. *Anal. Chem.* 2005, 77, 1111–1117.
- (216) Osbourn, D. M.; Sanger, R. H.; Smith, P. J. S. *Anal. Chem.* 2005, 77, 6999–7004.
- (217) Brunk, U.; Collins, V. P.; Arro, E. J. *Microsc.* 1981, 123, 121–131.
- (218) Schrand, A. M.; Schlager, J. J.; Dai, L.; Hussain, S. M. *Nat. Protoc.* 2010, 5, 744–757.
- (219) Kueng, A.; Kranz, C.; Lugstein, A.; Bertagnolli, E.; Mizaikoff, B. *Angew. Chemie - Int. Ed.* 2005, 44, 3419–3422.
- (220) Horan, P. K.; Slezak, S. E. *Nature* 1989, 340, 167–168.